PRECIPITATION GRADIENTS ACROSS THE CONTINENTAL DIVIDE IN THE SOUTHERN CANADIAN ROCKIES

By

Selina Mitchell, B.Sc., University of Northern British Columbia, 2007

THESIS SUBMITTED IN PARTIAL FULFILLMENT OF THE DEGREE OF MASTER OF SCIENCE

IN NATURAL RESOURCES AND ENVIRONMENTAL STUDIES

UNIVERSITY OF NORTHERN BRITISH COLUMBIA

December, 2022

Abstract

This project examines precipitation patterns across the Continental Divide in the southern Canadian Rockies with a focus on precipitation gradients. This thesis is part of the Storms and Precipitation Across the continental Divide Experiment (SPADE) that occurred between 26 April 2019 and 26 June 2019. Daily meteorological data were also examined between 2011 and 2019. The study area encompassed mountainous topography from the Columbia Valley in eastern British Columbia, to a transect of stations alongside the Foothills in western Alberta, with a range of elevations from about 750 m to about 3500 m above sea level. Local station data were derived from three meteorological stations developed for the SPADE campaign, Nipika Mountain Resort (Nipika), Fortress Junction, Fortress Mountain and a tipping bucket transect. Regional station data were derived from several meteorological station networks with publicly available data. Gridded data included ERA5 and ERA5-Land. Cumulative precipitation amounts were the focus of this study, but temperature, relative humidity, and wind speed and direction were also included in my analysis. The objectives of this project are to examine relationships between precipitation gradients/patterns and elevation, cool and warm seasons, general wind patterns/storm trajectories, and inter-annual and intra-annual variability. Elevation is a predictor of precipitation amounts in our study region, and over most time-frames it was a stronger predictor than latitude and longitude in determining precipitation amounts, but the relationship between elevation and precipitation was not always significant. On average precipitation increases at a rate of 0.39 mm m^{-1} across the study region when it is examined across an annual period. Warm (summer) and cool (winter) seasons exhibited distinctly different precipitation gradients. A southerly wind component at Nipika was associated with large amounts of precipitation at this site.

Temperatures, wind speed and wind direction varied across the nine-year study period, with some distinct changes occurring during the 2014 to 2016 El Niño period. Precipitation exhibited different diurnal patterns on each side of the Continental Divide. Overall, precipitation amounts varied substantially across years, while precipitation patterns retained similarities.

Committee Members

Dr. Stephen Déry

Department of Geography, Earth and Environmental Sciences, University of Northern British Columbia, Prince George, British Columbia, Canada.

Dr. Peter Jackson

Department of Geography, Earth and Environmental Sciences, University of Northern British Columbia, Prince George, British Columbia, Canada.

Dr. Julie Thériault

Département des Sciences de la Terre et de l'Atmosphère, Université du Québec à Montréal, Montréal, Québec, Canada.

Table of Contents

List of Tables

List of Figures

Acknowledgements

My work took place on the traditional lands of the Lheidli T'enneh, the Ktunuxa, the Îyârhe Nakoda (Stoney Nakoda), the Tsuut'ina First Nation, the Blackfoot Confederacy, and the Métis Nation of Alberta. I extend deep gratitude towards these nations.

I would like to extend my profound thanks to the following:

Stephen Déry for his tremendous support and patience. I am grateful for his wide-ranging expertise in hydrometeorology and his beautiful approach to fostering academic growth. Thank you for taking me on and putting up with me. Additionally, thank you to his dog Angel for her delightful moral support in the field.

Julie Thériault for providing some excellent leadership for the SPADE project. It was a great pleasure to be a part of this amazing project and I look back on it as one of the best experiences of my life. I am appreciative of her collaborative approach.

Peter Jackson for kindly agreeing to be on my committee and for helping me to reacquaint myself with meteorology. Additionally, many thanks for to creating a comprehensive repository of meteorological data for our project.

Craig Smith for generously agreeing to be the external examiner for my thesis. I appreciated your exceptional insights. Thank you for your beneficial critique.

John Pomeroy and Ron Stewart for their generous advice and support for this project.

The Global Water Futures (GWF) research program funding. This generous funding alleviated financial strain during my studies.

The owners and operators of Nipika Mountain Resort Lyle, Dianne, and Steven Wilson, and their employees. Thank you for your tremendous hospitality and for generously allowing us to use your beautiful land for our research.

The owners of Fortress Mountain and the caretaker, Mountain Mel, who provided warmth, hospitality, and protection from the elements at this remote site.

Plamen and his family for providing excellent accommodations at Radium Hot Springs.

The University of Calgary Biogeoscience Institute, particularly Adrienne Cunnings, for providing a wonderful environment for remote research.

The Coldwater Laboratory which is part of the University of Saskatchewan Global Water Futures (GWF) project. I was greatly appreciative of the use of this facility and the generous people within its walls that donated their expertise to this project.

Ian Knuckey and Fabio Stern at Baymag Mine for kindly providing detailed meteorological data from Kootenay National Park.

The Changing Cold Regions Network (CCRN) for providing excellent data from remote sites in the Canadian Rockies. Many thanks to both Laleh Moradi and Amber Peterson for deftly fielding questions and providing access to data.

The Alberta Climate Information Service (ACIS), found at https://acis.alberta.ca, for providing wide-ranging data from numerous sites in Alberta. Many thanks to Ralph Wright for providing his expertise on data and quality control procedures.

The Ministry of Transportation and Infrastructure (MOTI) Weather Network Program. Thank you to Rob Andersen, Adam Todd, and Tanya McKinney for kindly providing detailed metadata regarding these sites.

The BC Wildfire Service in the Ministry of Forests, Lands, Natural Resource Operations and Rural Development (FLNRORD) for providing meteorological data from several sites in British Columbia. Thank you to Joanna Wand, Brady Holliday, Jesse Ellis, Andrew Skinner, and Mike Pepin for generously contributing their expertise regarding their sites.

John Rex at the Research and Stewardship in the Omineca Region of Forests, Lands, Natural Resource Operations and Rural Development for kindly loaning us the Tipping Bucket Rain Gauges (TBRGs) in our rain gauge transect.

The Pacific Climate Impacts Consortium (PCIC) for providing a user-friendly interface for collecting meteorological data and to Faron Anslow for providing excellent support.

The National Center for Atmospheric Research (NCAR) for providing some expert quality control for some meteorological time series from SPADE stations.

You Qin Wang at the University of Northern British Columbia High Performance Computing Lab for storing a copy of SPADE meteorological data.

Frank Weber at BC Hydro for providing an overview of snow pillow metadata.

Ian Jackson and Brian Webster for providing an overview of Avalanche Canada meteorological data.

Juris Almonte for tremendous support as the SPADE project manager, and then for her wide-ranging expertise as a field technician at Environment and Climate Change Canada. I am grateful for her generosity that stretched beyond her obligations to this project.

Hilary Smith for excellent support as a colleague, the project manager of SPADE, and as a lead author of our publications. I am grateful for her tremendous organizational skills and patience.

Jeremy Morris and Hadleigh Thompson for their fantastic support during the campaign and the thesis writing process. These two have furnished me with hours of help on all manner of meteorological equipment and computer systems, in addition to providing tremendous moral support during inclement weather.

Aseem Sharma and Siraj Ul Islam for their generous support in coding, data storage, and for providing me with a comprehensive understanding of gridded data.

Rajtantra Lilhare for his expertise in ERA5 and ERA5-Land data downloading and processing. My work with ERA5 would not have been possible without his precise directions and gentle support.

My fellow participants in the SPADE campaign: Cécile Carton, Charlie Hébert-Pinard, André Bertoncini, Aurélie Desroches-Lapointe, and Mathieu Lachapelle. Thank you for your tremendous camaraderie and wisdom.

Margot Vore, Brayden Nilsen, Sara Darychuk, and Adele Halper for generously helping me with coding. I am tremendously grateful for your rescue.

Christine Jackson and my colleagues in the Weather and Climate course (ENSC 201) at the University of Northern British Columbia, for patiently helping me to revise my rusty meteorological skills.

The University of Northern British Columbia Geographical Information Systems (GIS) Lab including Scott Emmons, Roger Wheate, Ping Bai, and Matt McLean. Thank you for providing me with GIS software and expert advice on how to produce beautiful maps.

The University of Northern British Columbia library staff for providing excellent support in the library and for furnishing me with critical thesis formatting skills.

Kelly Hurley for helping me with office resources and providing me with great morale during long writing sessions.

Other colleagues past and present at the Northern Hydrometeorology Group (NHG) based at the University of Northern British Columbia who have provided expert advice and emotional support. They have borne the brunt of helping me to refine my presentations. These colleagues include Justin Kokoszka, Michael Allchin, Natalya Klutz, Ivy Strothers, Tamar Richards-Thomas, Lisa Rickard, Bruno Sobral, Pierrick Lamontagne-Halle, Derek Gilbert, Anna Kaveney, Spencer Woyke, Emile Cardinal, Adam MacDonald, Daniel Scurfield, Jingwen Wu, and Uttam Puri Goswami.

The kind security guards at the University of Northern British Columbia who watched over me during numerous all-nighters and worked with the alarm systems at the Enhanced Forestry Lab to accommodate my bizarre schedule.

My family, Judith, Simon, Peter, and Michael Mitchell for providing me with deep seated emotional support during this journey. Thank you for the long journey to visit me at Nipika Mountain Resort.

My roommates Jeannette and Timothy Gagnon for constantly feeding me and taking great care of my dog both during the field campaign and during thesis writing sessions. Also, thank you for tremendous emotional support.

My friend Kori Cullen for both supporting and inspiring me during this journey.

My dog Daisy who has been a constant source of inspiration and joy during the thesis writing process.

Glossary

ACIS: Alberta Climate Information Service

CCRN: Changing Cold Regions Network

ECCC: Environment and Climate Change Canada

FLNRORD: Forests, Lands, Natural Resource Operations and Rural Development

Geonor: Automatic precipitation gauge designed for year round all weather measurements

MOTI: Ministry of Transportation and Infrastructure

Pluvio: Automatic precipitation gauge designed for year round all weather measurements

Precipitation Gradient: Rate of change in precipitation per unit of vertical distance

SPADE: Storms and Precipitation Across the Continental Divide Experiment

Tipping bucket rain gauge (TBRG): A precipitation gauge designed for unattended locations, consisting of a funnel and a see-saw like structure. This gauge may not perform during precipitation events with solid precipitation

Chapter 1: Introduction

1.1 Overview

Mountains are an integral component of the world's water supply. Interactions between these raised topographical features and the atmosphere can enhance precipitation rates (orographic enhancement of precipitation), ensuring that mountain ranges have a higher contribution to water supplies in comparison to other parts of their watershed (Immerzeel et al. 2020). As a consequence of these atmosphere-lithosphere interactions, the Canadian Rockies form a crucial component of North America's water supply. Two of North America's most critical water towers (important sources of water storage and supply), are located in these mountains, supplying water to both the Fraser River and the Columbia River basins as well as other basins (Immerzeel et al. 2020). However, water flows in rivers emanating from the Canadian Rockies are declining (Rood et al. 2007). Summer flows have decreased by 20% in the 20th century for rivers on the eastern slopes of the Canadian Rockies with potential consequences for forests, fish, and sediment loads (Rood et al. 2005; Rood et al. 2007). East-slope river flows are expected to decrease by an additional 10% by 2050 (Rood et al. 2007). Drying within these watersheds may have severe consequences for the Canadian Prairies since human activities and climate change have already reduced available river flows in this area that is historically drought prone (Schindler & Donahue 2006). Additionally, there is evidence that orographic enhancement of precipitation is decreasing in parts of the Canadian Rockies due to changes in wind patterns (Luce et al. 2013). Climate change could be warming minimum temperature regimes disproportionately quickly at elevated locations in these mountains and threatening water supplies through gradual snowpack reduction, if the Canadian Rockies are mirroring the neighbouring

Cariboo mountain range (Sharma & Déry 2016). Glacial recession in this area is also another factor that threatens these critical water towers and the broader water supply in North America (Marshall 2014).

Despite their crucial role in sustaining North America's water supply and their close proximity to areas with limited freshwater supplies, the mechanisms behind orographic enhancement in these mountains and moisture flux across these mountains remains poorly documented. Meteorological stations are scarce in this region and located disproportionately at lower elevations (Hik & Williamson 2019). Within the area that was selected for this study, there are about 97 meteorological stations with data accessible to the public spread across a 34,000 km^2 area. Environment and Climate Change Canada weather radar does not provide comprehensive coverage of the Canadian Rockies, specifically a focused image of both sides of the Continental Divide simultaneously. Each side of the Continental Divide appears on the edge of separate weather radars (Environment and Climate Change Canada 2020). One of the objectives of the Storms and Precipitation Across the continental Divide Experiment (SPADE) campaign is to study precipitation patterns in this region in greater detail, particularly the ability of precipitation to cross the Continental Divide. This focal point may enable us to garner a better understanding of mechanisms for orographic enhancement in the Canadian Rockies. A greater knowledge of precipitation distribution in these mountains may enable decreasing water resources to be managed more effectively.

1.2 Purpose of the SPADE Study

Overall, the SPADE experiment aimed to quantify some local meteorological variables in the Canadian Rockies to improve our understanding of regional processes and moisture flow into and across the Canadian Rockies. To characterize precipitation amounts, phases, and patterns across the Continental Divide, SPADE is integrating surface observations with a wide variety of meteorological instrumentation to accurately characterize precipitation events. The SPADE campaign was a collaborative project between several Canadian universities that examined moisture fluxes and condensate across the Continental Divide in the southern Canadian Rockies. This project allowed us to gather precise and detailed meteorological data at specific sites over a two-month period between 26 April and 26 June 2019 in a section of the southern Canadian Rockies over the Continental Divide. Human observers worked alongside meteorological instruments, providing additional observations of the atmosphere including identification of cloud types and precipitation phases. By combining human observations with precipitation measurements, we were able to better identify temperatures at which phase transitions were occurring and to determine what type of synoptic events were responsible for precipitation. This campaign allowed us to characterize precipitation events as they were occurring, and provided us with a portrait of moisture fluxes and condensate in the Canadian Rockies.

1.3 Significance of the Study within Hydrometeorology

The Canadian Rockies are part of the hydrographic apex of North America (Rood et al. 2005), comprising of many peaks between 3000 to 3500 m in elevation. The hydrographic apex lies at the triple divide on the Continental Divide, a ridge from which water flows into the Arctic, Atlantic and Pacific Oceans (Rood et al. 2007). Atmospheric systems from the Pacific, Arctic, and Atlantic Oceans influence each of the watersheds connected to the Continental Divide; therefore, this area receives moisture input from a wide variety of weather systems, creating a strategic location from which to study both local and broader atmospheric processes (Rood et al. 2005).

As a consequence of being a hydrographic apex, the Canadian Rockies form the headwaters of several major river systems including the Fraser, the Columbia, and the Saskatchewan that provide water, hydroelectricity, or food (through agriculture and fisheries) to large populations in western Canada and beyond. Waterways in Saskatoon, Edmonton, Calgary, Vancouver, and various other cities are shaped by hydrological cycles in the Canadian Rockies. To be able to predict current or future fluctuations in these critical waterways, it is crucial that we understand their inputs through an evaluation of precipitation, particularly in their headwaters.

As with most southern regions in Canada, upper-level processes have been examined above the Canadian Rockies. However, given the sparsity of meteorological stations in this region and the complexity and heterogeneity of the terrain, gridded meteorological data which represent historical interpolations, such as the Pacific Climate Impacts Consortium (PCIC) ensembles, perform poorly. This contributes to an inadequate understanding of local meteorological processes (Wong et al. 2017).

Precipitation gradients can be persistent within the landscape; however, precipitation varies with temperature and season (Anders et al. 2007; Milewska et al. 2009). Therefore, a holistic understanding of precipitation gradients requires an examination across temperature regimes, specifically above and below temperatures at which rainfall transitions to snowfall. Given inter-seasonal and inter-annual variability in precipitation (Shea & Marshall 2007), precipitation gradients should be examined across seasons and across years to determine their persistence in the landscape.

Precipitation amounts vary around the Continental Divide. Recurrent orographic forcing on the western side of the Continental Divide causes air masses to become drier and precipitation amounts to decrease, creating a precipitation shadow effect directly on the eastern side of the Continental Divide (Moran et al. 2007). The presence of a rain shadow has been postulated through a comparison of data from a meteorological station located 800 m east of the Continental Divide at 2674 m above sea level, to meteorological measurements taken in Calgary, Alberta (AB) which is located about 100 km east of the Continental Divide at an elevation of 1045 m above sea level (Moran et al. 2007), but this study did not examine the precipitation-elevation relationship between these two sites. The Foothills Orographic Precipitation Experiment (FOPEX) identified some relationships between precipitation and elevation in the nearby Alberta Foothills, from Limestone Mountain to Caroline, AB, but it focused exclusively on precipitation on the eastern side of the Continental Divide (Smith 2008).

As the apex of our continent, the Continental Divide would provide insights into orographic lift at some of the highest elevations in southern Canada. A study at this site would also yield a comparison of precipitation gradients on both the eastern and western sides of the Continental Divide, providing insights into atmospheric moisture originating from the Pacific, the Arctic, and from the Gulf of Mexico (Rood et al. 2005). Greater information on localized orographic enhancement and precipitation shadows would enhance our ability to predict hydrological inputs in the region and provide insights into broader atmospheric processes.

Orographic precipitation enhancement processes, or the processes by which precipitation rates are enhanced by air being lifted over mountains (often enhancing precipitation at higher elevations) can be a large determinant of regional water balances in an area with complex mountainous topography (Luce et al. 2013). Therefore, an examination of precipitation gradients across a range of elevations may allow us to refine our understanding of meteorological processes within this region. However, given the rugged terrain and dynamic meteorology of this region (Thériault et al. 2018), many challenges exist in accurately evaluating precipitation in this area.

One method to estimate precipitation amounts in rugged terrain with sparse meteorological information could be to define the precipitation-elevation relationship, or quantify precipitation gradients within the region. Given an understanding of changes in precipitation with elevation, existing meteorological data could be extrapolated to other parts of the landscape at different elevations.

My research objectives are tailored for two larger goals. One aim of my research is to examine SPADE precipitation events in greater detail and to contextualize them in terms of topography, regional precipitation patterns, and other meteorological phenomena. Another aim of my research is to examine how precipitation patterns change with time and to identify some meteorological and topographical variables that might be responsible for precipitation gradients.

The objectives of this research are to:

- Determine the magnitude of orographic enhancement across SPADE stations.
- Determine if localized patterns during precipitation events at SPADE stations are representative of regional patterns.

- Determine how elevation, longitude, latitude, wind, and temperature influence precipitation gradients.
- Explore the equivalence of reanalysis products to station data to determine if ERA5-Land data can be used as a replacement for station data.
- Examine precipitation from the 2011 to 2019 period across a variety of time periods such as between SPADE periods (26 April to 26 June), between seasons, and between years to determine how gradients change with time.

1.4 Research Questions

1. How does elevation influence precipitation gradients across the Continental Divide?
2. Can differences in precipitation gradients be detected between cool and warm seasons?
3. What is inter-annual and intra-annual variability in precipitation gradients in this region?
4. How do general wind patterns/storm trajectories affect precipitation gradients?

Precipitation gradients provide useful depictions of changes in hydrometeor density across the landscape that could be used to inform hydrological management regimes. Given that changes in mountain hydrology are occurring and are likely to persist (Sharma & Déry 2016), maps of current precipitation regimes are critical for determining current inputs into hydrological systems. Therefore, identifying precipitation gradients in the Canadian Rockies within the SPADE study area and factors involved in their creation is a particularly useful endeavour.

This thesis is divided into chapters, with each chapter containing a different constituent of the research process. Chapter 2 contains a literature review, Chapter 3 contains an outline of the instruments and methodology, Chapter 4 contains some results of this project, and Chapter 5 provides discussion and some research limitations. Chapter 6 provides conclusions, some broader impacts of this work, and some recommendations for future work.

Chapter 2: Literature Review

This chapter provides a review of existing literature regarding mechanisms behind orographic enhancement of precipitation and examines some of the challenges associated with identifying precipitation gradients within the landscape, such as temporal limitations, convective activity, and problems associated with accurately measuring precipitation. A general overview of precipitation patterns near the Continental Divide is also provided.

2.1 Cloud formation

For precipitation to occur areas of water droplet/ice crystal aggregation, or clouds need to form in the atmosphere (Ahrens et al. 2012). Clouds primarily form through convection, convergence of surface air, or uplift along frontal boundaries or along topographical features (Ahrens et al. 2012). Greater amounts of cloud cover occur over mountains in comparison to their surroundings (Barry 2008). This increased cloud cover is the result of both atmospheric conditions (namely moisture content and atmospheric stability) and uplift caused by the mountains (Barry 2008). Two main mechanisms by which clouds form in the mountains are direct forced ascent, and thermal forcing (Barry 2008). Through these mechanisms, mountains can enhance the amounts of precipitation that occur on the landscape relative to flat or undulating terrain.

2.2 Orographic enhancement

Orographic enhancement of precipitation is critical to the manner in which the atmosphere and the lithosphere interact (Roe 2005), and it can be an important contributor to precipitation distribution (Luce et al. 2013). This type of precipitation enhancement arises through airflow that has been redirected in a more vertical direction by topography (Roe 2005; Ahrens et al. 2012). When an unsaturated parcel of air encounters elevated terrain and is forced to ascend, this parcel expands adiabatically, and due to an associated drop in pressure, it cools as it rises (Roe 2005). Due to cooling processes, the vapour that this parcel carries may reach saturation. Since vapour pressures cannot exceed saturation values by more than ~1%, a rising parcel's excess water vapour condenses into cloud particles. In turn, hydrometeors can form from this condensed water vapour. Orographic enhancement may create a region of enhanced condensation, but there are many mechanisms by which this condensation may become hydrometeors (Roe 2005).

The simplest form of orographic enhancement of precipitation is upslope ascent, where an air parcel is mechanically forced up a mountain slope by wind (Roe 2005). However, a variety of complex processes can influence orographic enhancement of precipitation including wind speed, slope gradient, atmospheric stability, and moisture content.

2.3 Overview of wind in orographic enhancement

Wind intensity and direction can have a direct relationship with the magnitude of orographic enhancement that occurs in a given area (Colle 2004; Johansson & Chen 2003; Luce et al. 2013; Roe 2005). In one numerical modelling study, three different wind speeds created different precipitation profiles for the same mountain model (Colle 2004). In model runs with the lowest wind speed, precipitation maxima tended to occur further upwind of the mountain than other wind speed categories (Colle 2004). Meanwhile, model runs with the fastest wind speed had precipitation spread more widely across the upwind mountain surface, and advected more precipitation into the lee than other speed categories (Colle 2004).

Wind is a good indicator of many characteristics of broader meteorological phenomena such as frontal systems, and can be used to classify air masses that are responsible for precipitation events, which in turn can be used to determine relative precipitation amounts (Johansson & Chen 2003; Moran et al. 2007; Shea & Marshall 2007; Stockham et al. 2018). However, not only is wind a factor in orographic precipitation enhancement (Anders et al. 2007; Johansson & Chen 2003; Mott et al. 2014), it can also move precipitation maxima across the landscape (Mott et al. 2014). If winds intensify during a precipitation event, a precipitation maximum may move from the windward flank or the apex of a ridge, to the lee of a ridge (Mott et al. 2014; Roe 2005). Maximum precipitation amounts often occur on a windward flank for large mountains, but at the crest for smaller ones (Roe 2005). Wind also moves frontal systems that are responsible for precipitation (Shea & Marshall 2007) and may cause these storms to change (Roe 2005). Therefore, although winds can determine characteristics of precipitation gradients on a landscape, they can simultaneously alter them.

Prevailing westerly winds may form an integral part of orographic enhancement in the Pacific Northwest of the United States (Luce et al. 2013). However, in the Canadian Rockies, although there are prevailing westerlies (Shea & Marshall 2007), precipitation events may result from northwesterly flow (Moran et al. 2007), from upslope flow from the east (Thériault et al. 2018; Moran et al. 2007), or from southwesterly flow (Shea & Marshall 2007; Sinclair & Marshall 2009). Prevailing wind direction can be instrumental in determining where windward orographic precipitation occurs through horizontal moisture and condensate convergence near a mountain barrier (Mo et al. 2019; Mo et al. 2021).

2.4 Other variables in orographic enhancement

Slope is also an important factor in precipitation enhancement. In a statistical analysis of the effects of wind and topography, an important factor in determining precipitation enhancement was slope multiplied by wind speed (Johansson & Chen 2003). However, if slope length extends too far, an air mass may be blocked by the slope, stagnate and be forced along the edge of the slope. In some cases, slower winds stagnated when exposed to the highest elevation mountains in model runs, bringing precipitation maxima further upwind (Colle 2004).

Mountain locations in relation to consistent sources of moisture may determine the amounts of precipitation enhancement that occur. The Washington Cascades, a coastal mountain range in the US state of Washington, exhibit some of the strongest precipitation gradients in the world (Siler et al. 2013). In a study conducted in Sweden, sites located close to the coast exhibited the greatest precipitation enhancement due to slope (when multiplied by wind speed) (Johansson & Chen 2003). This effect was reduced for mountains further inland, particularly those with upwind obstacles (Johansson & Chen 2003).

If the atmosphere is too stable, or advecting winds are too light, an air mass may become trapped at the base of a mountain where it might be re-directed or it might stagnate, forcing orographic influence further upwind (Roe 2005; Luce et al. 2013; Colle 2004). Subsequently, this stagnant air mass may enhance lifting of an oncoming air mass (Roe 2005). Additionally, strong atmospheric stability can create gravity waves, allowing a parcel to ascend before the windward flank of a barrier (Roe 2005). Conversely, orographic enhancement may have an even larger positive impact on precipitation rates when orography triggers unstable convection in an ascending air mass, which could lead to greater condensation rates and more efficient fall out of precipitation (riming on solid particles might be a consequence of this) (Roe 2005; Thériault et al. 2015).

Orography can result in decreased precipitation when upwind barriers block wind from advecting air masses, decreasing orographic enhancement (Johansson & Chen 2003).

Precipitation that is melting or evaporating can create cool winds that may flow against an ascending air mass, which may slow or block it, limiting subsequent orographic enhancement of precipitation (Roe 2005). If this airflow is redirected, precipitation could result, particularly if this diversion leads to flow convergence (Roe 2005).

2.5 Temporal and spatial variability in orographic enhancement

Tremendous variability in orographic enhancement does not only exist between storms, but within storms. Precipitation rates can be altered during the storm, due to air mass stagnation, or convective processes, as the storm evolves (Roe 2005). Formation/degradation of precipitation exchanges latent heat with the surrounding air, which results in changes to airflow patterns (Roe 2005). Orographically induced clouds can also interact with passing clouds to increase precipitation enhancement by fostering seeder-feeder mechanisms and enhancing precipitation from passing storm clouds (Roe 2005). Despite many exceptions, in general, orographic enhancement of precipitation facilitates cooling of air parcels and condensation on windward slopes, and warming of descending air parcels on the lee of the slope (Roe 2005).

At a national scale, precipitation over Canada varies considerably, with the largest amounts of precipitation occurring near the coasts (a source of moisture for precipitation formation) and on mountain slopes facing west towards the predominant wind direction (Ahrens et al. 2012). In the mountainous regions of British Columbia (BC), precipitation amounts diminish with increasing distance from the moisture source, the Pacific Ocean (Figure 2.1). This trend results in precipitation gradients, or decreases/increases in precipitation amounts over space.

.

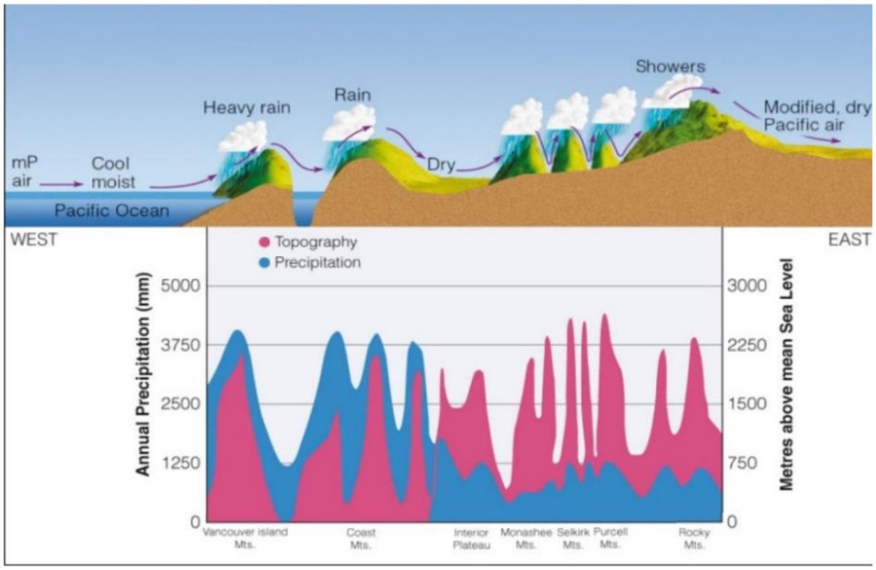

Figure 2.1. Average annual precipitation varies due to topography in an east-west transect across southern British Columbia between the Pacific Ocean and the Canadian Rockies (from Ahrens et al. 2012).

Annual precipitation amounts decrease by two thirds in a west to east transect across southern BC (Ahrens et al. 2012). Increases in elevated topographical relief are linked to increases in annual precipitation; however, inland mountains with greatest topographical relief do not receive the greatest amounts of precipitation, since interactions with the topographical features to the west have removed moisture from westward moving air masses (Ahrens et al. 2012).

2.6 Convection and precipitation gradients

Convection is a prominent source of precipitation in the Rockies during summer months (Barry 2008; Feng et al. 2019). Large cumulus clouds result from valley flows and thermal convection over the eastern Canadian Rockies (Barry 2008). Convective formation in this region is enhanced by strong diurnal heating in the Rocky Mountain Foothills and this heating causes upward motion that can initiate thunderstorms (Ahrens et al. 2012; Feng et al. 2019). Convection could make identifying precipitation gradients difficult. In a study conducted on precipitation in the Alberta Foothills, significant linear correlations were more difficult to establish during summer months, possibly due to greater spatial variability in convective precipitation at this time of year (Smith 2008).

2.7 Larger scale atmospheric processes and precipitation gradients

A study in the United Kingdom designed to examine the rain shadow effect in the Peak District found that, not only were orographic processes responsible for these precipitation gradients, but continental air masses were also involved (Stockham et al. 2018). Global weather patterns may also influence precipitation gradients at the local level. The east-west precipitation gradient in Washington's Cascade Mountains has a strong relationship with the El-Niño Southern Oscillation (ENSO), which is a periodic variation in sea surface temperature and winds in the eastern Pacific Ocean, thousands of kilometres away (Siler et al. 2013). Precipitation gradients may also be dependent upon their location within a mid-latitude cyclone (Mass et al. 2015).

2.8 Temporal variation in precipitation gradients

Isolating precipitation gradients through time may be challenging. Given the variability of precipitation, gradients may not become immediately apparent in smaller events (Roe 2005). In one study near the Continental Divide in the Canadian Rockies, each snowstorm event that was studied produced a different amount of snow, and a different spatial distribution of precipitation across the study area (Moran et al. 2007). However, if precipitation data were examined across several years, a rain shadow phenomenon could be identified in this region (Moran et al. 2007). Conversely, an application of a linear model revealed that persistent precipitation gradients exist on the Olympic Peninsula, despite annual precipitation amounts that varied by about 20% between 2000 and 2001 (Anders et al. 2007). These studies indicate that although precipitation gradients may be persistent across a given landscape, their presence might only be detected across a suitably long time-frame.

2.9 Challenges with accurately characterizing precipitation

Precipitation can be measured in numerous ways including ground based observations such as precipitation gauges and ground based meteorological radar profilers and laser weather sensors, through to remote sensing such as weather radars and satellite images. Unfortunately, our study area is remotely situated in relation to weather radars. Each side of the Continental Divide appears on a different weather radar and the large distance between radar stations and our domain means that radar beams may overshoot certain weather phenomena, may be blocked by topography, or may be attenuated by storms closer to the radar. Additionally, virga may be interpreted as surface precipitation at these sites (Environment and Climate Change Canada 2020). To fill some of the gaps in precipitation measurements in weather radar, this study employs networks of precipitation gauges in situ. This is the global standard and the most reliable method by which precipitation is measured at a specific location. Unfortunately, inconsistencies in gauge-based precipitation measurements can be the result of dissimilar types of precipitation gauges being employed. Different types of precipitation gauges can have dissimilar performance because of variables such as wetting loss and heat capacity that are linked to their construction. In the case of wetting loss, water may evaporate from the surface of the orifice or the inner walls of the precipitation gauge, and these rates vary according to the type of materials that are used in the precipitation gauge (Wang et al. 2017).

Wind-induced undercatch of precipitation depends largely on whether or not the gauge is shielded from the wind, with shielded gauges having a greater capacity to collect precipitation in comparison to non-shielded gauges (Colli et al. 2015; Milewska et al. 2019; Kochendorfer et al. 2021). This discrepancy in catch rates means that wind shields can be a principal feature of accurate snow measurement. Precipitation loss due to wind-induced undercatch continues to be one of the biggest challenges for the accurate appraisal of precipitation in an automated gauge (Milewska et al. 2019). Wind interactions with a precipitation gauge creates turbulent updrafts that prevents precipitation from entering the gauge, and the strength of these updrafts varies with wind speeds. (Pollock et al. 2018; Milewska et al. 2019). Alter shields counteract the eddies that prevent precipitation from entering the gauge orifice, diminishing the amount that catch efficiency decreases with wind (Colli et al. 2015; Milewska et al. 2019; Muchan & Dixon 2019; Kochendorfer et al. 2021). Each gauge and shield configuration responds differently to environmental conditions (Mekis et al. 2018; Pollock et al. 2018; Kochendorfer et al. 2021). Therefore, cumulative precipitation amounts may differ between sites depending on whether sites are shielded or not and what type of shields are employed.

Precipitation gauges perform differently in response to solid or liquid precipitation, with automated weighing gauges outperforming tipping buckets during solid precipitation events (Mekis et al. 2018). Tipping buckets are not very effective at capturing solid precipitation events, they often delay the recording of precipitation since it is unable to enter the funnel until the solid precipitation has melted. There may be adhesion of precipitation to the debris-filtering screen or funnel, limiting recording of precipitation due to evaporation. Tipping buckets often freeze during the winter, and consequentially function poorly below freezing temperatures unless they are heated tipping buckets. Tipping buckets also underestimate rainfall during intense storm events (Duchon & Biddle 2010; Mekis et al. 2018). However, snow capping of an automated weighing gauge can lead to extended periods in which precipitation data are underreported (Milewska et al. 2019). Additionally, solid and liquid precipitation cannot be separated at automated weighing gauges since only total precipitation is recorded (Milewska et al. 2019).

Automated weighing gauges are also susceptible to changes in precipitation measurements due to variations in wind or temperature (Mekis et al. 2018). Automated weighing gauges provide a better measurement device for all seasons precipitation than tipping buckets due to their increased efficacy at sub-freezing temperatures (Duchon & Biddle 2010; Mekis et al. 2018). Networks in this study area were largely comprised of automated weighing gauges or tipping bucket rain gauges with a couple of measurement sites where precipitation was recorded manually (Section 3.3).

Quality control with wind adjustments will likely increase the amount of precipitation that is measured (Duchon & Biddle 2010; Pollock et al. 2018; Milewska et al. 2019). However, since automated and remote tipping bucket rain gauges are not monitored there is a limit to the amount of metadata that is available regarding precipitation, and consequently a limit to how much quality control can be done, on these gauges (Mekis et al. 2018).

Different user groups require different quality data (Mekis et al. 2018), and consequently different levels of quality control. Therefore, an entire network may be designed according to the types of data that are required by a specific user group, and this network may have a specific type of quality control protocol that can differ from neighbouring stations. For example, the BC Ministry of Forests, Lands, Natural Resource Operations and Rural Development (FLNRORD) stations are geared towards fire weather and have fewer quality control procedures than the Alberta Climate Information Service (ACIS) (ACIS 2020-2022) stations that are geared towards agriculture.

Various environmental factors influence catch rates within networks or between networks. The temperature of solid precipitation affects catch efficiencies. Snow with a temperature below 3°C is more prone to wind-induced undercatch (Milewska et al. 2019). Precipitation also has considerable weather dependent errors between stations caused by different freezing conditions, different physical characteristics in precipitation, and spatial variability in precipitation (Mekis et al. 2018). Some scales of precipitation are missed in station networks, because meteorological stations within these networks do not have the spatial distribution that is required to capture them, particularly in remote regions of Canada. However, meteorological stations remain the most accurate point source of information regarding the accumulation of precipitation (Wang et al. 2017).

Chapter 3: Study Area, Data, and Methods

This chapter provides a characterization of the SPADE study area and the data collected during the SPADE campaign using SPADE equipment and other instrumentation in the area. This chapter also outlines methods used for data collection and some of the procedures that were used to process data along with some of the quality control procedures.

3.1 SPADE Study Area

The Continental Ranges of the Canadian Rockies encompass the SPADE study area, a region comprising of rugged topography. Steep westward dipping faults, elevated mountain passes, and some of the highest peaks in the Canadian Rockies distinguish this area (Bobrowsky & Rutter 1992). Below treeline, vegetation in this region includes Engelmann spruce, white spruce, alpine fir, and lodgepole pine (Bobrowsky & Rutter 1992). This mountainous landscape includes the Continental Divide, which is the highest barrier to precipitation in southwestern Canada (Bobrowsky & Rutter 1992; Sinclair & Marshall 2009).

A dominant meteorological feature of this region is the prevailing westerlies, which facilitate the transport of moisture from the Pacific Ocean across southern British Columbia and into the Canadian Rockies through the passage of mid-latitude cyclones in an eastward direction (Bobrowsky & Rutter 1992; Sinclair & Marshall 2009). This north-south orientated mountain range is a barrier to westerly flow and creates orographic uplift which, in turn, facilitates orographic enhancement of precipitation (Bobrowsky & Rutter 1992; Sinclair & Marshall 2009). This phenomenon is typified at this location by precipitation on westward slopes and warming of air masses, leading to cloud dissipation on the eastern side of the Canadian Rockies (Bobrowsky & Rutter 1992).

Westerly winds advect maritime polar air masses from the Pacific into the Canadian Rockies; however, continental polar air masses, which are air masses that originate in northern Canada, also define the climate of this region since the Canadian Rockies often block the westward flow of these air masses from the prairies during the winter (Sinclair & Marshall 2009; Bobrowsky & Rutter 1992).

Although glacierized areas in the Canadian Rockies experience a snow accumulation period from October to June, there is significant variation in precipitation across the geographical extent of the Canadian Rockies (Bobrowsky & Rutter 1992; Sinclair & Marshall 2009). To capture precipitation variation, SPADE deployed several surface observational stations on both sides of the Continental Divide. Meteorological stations at Fortress Mountain, Fortress Junction, and the Biogeoscience Institute (BGI) provided measurements on the eastern side of the Continental Divide (Table 3.1 and Figure 3.1), while Nipika Mountain Resort (Nipika) and a precipitation gauge transect provided precipitation measurements on the western side of the Continental Divide.

Table 3.1. SPADE surface station locations and periods of operation. (Refer to Appendix A for intervals in which stations were inoperable during these periods of time).

Station	Coordinates	Elevation (masl)	Period
Nipika Mountain Resort (Nipika)	50.6118° N, 115.8008° W	1087	21 September 2018 – 26 June 2019
Fortress Junction	50.7856° N, 115.1608° W	1580	24 April 2019 - 26 June 2019
Fortress Mountain	50.8242° N, 115.1972° W	2076	24 April 2019 - 26 June 2019
Biogeoscience Institute (BGI)	51.0267° N, 115.03441° W	1418	25 April 2019 – 25 June 2019
Precipitation Gauge Transect	50.69025° N, 115.76490° W 50.73336° N, 115.6615° W 50.7416° N, 115.5061° W	1198 1220 1667	11 May 2019 – 23 June 2019 11 May 2019 – 23 June 2019 11 May 2019 – 23 June 2019

3.2 Study Area

Three surface observational stations were operational for the duration of the SPADE field campaign. These sites, Fortress Junction, Fortress Mountain, and Nipika Mountain Resort (Nipika), provided continuous data, which will form the initial inputs for my comparison of precipitation gradients across the Continental Divide (Figure 3.1).

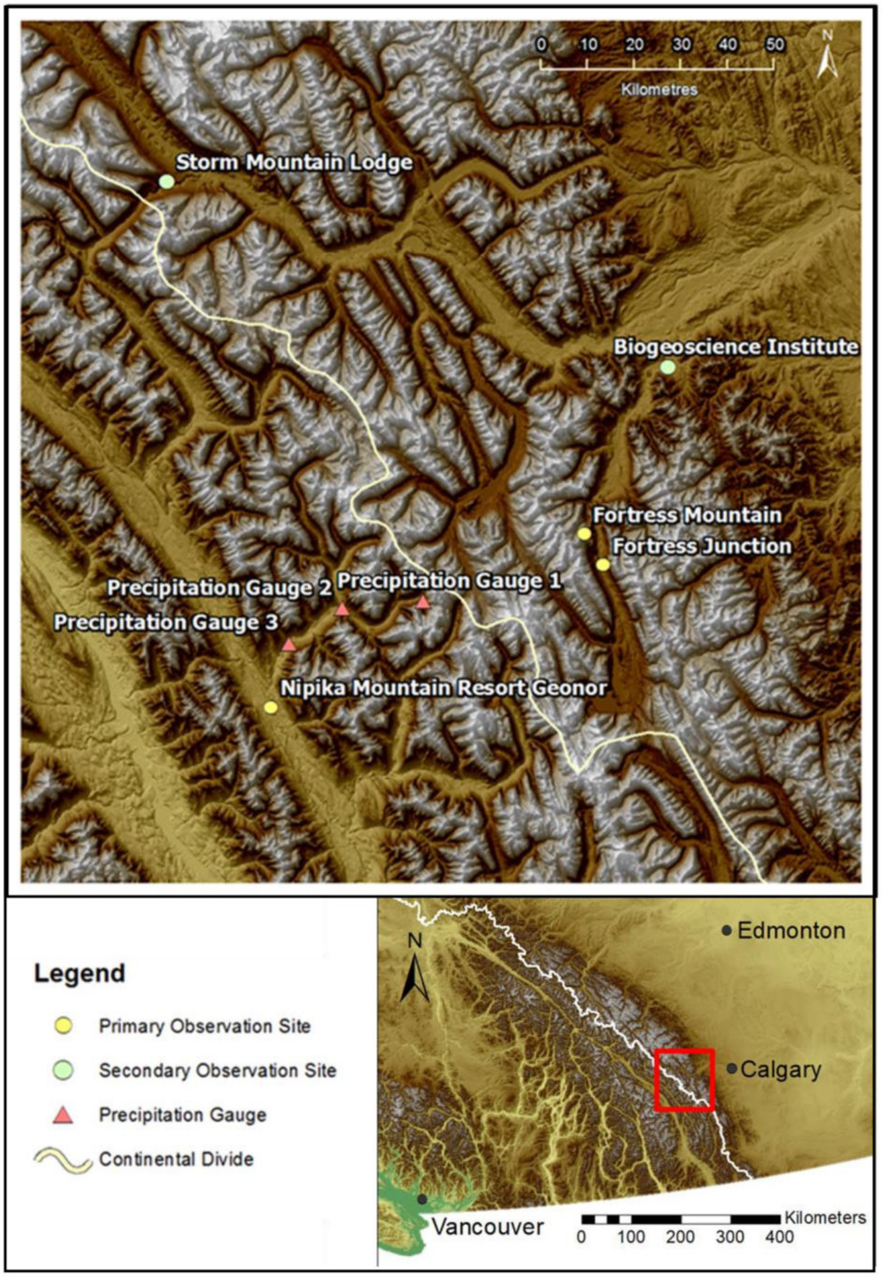

Figure 3.1. Three primary observation sites for SPADE: Fortress Junction, Fortress Mountain, and Nipika Mountain Resort (Nipika) (yellow circles). A transect of tipping bucket rain gauges (TBRGs) (red triangles) provided additional information regarding precipitation gradients. The three tipping bucket rain gauges and the Nipika Mountain Resort Geonor (Nipika Geonor) comprised the precipitation gauge transect. Two secondary observation sites (green circles) were deployed on a temporary basis to enhance our understanding of meteorological processes on the edge of the SPADE domain.

Fortress Junction was located 5 km south of Fortress Mountain in the same watershed on the eastern side of the Continental Divide, with a 500 m difference in elevation. Fortress Junction was located in an open field at the bottom of a mountain valley, while Fortress Mountain was located in an alpine meadow on the edge of a plateau overlooking Fortress Junction (Figure 3.2). Both of these stations were located 20 km east of the Continental Divide. Many snow-clad peaks with elevations upwards of 2500 m above sea level surrounded these stations. Nipika was the lowest station in the SPADE project situated at about 500 m below Fortress Junction. Located in a small clearing at the bottom of a mountain valley near the Kootenay River 30 km west of the Continental Divide. It was surrounded by mixed forest and mountains with elevations upwards of 2500 m above sea level, however the ridges near this station were considerably lower than this. The locations of the three main meteorological stations that provided baseline data from each side of the Continental Divide during the SPADE period was determined prior to this study. This configuration of stations allowed precipitation to be examined on either side of the Continental Divide and for potential effects of orographic enhancement of precipitation to be examined as well.

In addition to the meteorological sites that were deployed for the duration of the SPADE campaign, we deployed three tipping bucket rain gauges (TBRGs) between 11 May 2019 and 23 June 2019. These TBRGs were deployed as a transect along the Cross River Valley, which is oriented in a northeasterly direction between Nipika and the Fortress sites. The Nipika Mountain Resort Geonor (Nipika Geonor) was included as the lowest elevation station along this transect. The lowest elevation TBRG was located at 1198 m at 50.69° N, 115.76° W, the mid-elevation TBRG was located at 1220 m above sea level at 50.73° N, 115.66° W, while the highest elevation station was located at 1667 m above sea level at 50.74° N, 115.50° W. These sites were chosen so that the TBRGs were roughly equidistant from each other in a straight line transect along the Cross River Valley.

Figure 3.2. Primary observation sites for SPADE from east to west include Fortress Junction (top left), Fortress Mountain (top right), and Nipika (bottom). All three of these sites contained a variety of meteorological instruments and were visited frequently throughout the SPADE campaign by weather observers. (Photo credit: Juris Almonte).

The goal of my section of the SPADE study develops a comprehensive understanding of precipitation gradients in the Canadian Rockies over the Continental Divide. To achieve this, this project will examine precipitation gradients from the Columbia River Valley on the western margin of the Canadian Rockies through to the Foothills on the eastern margin of the Canadian Rockies.

The western edge of my study area was defined by the convergence of the Columbia River Valley with the Purcell Mountains. This design intentionally excludes most of the Purcells from the study area since these mountains are hydrologically distinct from the Canadian Rockies. These mountains are closer to the Pacific Ocean, therefore they receive higher amounts of annual precipitation than the Canadian Rockies (Ahrens et al. 2012, Figure 17.5).

My study area encompassed the headwaters of the Columbia River (Columbia Lake) near Canal Flats through to where the Columbia River enters Kinbasket Lake. This ensured that the highest and the lowest points of the Columbia Valley are included in my study area (Figure 3.3).

The eastern margin was defined by sites that most closely matched the elevation of Nipika within the foothills of the Canadian Rockies, without extending the study area into regions where mountainous topography flattens in the prairies. Including sites with similar elevations to Nipika was important so that I could exclude elevation from my comparisons of air mass characteristics on either side of the Continental Divide. The Foothills Orographic Precipitation Experiment (FOPEX) (Smith 2008) occurred near this area in the Foothills at a similar elevation to my study area (between 1070 m and 2120 m above sea level), so I will use this study to inform my own findings in this region.

Precipitation gradients will be identified using meteorological data from surface-based stations (Tables 3.2 and 3.3) and gridded data products. A combination of surface-based stations and gridded data is necessary for an evaluation of precipitation gradients in this region since conventional surface-based stations are sparse, particularly at higher elevations. Unfortunately, modelled data can also have poor outputs at higher elevations (Sharma &

Déry 2016). Therefore, obtaining information from higher elevation research stations was a priority for this study.

3.3 Meteorological Data

This study collected as many surface observations as possible within the domain. However, to ensure that observations represented stable local patterns, stations with measurements from 2011 to 2019 were prioritized (one of the longer time-frames for ACIS stations). The spatial domain was extended in some areas to incorporate as many of these longer term stations as possible. Some stations that did not contain several years of data were included to improve the spatial resolution of precipitation gradients and homogeneity of the dataset. Since surface-based stations are operated by a variety of organizations that range from provincial and federal agencies to research institutions, this study may be affected by inconsistencies in precipitation measurements both between and within these groups. Dissimilarities between networks could limit our ability to perform uniform wind-induced undercatch adjustments in our study area, as each type of gauge has its distinct interaction with wind. Other quality control procedures could be impacted by network heterogeneity as well.

Frequency of measurement also impacts the amount of precipitation that is recorded by a precipitation gauge, with the potential for evaporation likely increasing between capture and measurement as the measurement frequency decreases, particularly with manual gauges. Networks in this study domain recorded precipitation at intervals ranging from 15 minutes to daily intervals. SPADE instruments used time intervals ranging from one minute to an hour.

The level of quality control used in a station network also influences the amount of precipitation that is recorded by a specific rain gauge. Careful quality control could eliminate erroneous spikes introduced by human or natural causes, such as snow capping or maintenance, and could diminish precipitation loss caused by evaporation or periods of drying. The importance of quality control at weighing gauges was demonstrated during another study conducted in southwestern Alberta. Precipitation amounts increased by 39% to 49% at a weighing gauge located on a ridge that was 2130 m above sea level and exposed to alpine conditions (Barnes & Hopkinson 2022). They increased by -4% to 1% at weighing gauges in montane valleys after correct quality control procedures were applied to annual precipitation data (Barnes & Hopkinson 2022). Station networks had very different levels of quality controls with some networks receiving daily quality control (ACIS) with other networks (FLNRORD) having no documented quality control.

3.4 Precipitation Gauges within the SPADE Domain

Precipitation gauge types vary between meteorological stations. Given the sparse population of the Canadian Rockies, most precipitation is measured automatically. In Canada, total precipitation is measured automatically using tipping bucket rain gauges (TBRGs), weighing gauges, and optical sensors. Ultrasonic snow depth sensors can be used to determine total snowpack depth (Mekis et al. 2018). TBRGs measure precipitation as it passes through an orifice in the top of a bucket, where precipitation causes a see-saw like container to move when a prescribed amount of precipitation has been obtained. Weighing gauges (a category that includes standpipe gauges) measure precipitation by weighing total precipitation through time. Total precipitation is collected in a bucket and discharged from the bucket once it is full. Optical sensors use a measurement of optical scatter, which is often combined with other sensor technologies, to achieve measurements of precipitation frequency and amounts. Meanwhile, snow depth sensors use ultra-sonic frequencies directed at a specific location on the snow to measure changes in snow depth. Each type of precipitation gauge is susceptible to error.

In addition to problems with wind-induced undercatch and their inability to measure snow density, automated gauges are incapable of automatically identifying precipitation phase. Additionally, these gauges may experience undercatch or precipitation accretion on the sides of the orifice, or evaporation of collected precipitation and this source of error may go unidentified (Pan et al. 2016; Kochendorfer et al. 2017). Error introduced by wind, temperature, and evaporation can all contribute to a decreased accuracy in the precipitation measurement. Automated weighing gauges may experience errors due to the impacts of rapidly changing thermal regimes on transducers or by being located on an uneven surface. Additionally, errors may develop in data during maintenance and charging of the stations when sensors are not suppressed (Mekis et al. 2018).

TBRGs fill slowly during solid precipitation events, therefore there is a delay in precipitation reporting. Additionally, adhesion of precipitation to the edges of the orifice or the filter, the introduction of dirt into the system, or splashing can introduce error into the measurements, or captured precipitation can freeze inside the TBRG rendering it inoperable. Meanwhile, snow movement such as deposition, erosion, and sublimation can create errors in ultrasonic snow depth sensor measurement. The ultrasonic snow depth sensor site is only representative of very localized conditions, given that snowpack varies considerably across a landscape. Additionally, the snow target may mirror nearby ground conditions (Mekis et al. 2018).

There are some stations in the Canadian Rockies where observers collect precipitation amounts manually using gauges such as the Type B rain gauge, the Nipher snow gauge, and manual snow rulers. Manual gauges are prone to many of the same errors as automatic gauges, including precipitation loss due to wind undercatch and evaporation (Mekis et al. 2018).

A wide variety of different precipitation gauges were used to collect precipitation by various organizations within the study area. Networks such as CCRN and ACIS provide information on their instrumentation and potential errors on their websites. Meanwhile, information on MOTI and ECCC stations was provided by technicians. Surface precipitation measurements come from a variety of sources including weighing gauges, TBRGs, optical sensors, and ultrasonic snow depth sensors. Most surface data in this study are at an hourly interval. The CCRN network has many stations where data are recorded at 15 minute intervals, while a station at Golden Airport and a manual station at Kootenay West Gate, and Kananaskis has measurements over daily periods.

Data from MOTI stations were only used for some analyses. MOTI stations utilize standpipe gauges fitted with transducers to collect precipitation data. These gauges are prone to evaporative loss and oscillations induced by other environmental variables. Therefore, data from these gauges were largely excluded from my study. These stations were used for some analyses over longer time periods. However, the fluctuations in precipitation values and the high rates of precipitation loss due to evaporation that occurred at these stations meant that they were not suitable for analyses over shorter time periods.

Depending on the network, data may also contain some seasonality. MOTI stations, for example, are maintained from October through to May, with only a few stations that are being used for climate analysis being maintained year round (e.g. Vermillion Pit). Conversely, FLNRORD stations focus on fire suppression, so they may not be maintained during winter months. One source of error for all long-term stations may be undocumented changes in instrumentation.

Table 3.2. Number of stations in each dataset with surface observations from the last 10 years within my study area.

Name	Acronym	Number of stations in a dataset				
		Annual	Seasonal	2019 SPADE Events	2019 Total SPADE Period	SPADE periods from 2011 to 2019
Storms and Precipitation Across the Continental Divide Experiment	SPADE	0	0	3	3	0
Alberta Climate Information Service	ACIS	37	35	55	55	53
Environment and Climate Change Canada	ECCC	0	0	3	3	0
BC Ministry of Transportation and Infrastructure	MOTI	0	0	8	8	0
BC Ministry of Forests, Lands, Natural Resource Operations, and Rural Development	FLNRORD	6	6	9	8	7
Changing Cold Regions Network	CCRN	0	0	17	13	0
BC Hydro	None	0	0	1	1	0
Total number of stations for each period		43	41	96	91	60

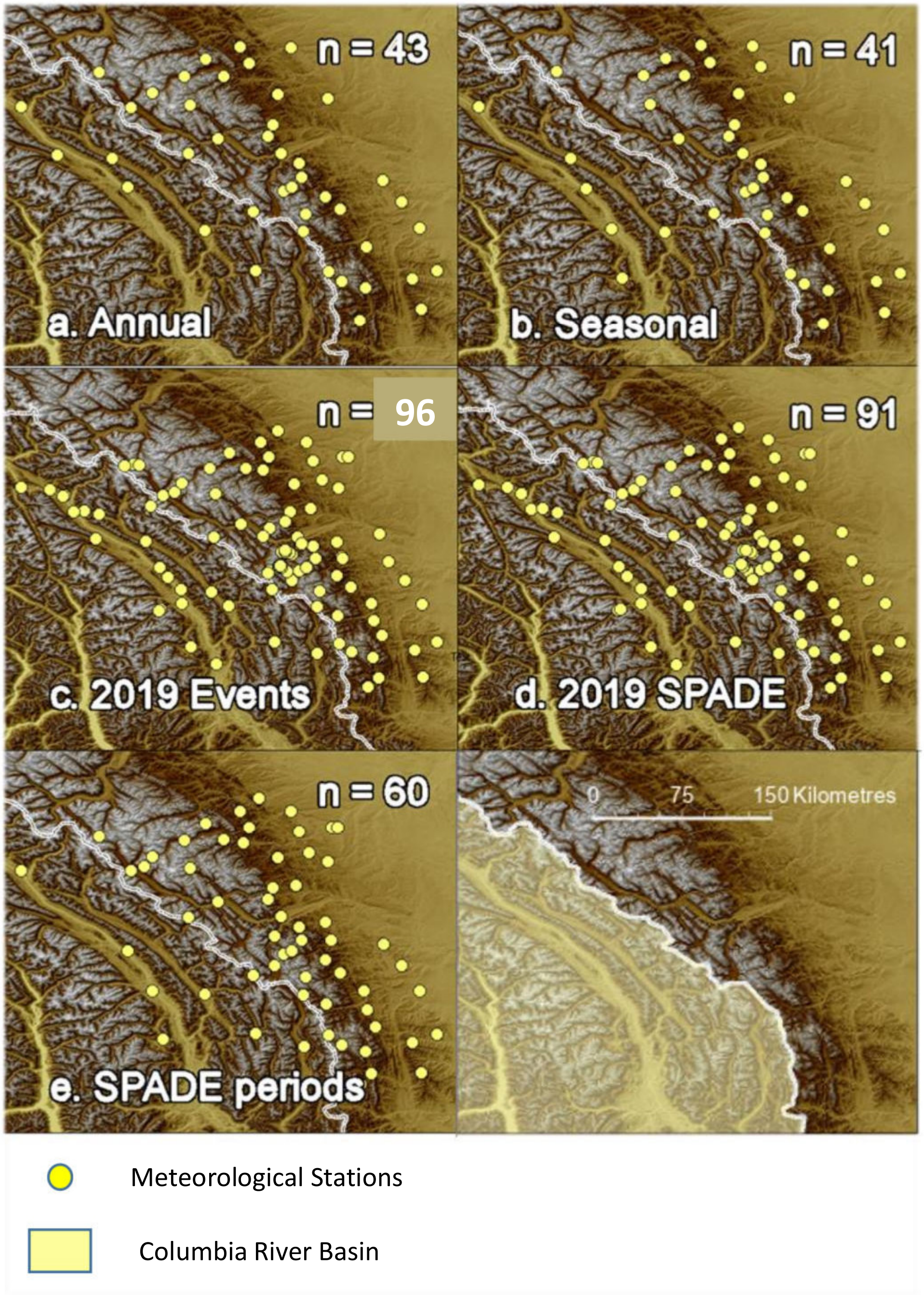

Figure 3.3. Distribution of meteorological stations for different time periods. The Columbia River Basin encompasses the western side of the Continental Divide in the study area. (a) The Annual time periods comprising of annual cumulative precipitation from 1 January to 31 December from 2011 to 2019. (b) The Seasonal time periods include measurements from four seasons including Winter, Spring, Summer, and Fall. (c) The 2019 Events period represents the 13 main precipitation events within the 2019 SPADE period (26 April to 26 June 2019). (d) The 2019 period includes every day within the 2019 SPADE period (26 April to 26 June 2019). (e) SPADE periods include every 26 April to 26 June period from 2011 to 2019.

3.5 Selecting Meteorological Stations from other Precipitation Gauge Networks

Stations were selected according to their accuracy. Stations that consistently displayed values that were incongruent with surrounding stations, were missing large parts of their time-series, or displayed constant evaporative loss, were not used in this study. MOTI stations were excluded from many aspects of this study on these grounds and were only used for the duration of the SPADE study (a two-month period). If station data contained anomalous peaks that were outside of the domain of a large precipitation event, or if data contained long breaks in precipitation that were not corroborated by other stations, this station was removed from analysis for the duration of the entire time-frame in which it appeared. If this anomaly appeared to affect cumulative precipitation amount for a given time period (as compared to other stations), then these data were removed from analysis for the entire period. More CCRN stations may have been included in longer-term analyses if there was more time to perform quality control on them during this study.

Employing this quality control process across various time-frames meant that each time-frame in which precipitation was measured used a different number of stations (Table 3.2 and Figure 3.3). The shortest and most recent time-frame used the most meteorological stations, a period of time that encompassed the 2019 SPADE events exclusively. The whole SPADE period had a similar resolution. The annual periods, which were the largest time-frames, used the smallest number of stations. Therefore, precipitation comparisons only occur between specific time-frames.

These quality control processes are employed for other meteorological variables as well. Therefore, the spatial resolution varied for each meteorological variable that was examined.

3.6 Meteorological Instrumentation at SPADE Sites

Precipitation totals for the SPADE project were acquired through the use of an OTT Pluvio (an automated weighing gauge), a Geonor T-200B (an automated weighing gauge), SR50 snow depth sensors, and tipping bucket rain gauges. Additional information regarding precipitation size and intensity was provided by OTT Parsivel (a laser-optical disdrometer). Manual snow measurements also occurred at the Fortress Mountain site using a snow ruler and a snow board. Manual snow measurements were not utilized on the west side of the Continental Divide since there was no snow accumulation at Nipika. Precipitation totals from the TBRG transect were collected using three Davis Tipping Bucket Rain Collectors (Model 7852), which were fitted with Odyssey data loggers.

All three of the main SPADE stations were equipped with a variety of meteorological instruments. However, the SPADE TBRG transect only measured precipitation amounts. My component of the SPADE experiment did not utilize all meteorological instruments located at the main SPADE sites. This study utilized meteorological instruments for measuring wind, precipitation, and temperature (Table 3.3) at various measurement intervals (Table 3.4). My component of the SPADE study focused on wind data (provided by a RM Young anemometer) and precipitation data (provided by a Geonor T-200B) at Nipika. Relative humidity values from an HS2C3 temperature-humidity probe were included in this study and timelapse images from a Wingscapes TimelapseCam (taken at one minute intervals) at about 1 m above the ground near the Nipika meteorological station were also used to determine sky conditions at this site.

Table 3.3. Meteorological instrumentation used to measure precipitation, temperature, and wind at each main SPADE site and in the tipping bucket rain gauge (TBRG) transect. (Refer to Appendix B for technical information regarding these instruments).

Meteorological Variables	SPADE sites			Instrument type
	Nipika	**Fortress Junction**	**Fortress Mountain**	**Tipping Bucket Rain Gauge (TBRG) Transect**
Precipitation	**Geonor T-200B Single Alter shield**	Pluvio 2 Single Alter shield	Pluvio 2 Single Alter shield [c] Snow board, snow depth ruler, SWE cylinder	3 Davis Tipping Buckets (Model 7852) each fitted with an Odyssey data logger
Temperature	**Campbell Scientific HS2-C3-L**	Vaisala HMP155	Vaisala HMP155	None
Wind Speed and Direction	**Campbell Scientific RM Young 5103AP-10-L**	Vaisala WXT520	Vaisala WXT520	None

Table 3.4. Time intervals at which each meteorological variable was measured at each SPADE site.

Meteorological Variables	SPADE site measurement intervals			
	Nipika (minutes)	Fortress Junction (minutes)	Fortress Mountain	Tipping Bucket Rain Gauge transect (TBRG)
Precipitation	5	1	15 minutes	At 0.2 mm of precipitation
Temperature	5	1	1 minute	None
Wind Speed and Direction	5	1	10 seconds	None

3.7 Gridded Data

The fifth major global reanalysis from the European Centre for Medium-Range Weather Forecasts (ECMWF) reanalysis (ERA5 and ERA5-Land) is a new gridded data product that provides data for 2019. ERA5 is the fifth generation of ECMWF global climate reanalysis of the atmosphere. ERA5-Land is a replay of ERA5 climate reanalysis which examines land variables at a higher resolution. Daily Surface Weather and Climatological Summaries (DayMet) are weather data that have been interpolated and extrapolated from ground observations through statistical modelling (Thornton et al. 2014). Unfortunately, DayMet does not contain any wind variables, therefore this product would have to be used in conjunction with another product that includes wind data for precipitation gradient analysis. Another meteorological gridded dataset, PNWNAmet (Werner et al. 2019), extends over a longer period but does not have any data beyond 2012. Therefore, the ECMWF reanalysis products were used for this study.

3.8 Procedures for Identifying Storms in the SPADE Domain

Once a forecast was agreed upon, SPADE personnel were deployed to Nipika and Fortress Mountain (Fortress Junction remained unmanned for the duration of SPADE) at the time that precipitation was estimated to start and for the duration of the precipitation event. Personnel left these sites only once precipitation had ceased at both sites. As the season progressed and solid precipitation became unlikely, Nipika did not have personnel outside of daylight hours, since darkness prevented sky observations, and precipitation identification was unnecessary since it was almost entirely liquid at this point in the season (as verified by the Parsivel). However, observers were deployed to Nipika during the night on 21 June 2019 to observe the exceptional intensity of this storm.

3.9 Procedures for Identifying Precipitation Events in the SPADE Domain

Precipitation events were initially identified according to precipitation at the Fortress Mountain precipitation gauge. Cumulative precipitation had to be greater than 0.2 mm per recording at Fortress Mountain for a storm to be considered a precipitation event. Precipitation at the Fortress Mountain Pluvio was used to develop the initial start and end times of the events. These times were subsequently adjusted to reflect differences in precipitation times at Fortress Junction and Nipika. All precipitation events in which observers were not present for any portion of the time with precipitation were removed from the pool. Synoptic maps were examined to determine if different precipitation events were part of the same storm system, and should be combined. Precipitation event times were then adjusted further according to field observations.

3.10 Process for Identifying Seasons

Unconventional seasons were used for this project. These seasons were adopted from *Glacier distributions and climate in the Canadian Rockies* by Shea et al. (2004). These researchers derived their seasons using climatological studies that included 30 years of meteorological data from 61 Environment Canada stations between 1961 and 1990 in this region. These seasons were constructed according to precipitation normals and monthly mean temperature. Months with similar temperature and precipitation regimes were grouped together to create four seasons of unequal lengths. According to this process winter comprises four months: November, December, January, and February. Spring comprises three months: March, April, and May. Summer comprises three months: June, July, and August. Fall comprises two months: September and October. Basing my seasons on climate normals that are over 30 years old in a non-stationary climate means that my seasons may not accurately reflect current trends. Time constraints in my project did not allow me to produce my own rigorously tested climate normals that reflect current trends, and these seasons exist in peer-reviewed scientific literature on the Canadian Rockies (Shea et al. 2004; Shea & Marshall 2007).

In the cases where I am examining seasons across an annual period, I have divided the winter season into two sections so that patterns in January and February (Winter 1) are separated from patterns in November and December (Winter 2). These patterns may be unrelated given the long time interval between them.

3.11 Data Processing for Quality Control

Precipitation data were downloaded from their respective network data repositories using the internet. Data from each station were subsequently plotted as a time-series using the R software environment for statistical analysis to determine if any parts of these data were missing or anomalous. If a section was missing or anomalous, this station was excluded from the study for the duration of the anomaly and for the duration of the period that was being examined if this potential error impacted cumulative precipitation amounts. Data were adjusted if it could be inferred that errors were a result of precipitation gauge or data logger malfunction, or errors induced by the environment. CCRN data, for example, had spikes where the weighing precipitation gauge would register zero or a value much higher than a possible increase in precipitation during a single time-frame, before returning to values that were similar to precipitation values in previous time-frames. Similar anomalies had occurred at the Nipika Geonor during the SPADE campaign, therefore it could be inferred that these anomalies were due to equipment error, so these errors were filtered out of the final cumulative precipitation values using R programming.

Filters were developed using similar programming to reduce the magnitude of evaporative loss and constant oscillation in MOTI data. However, given the dynamic nature of data from these stations, error magnitude could not be ascertained; therefore, most data from MOTI stations were discarded altogether.

The five minute Geonor data from Nipika during the SPADE study contained unexplained oscillations, many of which occurred at a diurnal frequency. These data were filtered by an experienced research group at the National Center for Atmospheric Research (NCAR) to eliminate these oscillations so that precipitation events could be more accurately identified.

A very slight temporal shift in precipitation occurred after this filtering process had been implemented, which did not seem to impact any precipitation events or analyses except the Event 10 time-series plot (Event 10 was the shortest event and lasted about 30 minutes). This slight temporal shift is impossible to quantify exactly, but the precipitation curve had a slightly different shape when it was examined at a time-frame of less than five minutes. There were no perceptible changes in the curve when it is examined at 15 minute periods. Original five minute Geonor data were used when these data were plotted against time for Event 10 to eliminate this change in curvature. Time-series at Fortress Mountain and Fortress Junction were also corrected using R programming for missing time-stamps or unexplained spikes in values.

TBRG data were plotted across time to determine if there were visible errors in their data. No errors could be identified outside of periods where TBRGs were known to be out of operation. There were three instances where TBRGs were known to be out of commission. The pedestal for Precipitation Gauge 1 was broken in two instances and Precipitation Gauge 3 was filled with pine needles in one instance. These time periods were highlighted and noted in the original precipitation gauge data spreadsheet. Precipitation Gauge 1 was broken during periods in which there may have not been large amounts of precipitation; therefore, these data were retained in subsequent plots and analyses (with this potential source of error noted). However, it was determined that when Precipitation Gauge 3 was broken, there were large amounts of precipitation; therefore, this period of time was removed from plots or analyses. Refer to Appendix C for additional information regarding quality control of data from the SPADE TBRG transect.

3.12 Data Processing for Precipitation Gradients

Once these time-series had undergone quality control, each station time-series was subsetted. Cumulative precipitation was extracted for the specified time-frame for each station and then entered into a spreadsheet document that attached the station name, the latitude and the longitude to each cumulative precipitation value. This spreadsheet was subsequently processed using the ArcMap component of ArcGIS Desktop 10.8. Once cumulative precipitation values were attached to x and y values on a map, ArcMap Natural Neighbour interpolation was used to develop spatial maps of precipitation patterns. This interpolation technique was selected since it retained the original station values during interpolations and did not produce assumptions about precipitation gradients beyond the SPADE domain. Additionally, this type of interpolation technique could produce precipitation gradients with abrupt and/or irregular changes across space, which could be characteristic of precipitation gradients in the mountains.

Hourly data from other networks were most commonly used to evaluate precipitation gradients during the SPADE period. However, none of the precipitation events occurred precisely over hourly intervals, therefore, hourly intervals that were roughly equivalent to these event periods were chosen for precipitation data subsets.

3.13 Data Processing for Time-Series Line Plots with Wind Vectors

Filtered precipitation data from the three main SPADE sites were plotted as lines across time using R programming. Alongside these lines, precipitation data from TBRGs were plotted as bar plots to demonstrate relative intensity. During analyses of TBRG data, it was determined that precipitation could be related to Events 10 and 11 (Table 5.2) may have occurred at these sites outside of existing precipitation event time-frames. Therefore, time-series precipitation plots were adjusted to encompass adjacent precipitation from TBRGs.

These adjusted time-frames were labelled Event 10a and Event 11a. Wind vector data were plotted at as fine a resolution that could be visualized without overlapping arrows. In the case of smaller events, this was at five minute intervals, for larger events this was at 15 minute intervals. Wind vectors with speeds less than 0.5 m s^{-1} were eliminated from these plots and replaced with zero values since it could not be determined if the anemometer was functioning correctly at these low wind speeds. A similar set of graphs was produced to examine precipitation intensity using bar plots. Filtered precipitation data from the three main SPADE sites were all divided up into 15-minute increments so that each time-series was at an equal interval, then the cumulative precipitation was taken for each 15-minute interval. These data were plotted next to each other as bar plots using R programming to demonstrate precipitation intensity.

3.14 Data Processing to Identify Convection

To identify seasons or periods of time during the year in which convection was prevalent, precipitation was plotted across time intervals to establish times at which most precipitation occurred using a binning technique developed using R programming. Periods of time with convection would be identified as time periods with a bias towards afternoon precipitation.

3.15 Additional Tools Used for Analyses

3.15.1 Software Tools

Wind roses and wind vectors were created using the OpenAir package in R. This R package is capable of averaging wind vectors across time using circular statistics.

Wind speeds of 0.5 m s^{-1} and less have been stripped out of wind vectors and wind roses that accompany event analysis. It has not been determined if the anemometer was functioning correctly at speeds below 0.5 m s^{-1}, which is the lowest speed at which these anemometers have been determined to accurately measure wind speed.

3.15.2 Weather Resources

Satellite images and ECCC maps were obtained from public domains during the SPADE period. This information was obtained from http://www.goes.noaa.gov and https://weather.gc.ca/analysis/.

3.15.3 Statistics

Mean is the centre of a group of values. Means were obtained using R programming functions (Equation 1).

$$\bar{x} = \frac{\sum_{i=1}^{N} x_i}{N} \tag{1}$$

Covariance (*cov*) is used to examine how two variables vary in conjunction with each other (Equation 2).

$$cov\ x, y = \frac{\sum (x_i - \bar{x})(y_i - \bar{y})}{N-1} \tag{2}$$

Correlation coefficient (*r*) is a measure for the strength of relatedness between two variables (Equation 3). Correlations were obtained using R programming functions.

$$r = \frac{\sum (x_i - \bar{x})(y_i - \bar{y})}{\sqrt{\sum (x_i - \bar{x})^2 \sum (y_i - \bar{y})^2}} \tag{3}$$

A correlation (*r*) is a measure of the relationship between two variables. This study examines correlation using the Pearson correlation coefficient which describes the robustness of the linear relationship between these variables. The coefficient of determination is determined when the correlation (*r*) is squared (R^2). It is a measure of explained variance. It is the proportion of variance in the dependent variable that was determined by the independent variable. The statistical significance of this test is denoted as a *p* value, or a probability value. For the purposes of this study the threshold for statistical significance is 0.05. When a test statistic value is below $p = 0.05$ using a one-tailed t-test, the correlation coefficient is significantly greater or lesser than zero.

Locally Estimated Scatterplot Smoothing (LOESS) is a moving regression that provides a non-parametric analysis of scatter plots (Fox & Weisberg 2018). In this case, LOESS regressions were obtained using the ‘symmetric’ version, where outliers are detected and then down weighted. LOESS was used to examine relationships between precipitation and environmental conditions such as elevation, longitude, and latitude.

3.16 Geographical Context of Meteorological Stations in the SPADE Study Area

Meteorological stations were somewhat evenly distributed throughout the study area (Figure 3.4), but one meteorological network on the western side of the Continental Divide (MOTI) was largely unsuitable for this study, with the exception of eight stations over the two-month period that encompasses SPADE. Therefore, there was a bias towards eastern meteorological sites in this study. A histogram comparison of meteorological station elevations and digital elevation model (DEM) elevations demonstrates that stations were located at disproportionately low elevations in relation to the surrounding terrain (Figure 3.5). Sixty-six percent of stations were located below 1738 m above sea level (the mean elevation for the DEM), with the highest station frequency between 1300 to 1400 m above sea level. Although there were fewer stations above 1738 m above sea level, they were relatively evenly distributed among elevations, with the exception of the highest station (Helen Lake) that was substantially higher than all of the other stations. An analysis of the DEM reveals mountainous topography in this region with an elevation range that nearly encompasses 3000 m (Figure 3.6). The limited number of stations at lower elevations in this range of elevations could mean that this study is not able to wholly quantify precipitation in the Canadian Rockies.

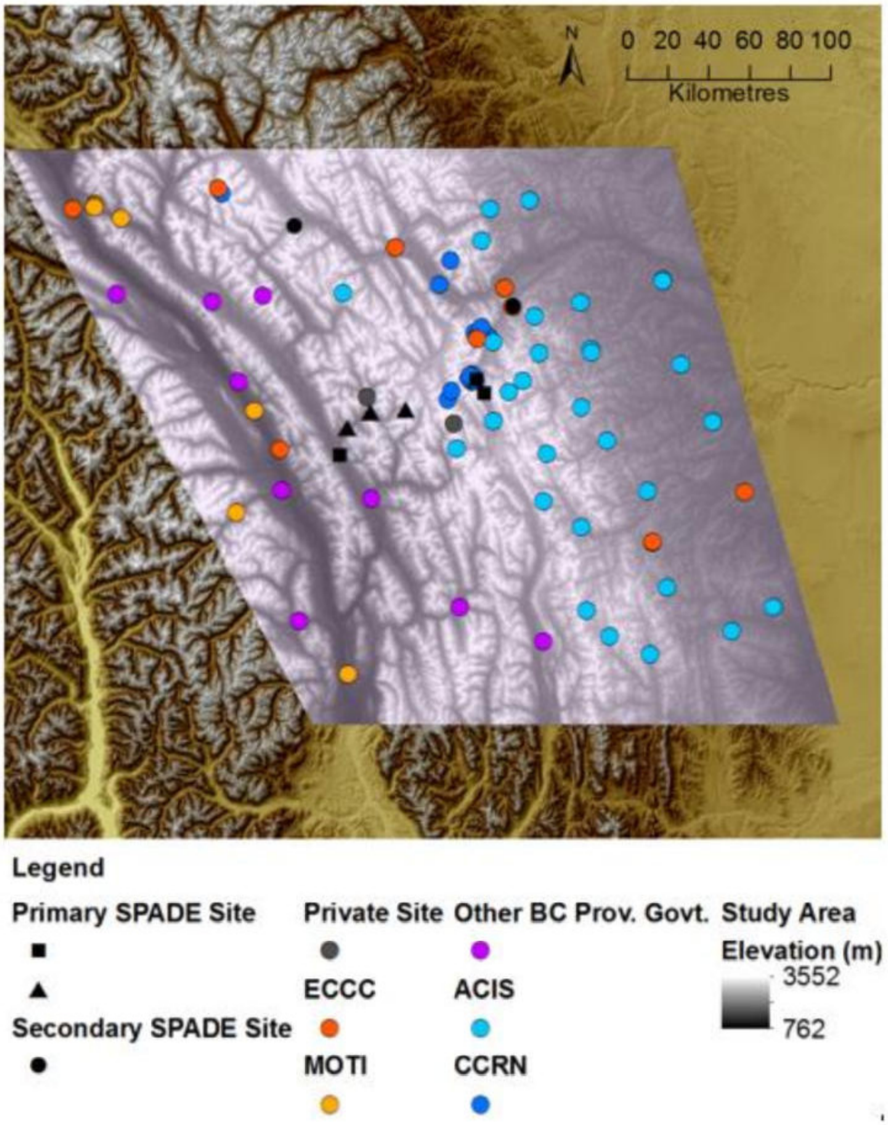

Figure 3.4. Meteorological networks that were considered in the SPADE study area. Meteorological networks included our SPADE network, two private sites, ECCC (Environment and Climate Change Canada), BC MOTI (Ministry of Transportation and Infrastructure), BC provincial government networks such as FLNRORD and BC Hydro stations, ACIS (Alberta Climate Information Service which is administered by the Province of Alberta), and CCRN (Changing Cold Regions Network), which is a collaborative scientific research network. Many MOTI stations and all of the private stations were removed from this study since data from these networks were unsuitable for our study.

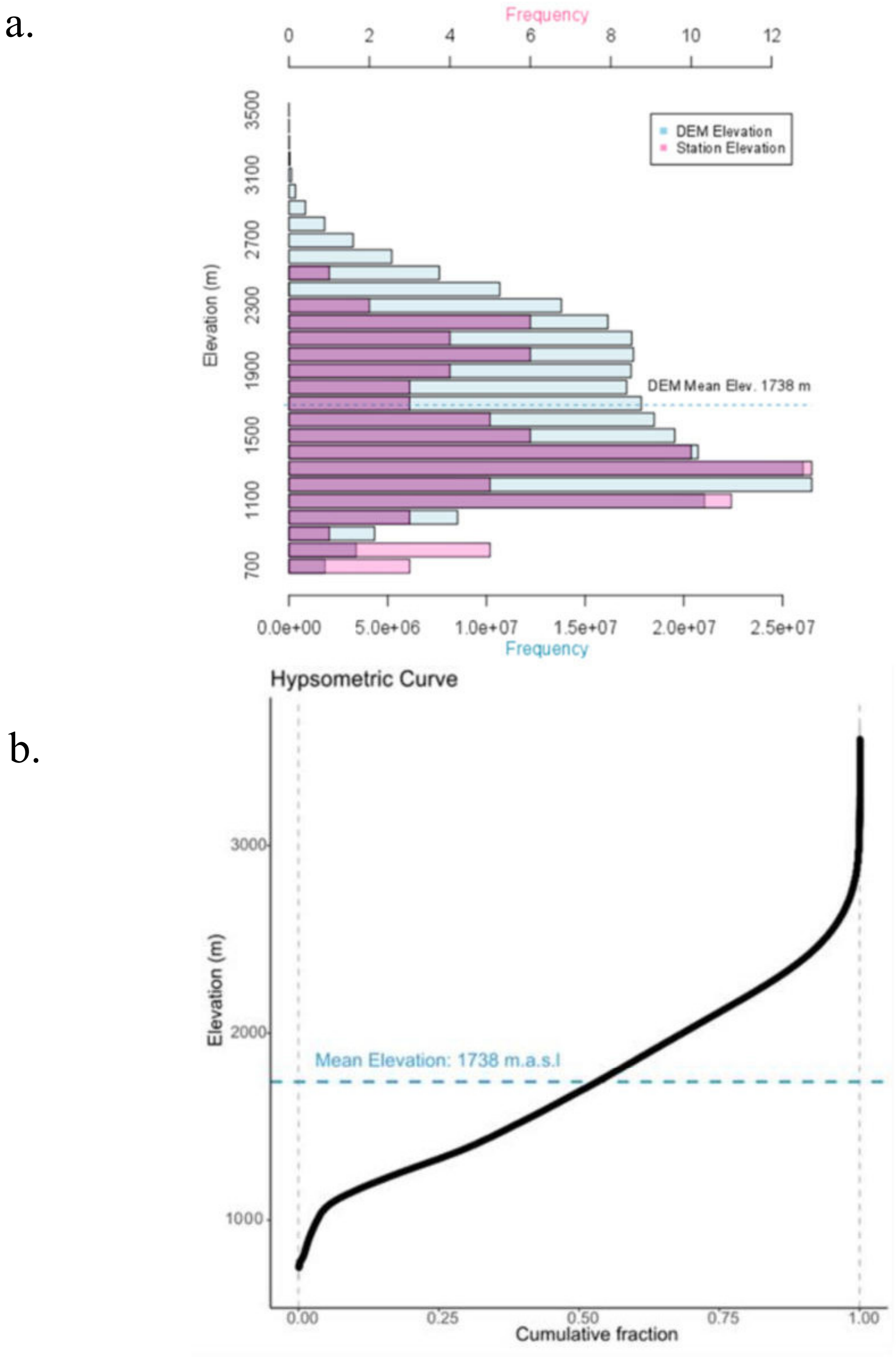

Figure 3.5. Topographical information from the study area. (a.) A histogram of elevations from a 20 m resolution Natural Resources Canada (NRCAN) digital elevation model (DEM) (blue), with meteorological station elevations at 100 m increments (pink). Purple-shaded areas demonstrate areas of elevation pattern overlap. (b.) A hypsometric curve derived from the study area DEM. This curve denotes the proportion of the landscape that belongs to each elevation.

Measurement	Value
Minimum Elevation	750 m.a.s.l.
Median Elevation	1690 m.a.s.l.
Maximum Elevation	3571 m.a.s.l.
Maximum Area	118947 km^2

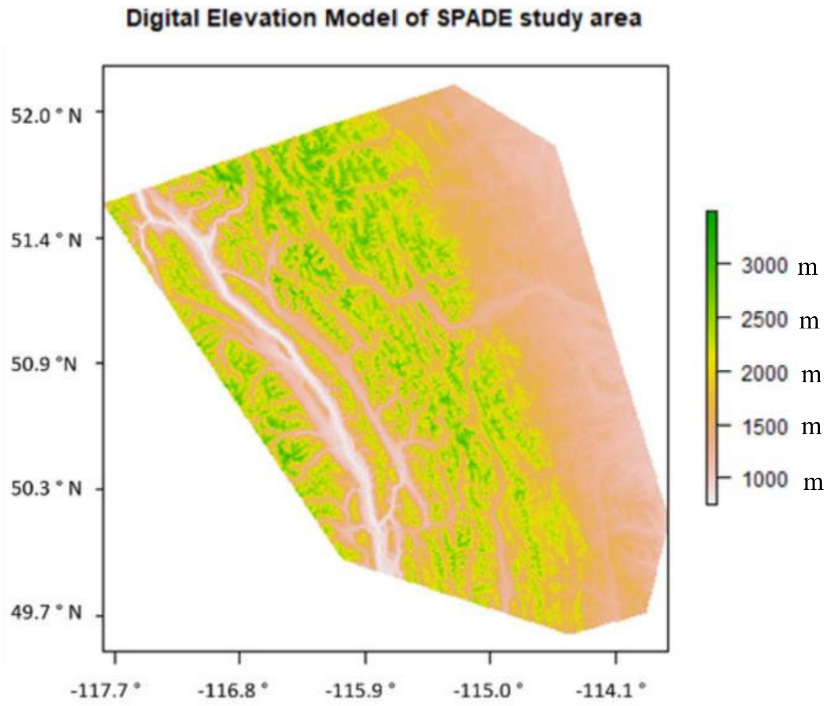

Figure 3.6. Topographical information and a raster derived from a Natural Resources Canada digital elevation model (DEM) with a 20 m resolution.

Chapter 4: Results

This chapter presents the results of various analyses. These analyses contain an examination of cumulative precipitation values in ERA5-Land data and station data, precipitation events during the SPADE period, wind-precipitation interactions at Nipika Mountain Resort (Nipika), a regional analysis of precipitation events using station data, and an examination of factors that may have influenced precipitation amounts across the study area during the SPADE period (including elevation, latitude, longitude, temperature and wind characteristics). These results also incorporate a comparison of precipitation during the SPADE period across years, in addition to examining precipitation across entire years and across seasons. I have also included an examination of diurnal precipitation patterns and a preliminary examination of wind-precipitation interactions for the study area.

My results examined graphical analysis of station data from primary observation sites using tools provided by R to produce visual comparisons, interpolations of regional precipitation using the Natural Neighbour interpolation tool from ArcMap 10.8 to examine precipitation patterns, and LOESS regression to examine relationships between precipitation and factors such as elevation, latitude, and longitude.

4.1 Comparison of annual cumulative precipitation from ERA5-Land and station data

ERA5-Land total precipitation values compared favourably with station values. Cumulative annual precipitation amounts from ERA5-Land were only 13 mm greater than station values for 2012 (Figure 4.1). The relationship between ERA5-Land values and station values appeared to be stronger during the 2011-2014 period than it was during the 2015-2019 period. Overall ERA5-Land overestimated total precipitation amounts in the SPADE study area by 6%. It was determined that during the year in which SPADE occurred, 2019 cumulative precipitation values were 4% larger than the average of 677 mm, meanwhile the 2019 ERA5 cumulative precipitation value was 6.5% larger than the station values.

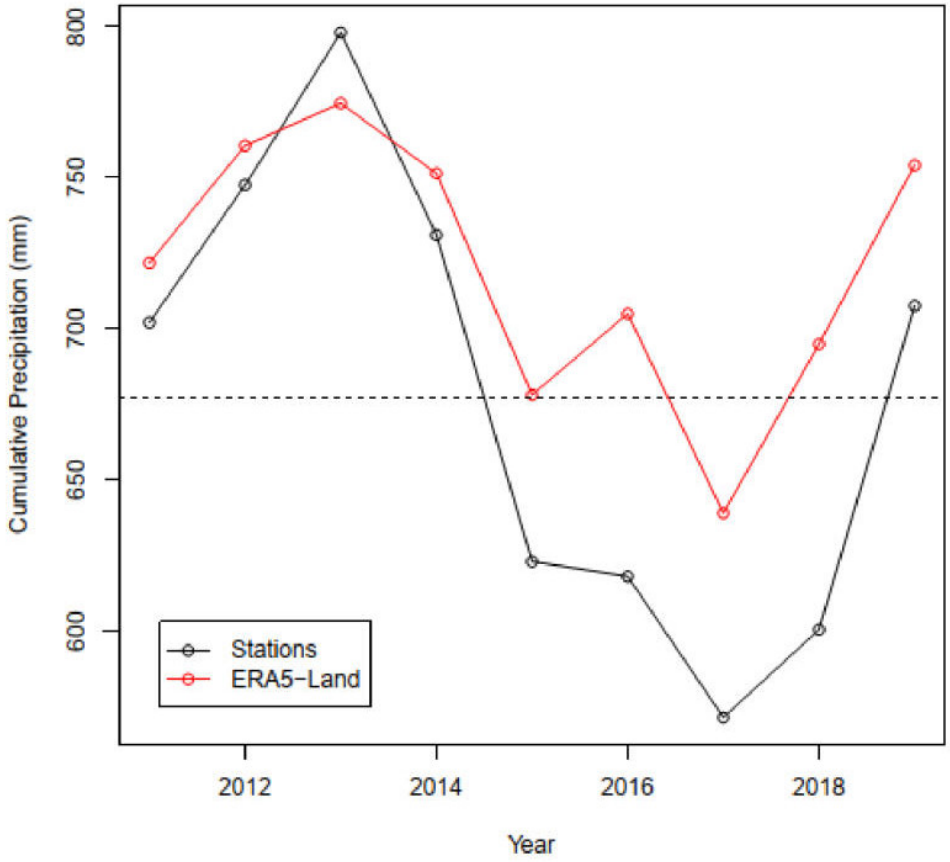

Figure 4.1. Average annual cumulative precipitation for the SPADE study area plotted across years (2011 to 2019). The dotted line represents the average precipitation amount for this time period (677 mm). (Precipitation patterns for the eastern side of the Continental Divide are overrepresented in this plot because the eastern side of the Continental Divide received substantially more precipitation than the western side of the Continental Divide during this period). The red line represents average ERA5-Land values at the stations that were used to derive the annual precipitation amounts. The RMSE for this reanalysis-station comparison is 55.5 mm. The bias for the precipitation-ERA5 relationship is -42.3 mm. There is a statistically significant correlation of 0.94 between these two types of data with $p < 0.001$.

4.2 Comparison of annual and SPADE cumulative precipitation

A line graph depicting cumulative precipitation from the SPADE period exhibited a similar profile to a line graph depicting annual precipitation across years. Cumulative precipitation and SPADE precipitation from these time periods exhibited a strong relationship, with a correlation value of 0.93 and $p < 0.001$ (Figure 4.2).

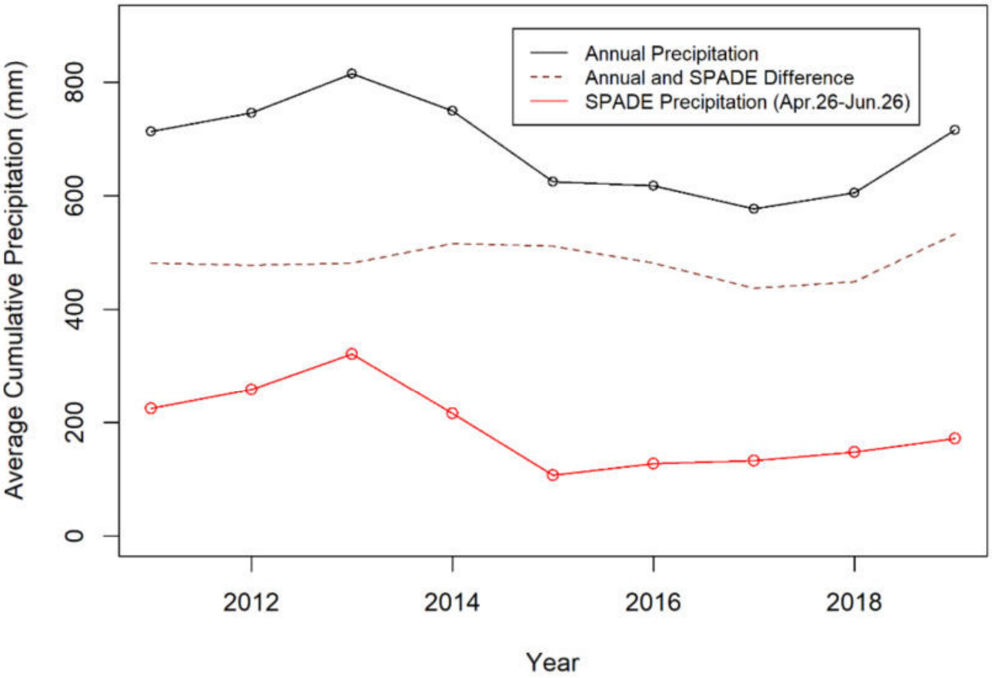

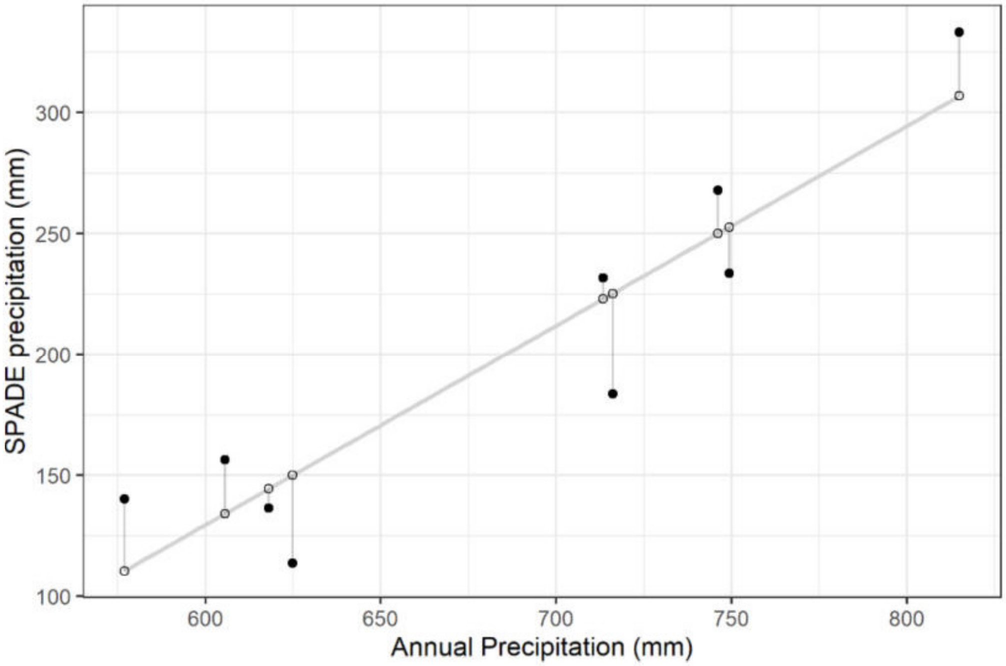

Figure 4.2. (Top) A line graph of average annual precipitation and average precipitation during the SPADE period with the difference in between the annual period and the SPADE period plotted across years. (Bottom) This plot compares the residuals obtained from a linear regression between the two periods to determine if the SPADE study period could be used as a proxy for annual cumulative precipitation. The linear regression had a correlation of 0.93, $p < 0.001$.

Both the line plots for annual cumulative precipitation and for SPADE cumulative precipitation exhibited peak values at 2013. The lowest cumulative value for the SPADE period was 2015, while the lowest value for the annual period was 2017. In 2019, the year of our experiment, the SPADE period comprised of a smaller proportion of the annual precipitation in comparison to the average. The 2019 SPADE period comprised of 25% of the total precipitation from that year. SPADE periods comprised 28% of the annual precipitation on average during the 2011 to 2019 period.

4.3 Examining predictors for precipitation during annual and SPADE periods

Table 4.1. Multiple linear regression results for cumulative precipitation during the 2019 SPADE period and elevation, longitude, and latitude.

Period	Main predictor	Elevation Slope mm/m	Below *p*-value	Longitude Slope	Below *p*-value	Latitude Slope	Below *p*-value	n	R^2
SPADE 2019	Longitude	9.03×10^{-2}	0.001	5.33×10^{1}	0.001	1.52×10^{1}	Not Sig.	91	0.60

Linear regressions were performed on cumulative precipitation amounts from the stations in our study area over each time frame to determine which variables had the greatest predictive power for cumulative precipitation. In addition to slope calculations, the probability that the slope was greater than zero was also determined using the F-test of overall significance. When a multiple linear regression was performed on 91 stations during the 2019 SPADE period, longitude emerged as the most important predictor of precipitation amounts (Table 4.1). However, when a smaller subset of stations was used (n=60) in multiple linear regressions for the same period of time (May-June) from the years 2011 to 2019, longitude was not the best predictor of precipitation in 2019, but rather elevation was (Table 4.2).

Table 4.2. Multiple linear regression results for cumulative precipitation during the SPADE period across years (2011 to 2019) and elevation, longitude, and latitude. Coloured blocks denote insignificant relationships. *P*-values are derived from an F-test and represent the probability that the null hypothesis is true. The test statistic for each regression is below the *p*-value threshold listed in the table.

SPADE Period	Main predictor	Elevation Slope mm/m	*p*-value	Longitude Slope	*p*-value	Latitude Slope	*p*-value	n	R^2
2011	Longitude	5.44×10^{-2}	0.05	8.44×10^{1}	0.001	7.74×10^{1}	0.001	60	0.51
2012	Longitude	6.55×10^{-2}	0.001	4.86×10^{1}	0.001	2.51×10^{1}	0.05	60	0.36
2013	Longitude	1.47×10^{-1}	0.001	9.30×10^{1}	0.001			60	0.44
2014	Longitude	5.10×10^{-2}	0.05	5.97×10^{1}	0.001			60	0.33
2015	Elevation	3.59×10^{-2}	0.001	1.78×10^{1}	0.01			60	0.33
2016	Elevation	5.20×10^{-2}	0.001			-1.51×10^{1}	0.05	60	0.37
2017	Elevation	7.04×10^{-2}	0.001	2.48×10^{1}	0.01	2.01×10^{1}	0.05	60	0.45
2018	Elevation	5.64×10^{-2}	0.001	2.01×10^{1}	0.05	2.03×10^{1}	0.05	60	0.28
2019	Elevation	6.86×10^{-2}	0.01	3.99×10^{1}	0.01			60	0.22

This smaller subset was necessary since many stations were unavailable across the entire May-June time-frame. For this smaller subset of stations, elevation was the most important predictor of cumulative precipitation amounts for the years 2015 to 2019. Longitude was the best predictor for 2011 to 2014. When multiple linear regressions were performed on cumulative precipitation amounts across years, elevation emerged as the best predictor of cumulative precipitation amounts (Table 4.3). Elevation remained an important predictor of cumulative precipitation amounts when linear regressions were performed only on the factors elevation and precipitation (Table 4.4).

Table 4.3. Multiple linear regression results for cumulative precipitation during annual periods (2011 to 2019) and elevation, longitude, and latitude. Coloured blocks denote insignificant relationships. *P*-values are derived from an F-test and represent the probability that a null hypothesis is true. The test statistic for each regression is below the *p*-value threshold listed in the table.

Year	Main Predictor	Slope mm/m	*p*-value	Longitude Slope	*p*-value	Latitude Slope	*p*-value	n	R^2
2011	Elevation	4.60×10^{-1}	0.001					43	0.56
2012	Elevation	4.39×10^{-1}	0.001	-1.47×10^{2}	0.01	-1.86×10^{2}	0.01	43	0.56
2013	Elevation	4.91×10^{-1}	0.001					43	0.60
2014	Elevation	3.75×10^{-1}	0.001					43	0.35
2015	Elevation	3.35×10^{-1}	0.001	-1.21×10^{2}	0.01	-1.36×10^{2}	0.01	43	0.51
2016	Elevation	2.95×10^{-1}	0.001	-7.48×10^{1}	0.05			43	0.44
2017	Elevation	4.58×10^{-1}	0.001	-7.42×10^{1}	0.05	-1.11×10^{2}	0.05	43	0.63
2018	Elevation	3.91×10^{-1}	0.001	-8.39×10^{1}	0.05			43	0.55
2019	Elevation	4.03×10^{-1}	0.001					43	0.47
Overall Means	Elevation	4.05×10^{-1}		-1.00×10^{1}		-1.44×10^{2}		43	0.52

Table 4.4. Linear regression results for elevation and cumulative precipitation (2011 to 2019). *P*-values are derived from an F-test and represent the probability that a null hypothesis is true. The test statistic for each regression is below the *p*-value threshold listed in the table.

Years	Main Predictor	Slope mm/m	*p*-value	n	R^2
2011	Elevation	0.45	0.0010	43	0.55
2012	Elevation	0.41	0.0010	43	0.39
2013	Elevation	0.48	0.0010	43	0.48
2014	Elevation	0.36	0.0010	43	0.28
2015	Elevation	0.32	0.0010	43	0.35
2016	Elevation	0.29	0.0010	43	0.37
2017	Elevation	0.44	0.0010	43	0.57
2018	Elevation	0.38	0.0010	43	0.49
2019	Elevation	0.40	0.0010	43	0.45

4.4 Precipitation Patterns during the SPADE period (26 April 2019 to 26 June 2019)

The highest precipitation accumulation was found slightly to the east of the SPADE meteorological stations, on the eastern side of the Continental Divide during the SPADE period (Figure 4.3). Sites with largest amounts of precipitation during this period were a mixture of mid-elevation sites and high elevation sites. Mid-elevation sites with large accumulations were located slightly to the east of high elevation sites with large accumulations during this May-June period in 2019.

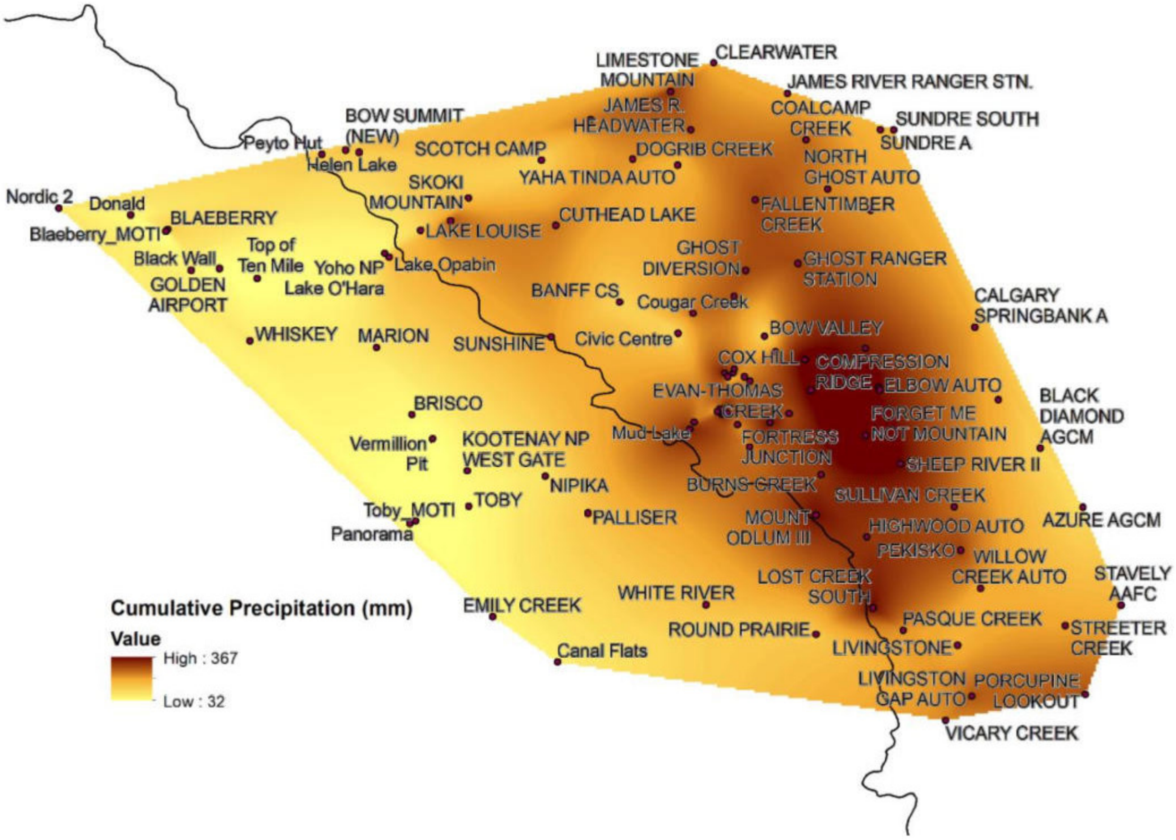

Figure 4.3. Precipitation accumulation from the 2019 SPADE period for all 91 meteorological stations in the study area. Precipitation values were derived from interpolations of station data. Black line denotes the Continental Divide. Capital and lower-case letters were used to designate stations from different networks. Networks with capital letters have continuous data. Networks with lower case letters may have superior but discontinuous data or may have problematic data.

Overall, greater amounts of precipitation occurred on the eastern side of the Continental Divide during the 2019 SPADE campaign. Precipitation events varied in magnitude and each precipitation event had its own suite of distinctly shaped precipitation patterns in the study area (Figure 4.4). Precipitation events associated with large synoptic scale events produced the most precipitation, but event type and moisture flux pattern was not identifiable from a visual inspection of precipitation accumulation (Figure 4.5). However, the precipitation events that were the result of localized topographical effects (storms created within the topography without external forcing (Events 6 and 7), resulted in several large areas of high accumulation relative to their surroundings. Precipitation events varied greatly in magnitude with Event 13 having a much greater magnitude than any other event. The four largest precipitation events that were identified as "significant long-lasting events" using SPADE sites (Events 1, 5, 9, and 13 (see Appendix D)) were also the largest events in the regional study area according to regional precipitation accumulation. Three out of four of these events were caused by upper level troughs (Event 5 was created by an upper level ridge). There was an upslope flow component to moisture flux in the Canadian Rockies for at least part of each of the four largest precipitation events.

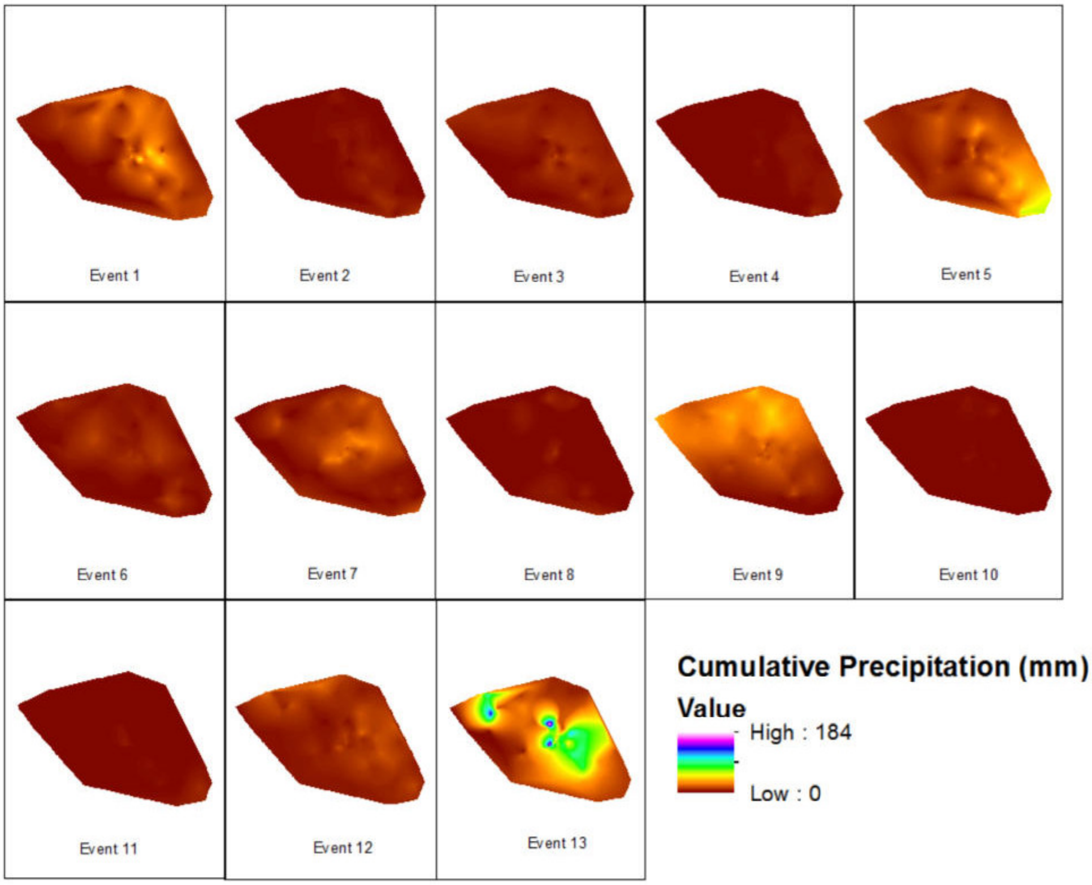

Figure 4.4. Interpolated cumulative precipitation amounts for each precipitation event during the 2019 SPADE period from meteorological station data. Total precipitation amounts for each precipitation event were interpolated to indicate the magnitude of each event relative to others.

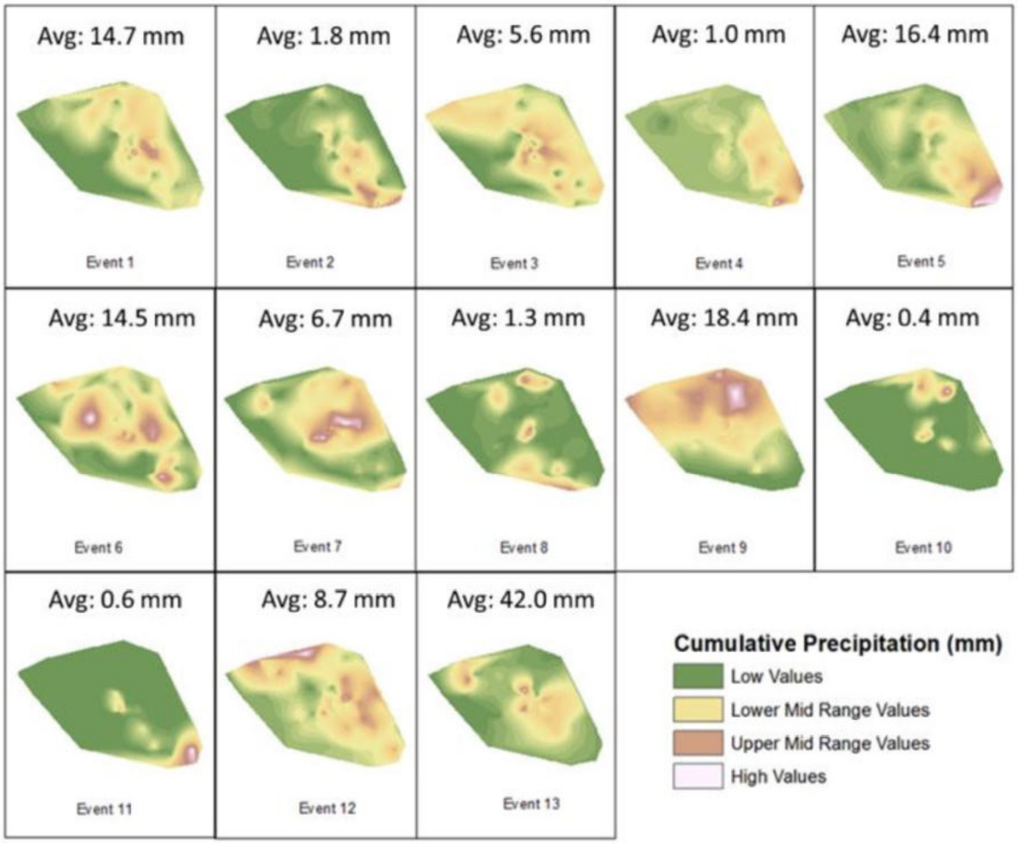

Figure 4.5. Comparison of relative amounts of precipitation across the study area during each precipitation event that occurred during the 2019 SPADE campaign.

4.5 Precipitation Patterns with Elevation

In an elevational transect of the study area, precipitation increased with elevation during the 2019 SPADE period (May-June 2019) (Figure 4.6). Sites with similar elevations received equivalent amounts of precipitation with the highest site, Fortress Mountain, receiving the most precipitation and the lowest site, Nipika obtaining the least amount of precipitation for all sites. Cumulative precipitation increased with elevation during the 2019 SPADE period; however, this relationship was likely non-linear (Figure 4.5).

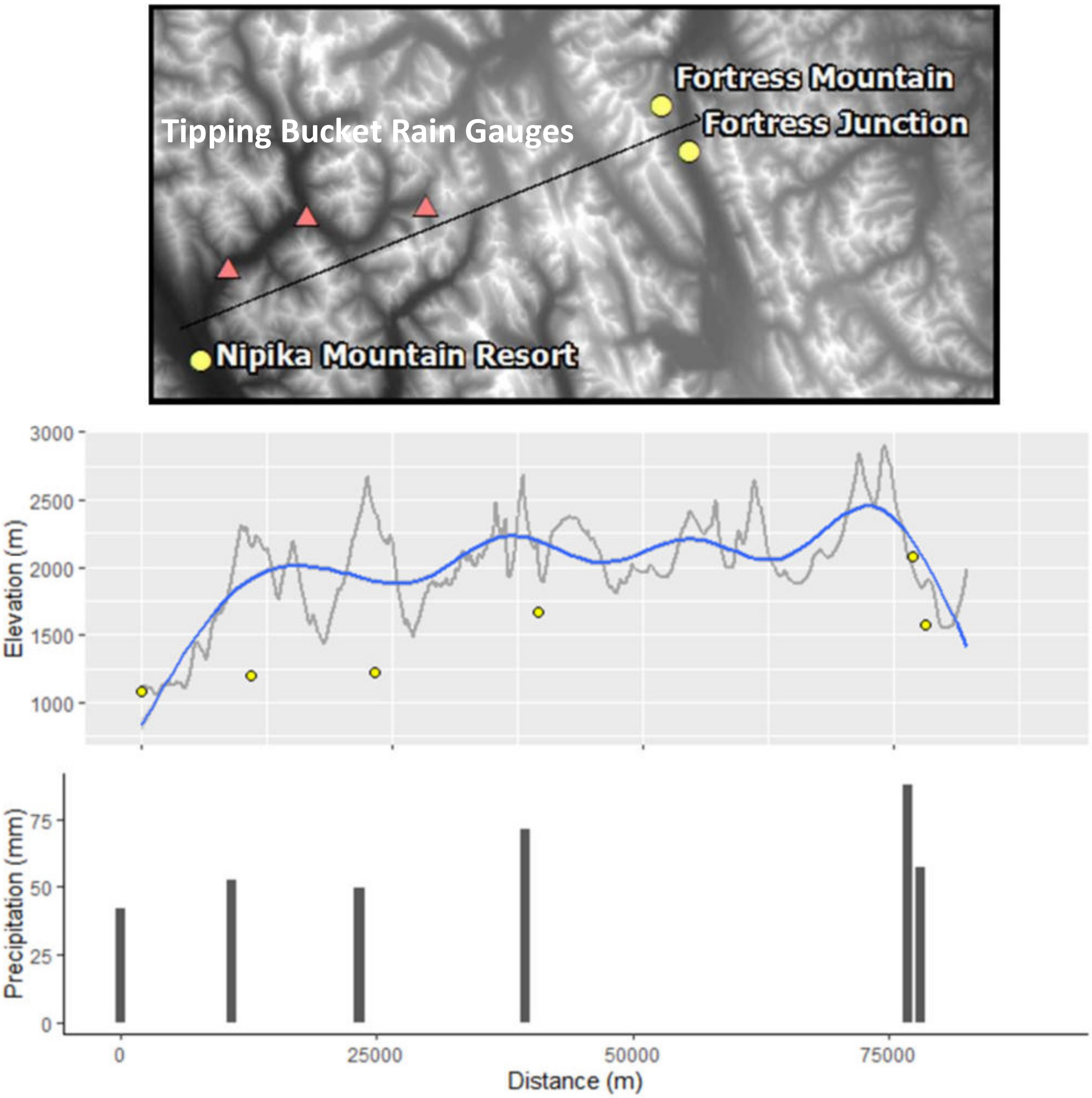

Figure 4.6. Linear elevation profile between Nipika, Fortress Mountain, and Fortress Junction (top). The blue line denotes a smoothed version of the elevation profile (middle). Circles designate station locations on the transect, these include the primary observation sites for SPADE and the precipitation transect which are tipping bucket rain gauges (red triangles). The bar graph represents total precipitation at each station between 12 May and 23 June 2019 (bottom).

a.

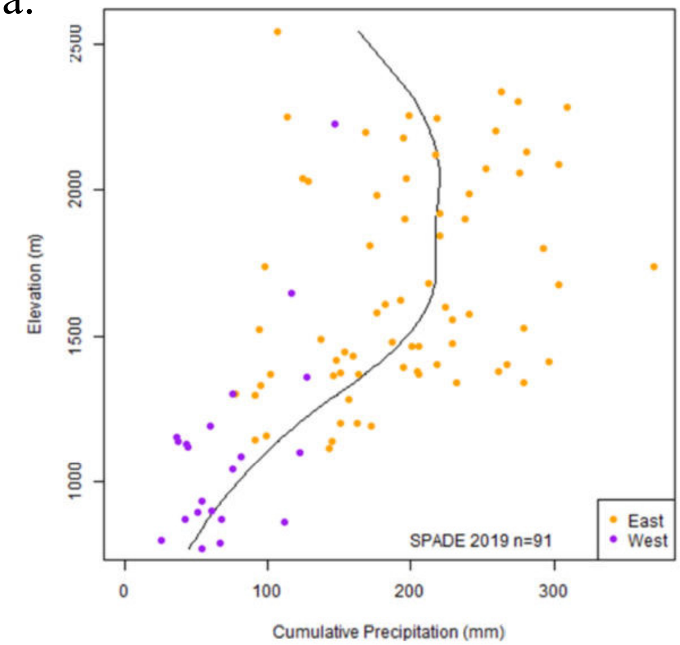

All stations are included in this plot (n=91).

b.

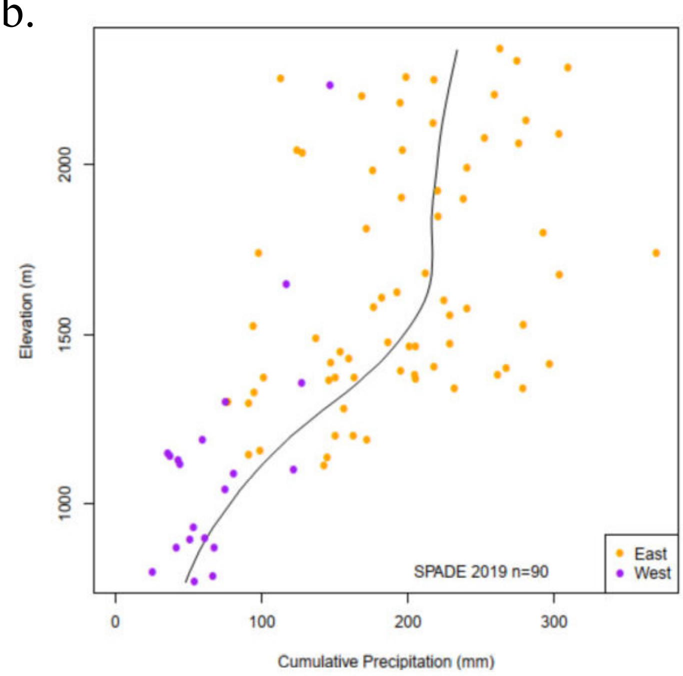

A potential high elevation outlier (Helen Lake) is removed from this plot (n=90).

Figure 4.7. Cumulative precipitation plotted against elevation at all stations in the SPADE study area. Points denote meteorological stations, with purple points denoting stations on the west side of the Continental Divide and orange points denoting stations on the east side of the Continental Divide. A multiple linear regression was used to examine the relationship between elevation, longitude, and latitude to cumulative precipitation over the SPADE period. This regression had a multiple R^2 of 0.60, $p < 0.001$. ($\hat{y} = 5.4 \times 10^3 + 9.0 \times 10^{-2}$Elevation+ 5.3×10^1 Longitude. Latitude was a non-significant predictor).

Elevation, longitude and latitude are likely the most important factors in cumulative precipitation amounts with an R^2 value of 0.60 for these three variables in a multiple linear regression from the 2019 SPADE period. Precipitation accumulated preferentially on the east side of the study area during this SPADE period according to regression curves (Figure 4.8). Peak precipitation values occurred just to the east of the apex of the regression curve for station elevations. The regression curve for precipitation does not match the regression curve for elevation with much sharper changes in slope on either side of the Continental Divide. The regression curve for cumulative precipitation has a peak just south of the apex for the regression curve for elevations. The slopes of the regression curves were closely matched to the south of this point; however, the precipitation curve had a much sharper change in slope than the elevation curve to the north of this point, with precipitation values changing at a much faster rate than elevation.

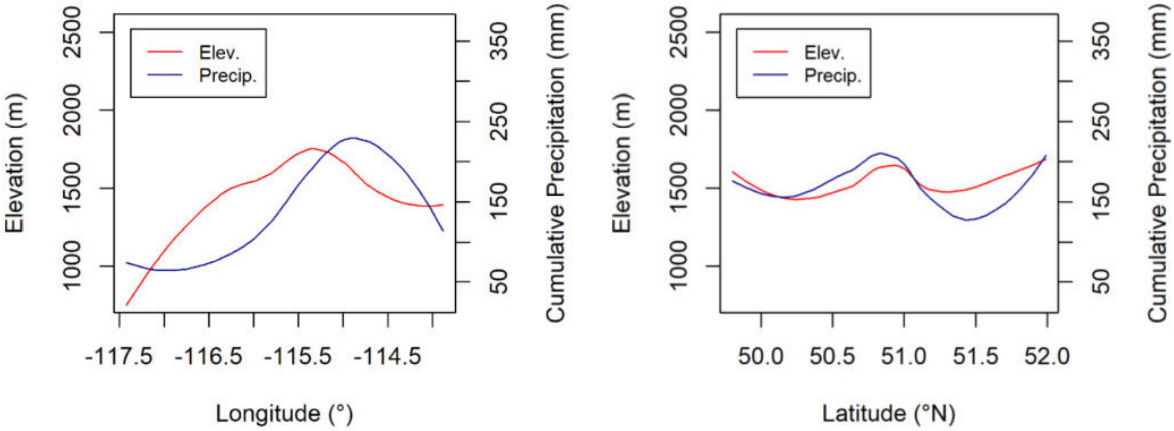

Figure 4.8. Relationships between precipitation and longitude and latitude during the SPADE period. (Left) A LOESS regression of meteorological station elevation paired with a LOESS regression of total accumulated precipitation at these stations against longitude (n = 91). (Right) A LOESS regression of meteorological station elevation against latitude paired with a LOESS regression of total accumulated precipitation against longitude (n = 91).

4.6 Examining the SPADE period across years

When LOESS regression curves of cumulative precipitation for the SPADE periods between 2011 and 2019 are plotted against longitude, the year 2013 exhibits the most conspicuous curve for peak precipitation with a high peak to the east of the height of land depicted in the regression curve for elevation (Figure 4.9. Refer to Appendix E to see relationship with Continental Divide). The curve for 2019 exhibits a similar peak at roughly the same longitude on the eastern side of the Continental Divide, but at a much lower magnitude. In contrast, precipitation from 2013 and 2019 was not remarkable on the west side of the Continental Divide in comparison to other years. The curves for 2017 had a peak slightly to the east of the height of land with low overall values, while 2016 exhibited peak values on the very western margin of the study area. Only 2015 exhibited lower precipitation values than 2016 and 2017 for the SPADE period with a shallow peak in precipitation values located far to the east of the height of land in comparison to almost all of the other years (only 2014 exhibited a more easterly precipitation peak). A similar regression curve was constructed from the relationship between longitude and the elevation/precipitation ratio (Figure 4.10), demonstrating that a relatively large proportion of precipitation relative to elevation exists on the west side of the study area where the stations are comparatively lower in elevation for most years.

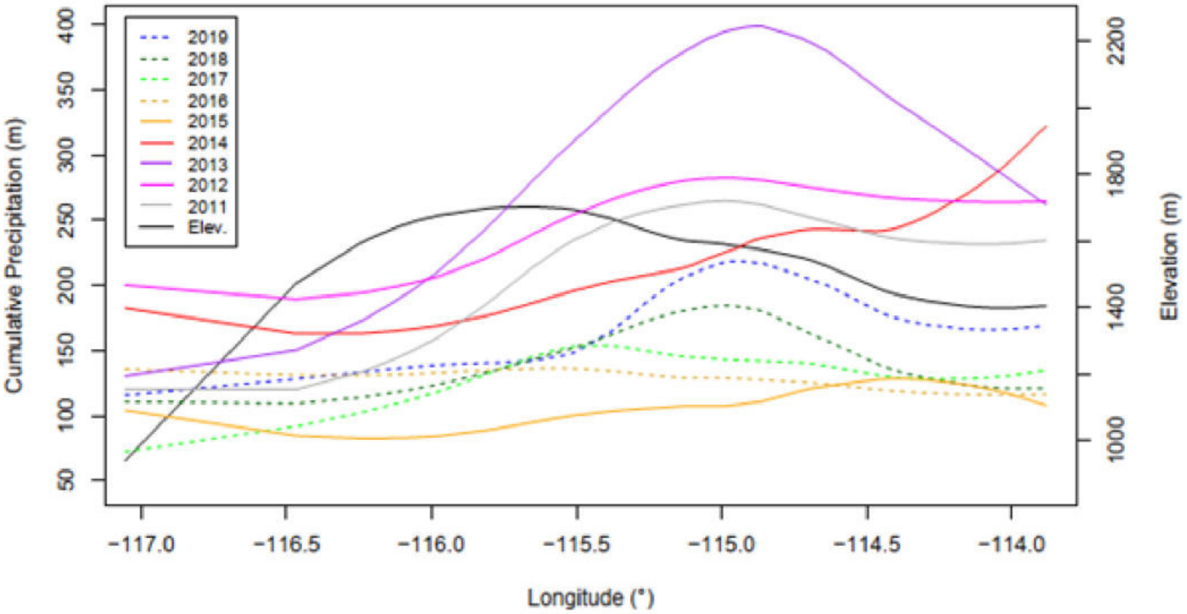

Figure 4.9. LOESS regression of cumulative precipitation during the SPADE period from each year (2011-2019) plotted across the longitudinal coordinate of each station. The black line denotes a LOESS regression of average station elevation at a specific longitude.

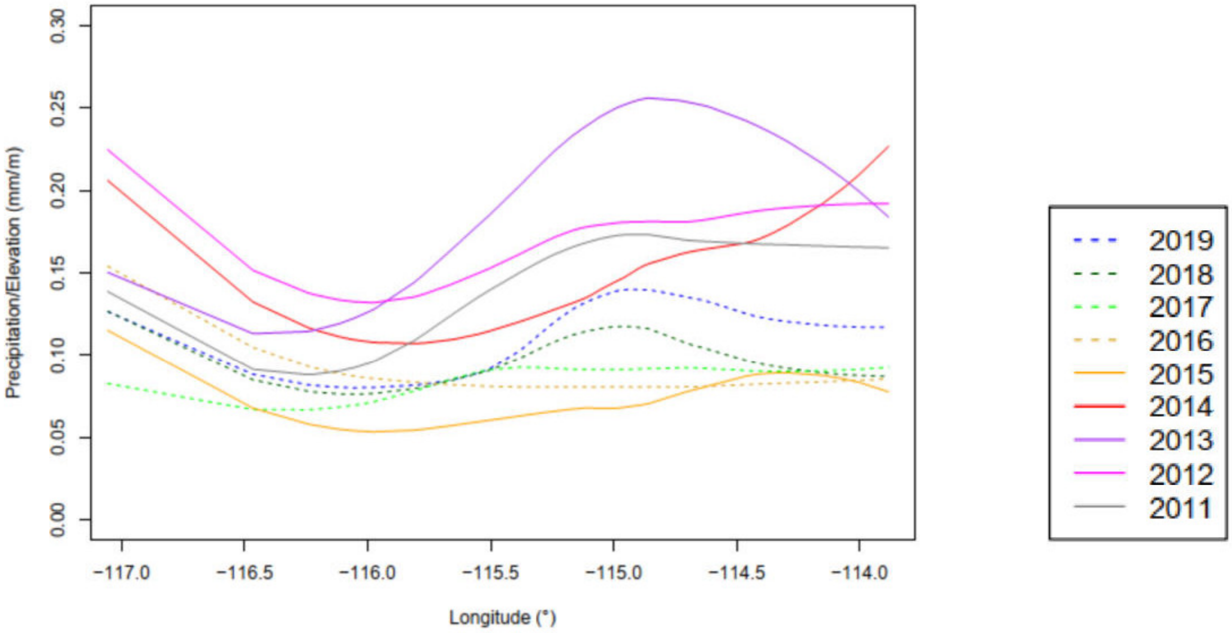

Figure 4.10. LOESS regression of cumulative precipitation during the SPADE period from each year (2011-2019) plotted across the longitudinal coordinate of each station. Cumulative precipitation values at each station were divided by the elevation at each station.

When LOESS curves for cumulative precipitation and elevation were plotted against each other, most curves exhibited similar profiles with peak precipitation values around 2000 m above sea level (Figure 4.11). This may be due to the presence of a smaller number of stations above this point. It could also be due to the increased proportion of the snow precipitation component at higher elevations. Snow is often associated with greater amounts of wind-induced undercatch at station gauges, since this type of hydrometeor is subject to a greater proportion of drag forces (Colli et al. 2015). The majority of precipitation regression curves exhibited a slight dip in values at around 1600 m above sea level. This may be due to some of the disproportionately high precipitation values at -115.5° on the eastern side of the Canadian Rockies, where sites had an elevation below 1600 m above sea level. The precipitation curve for 2013 was substantially larger than the other precipitation curves which may denote the large Alberta flooding event on the eastern side of the Continental Divide. The curve for 2016 was remarkable in that the lowest elevation stations averaged more precipitation than all sites up to 1800 m above sea level.

A LOESS regression of cumulative precipitation during the SPADE period plotted across the precipitation/elevation ratio also demonstrates preferential precipitation accumulation near 2000 m above sea level (Figure 4.12). Latitude did not have a significant correlation with precipitation amounts for any year when the precipitation/elevation ratio was examined in relationship to latitude (Figure 4.13). There was a relatively large contribution of precipitation relative to elevation at the northern latitudes of the study area during the 2011 to 2019 period (although this could be due in part to the effects of outliers). Latitude was not as strong a predictor of precipitation amounts as either elevation or longitude (Figure 4.14).

Latitude did not have a significant correlation with precipitation amounts for the majority of years that were examined.

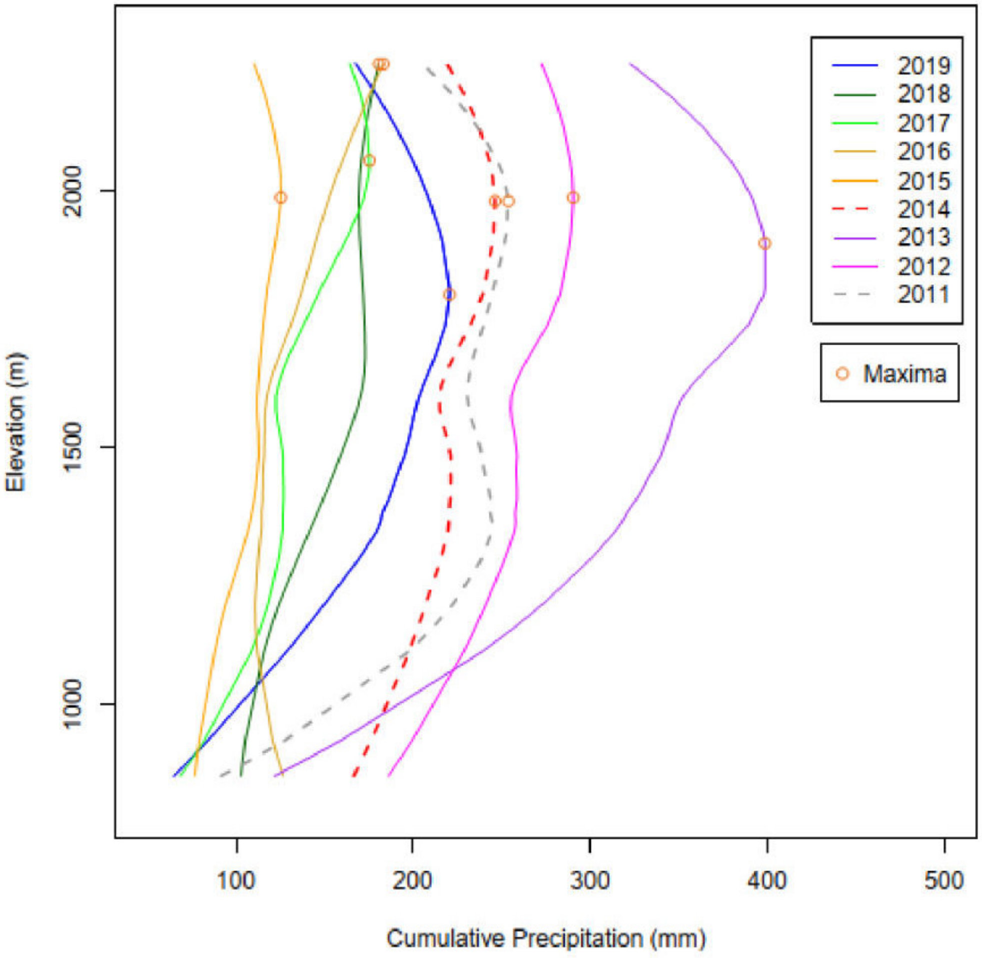

Figure 4.11. LOESS regression of cumulative precipitation during the SPADE period from each year (2011-2019) plotted across the elevation of each station. *Maxima* denote cumulative precipitation maxima from the SPADE period each year.

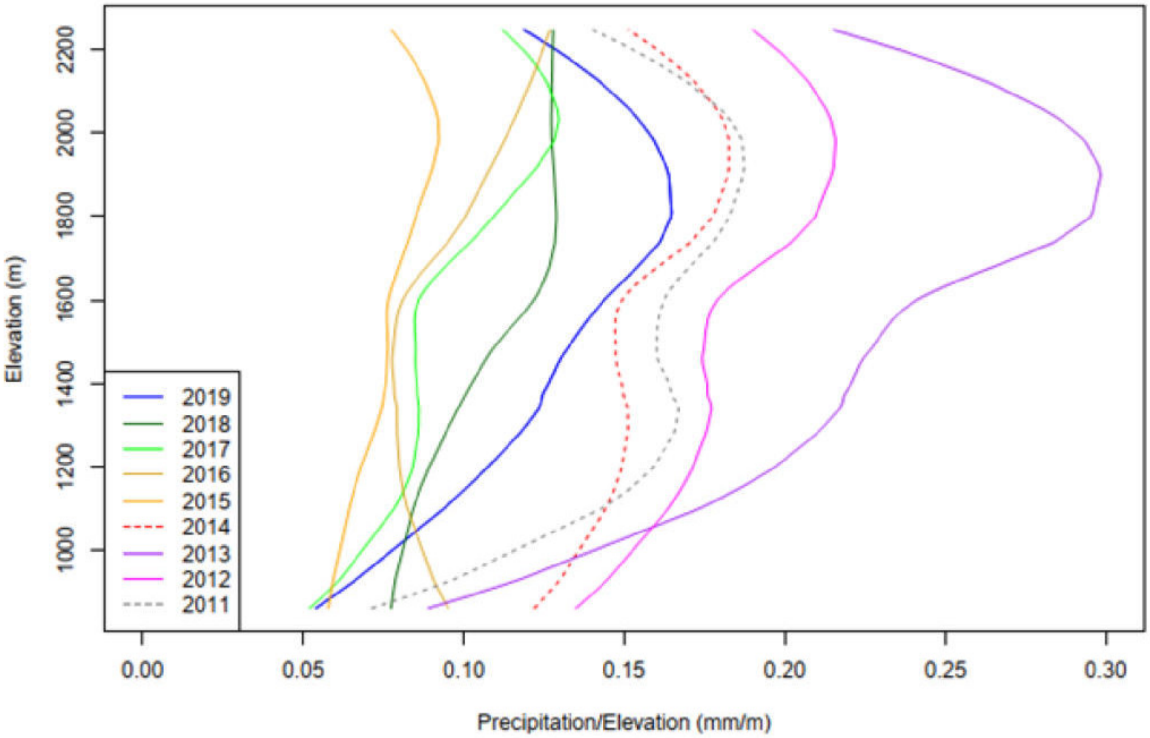

Figure 4.12. LOESS regression of cumulative precipitation during the SPADE period from each year (2011-2019) plotted across the elevation of each station. Each cumulative precipitation value was divided by the elevation of that station.

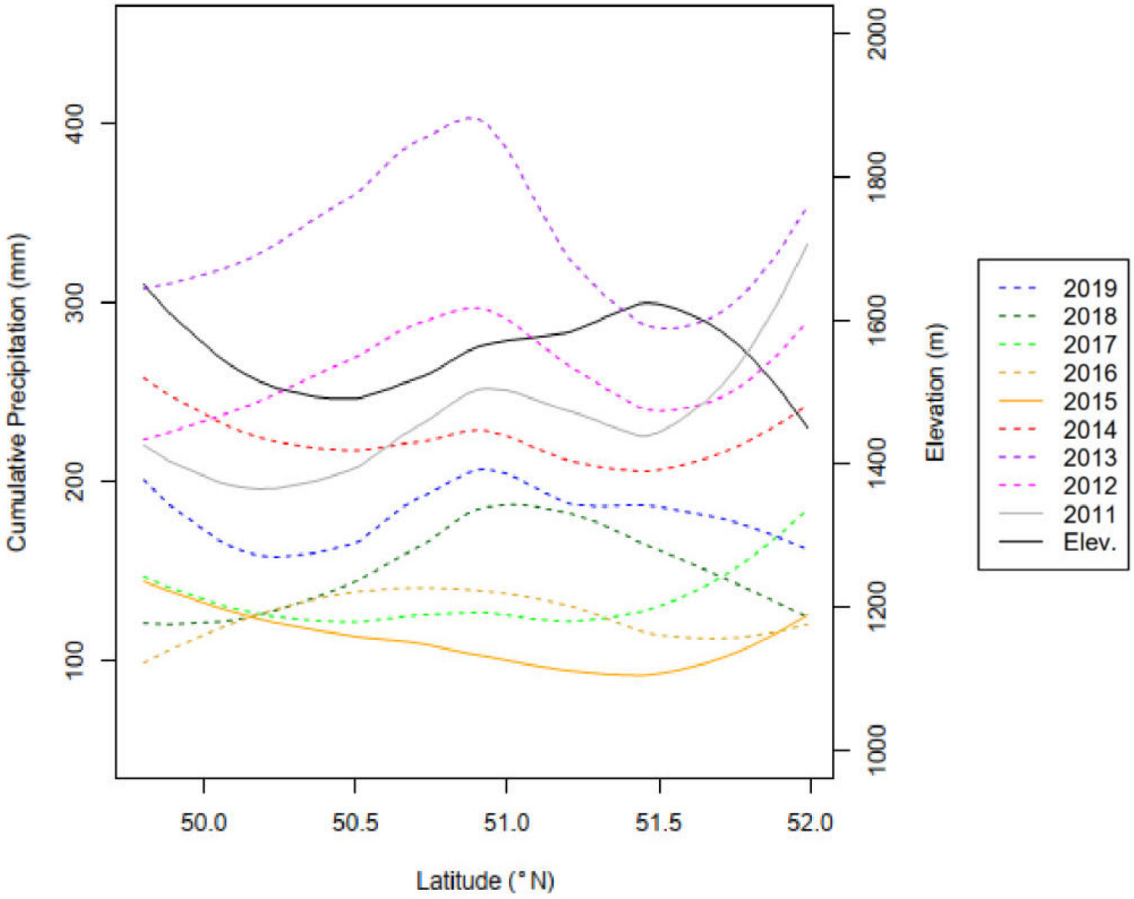

Figure 4.13. LOESS regression of cumulative precipitation during the SPADE period from each year (2011-2019) plotted across the latitude of each station. Solid lines represent significant correlations and dashed lines represent non-significant correlations ($p > 0.05$) between cumulative precipitation and latitude across all years during the May/June period.

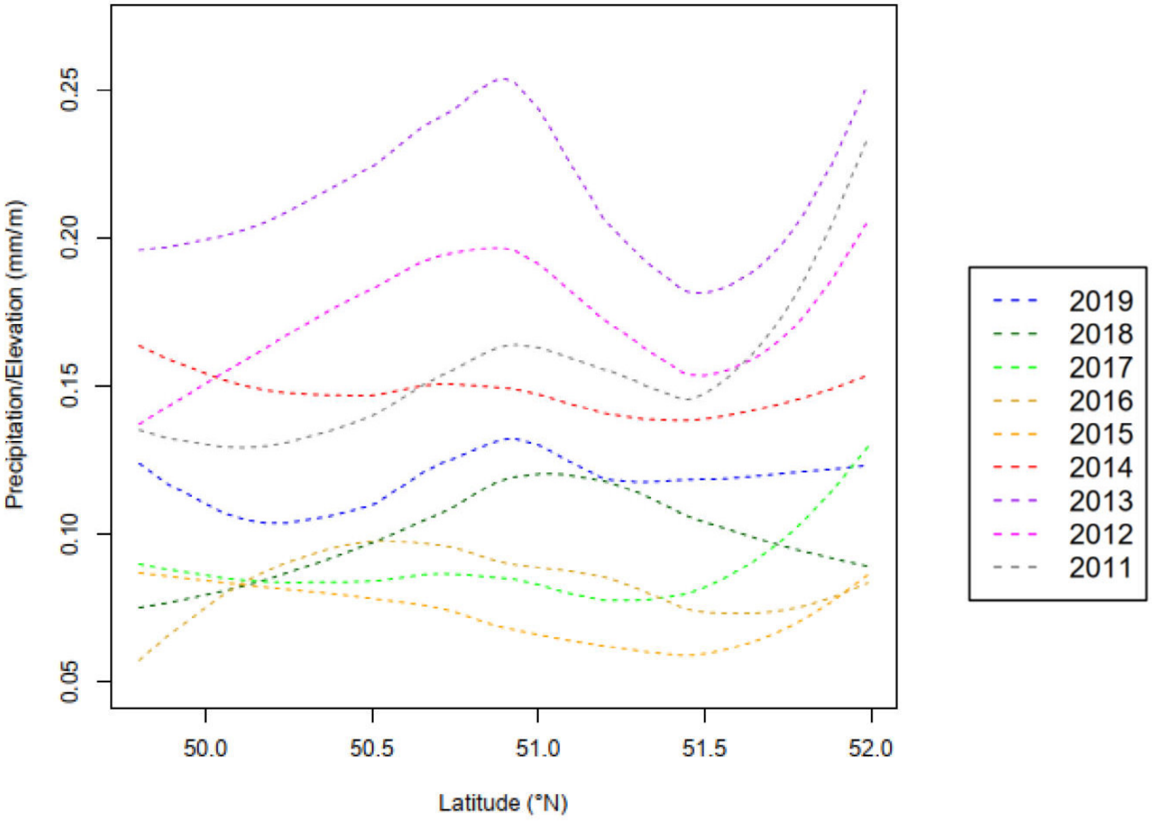

Figure 4.14. LOESS regression of cumulative precipitation during the SPADE period from each year (2011-2019) plotted across the latitude of each station. Solid lines represent significant correlations and dashed lines represent non-significant correlations ($p > 0.05$) between cumulative precipitation and latitude across all years during the May/June period. Cumulative precipitation values were divided by station elevation.

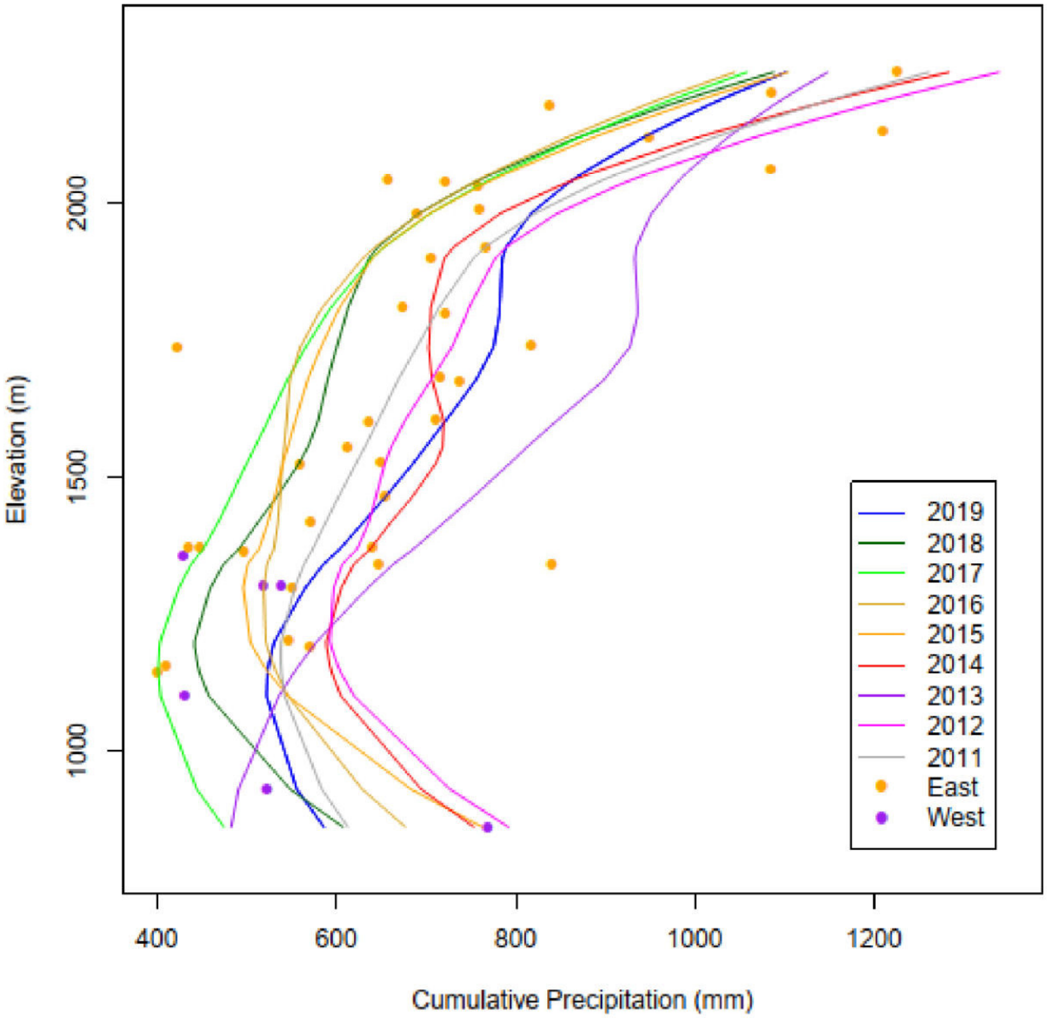

Figure 4.15. LOESS regression curves of annual (not May/June) cumulative precipitation against elevation. Dots represent the mean value for annual precipitation over the 2011-2019 period, with orange dots representing values from the east side of the Continental Divide and purple dots representing values from the west side of the Continental Divide.

When annual precipitation is plotted against elevation the lowest elevation sites have greater amounts of precipitation accumulation than some mid-elevation sites, but the highest elevation sites have the greatest precipitation accumulation (Figure 4.15). A similar plot was produced when the precipitation/elevation ratio was plotted against elevation (Figure 4.16). It highlighted precipitation accumulation at lower elevations that was disproportionately high relative to elevation. The lowest elevation stations were located to the west of the Continental Divide.

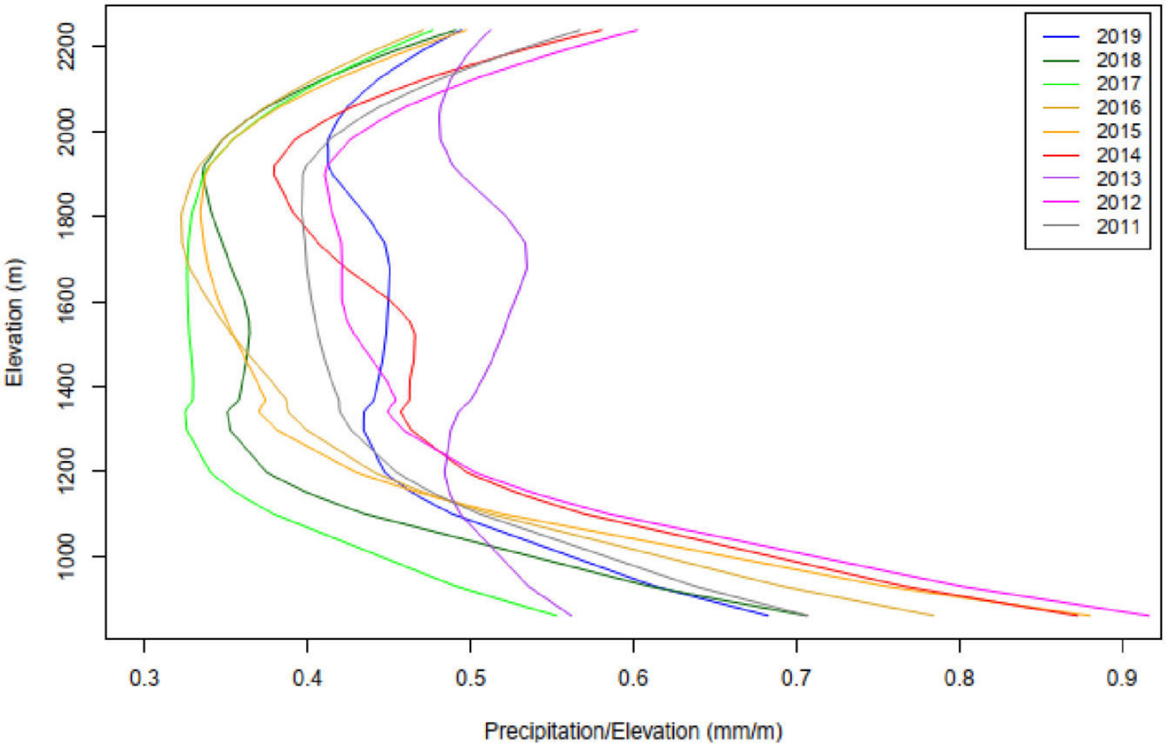

Figure 4.16. LOESS regression curves of annual (not May/June) cumulative precipitation against elevation. Cumulative precipitation is divided by station elevation.

Annual cumulative precipitation had a similar precipitation-elevation curve to SPADE cumulative precipitation, with precipitation increasing with elevation overall (Figure 4.17). Elevation was a significant predictor of cumulative precipitation across all years.

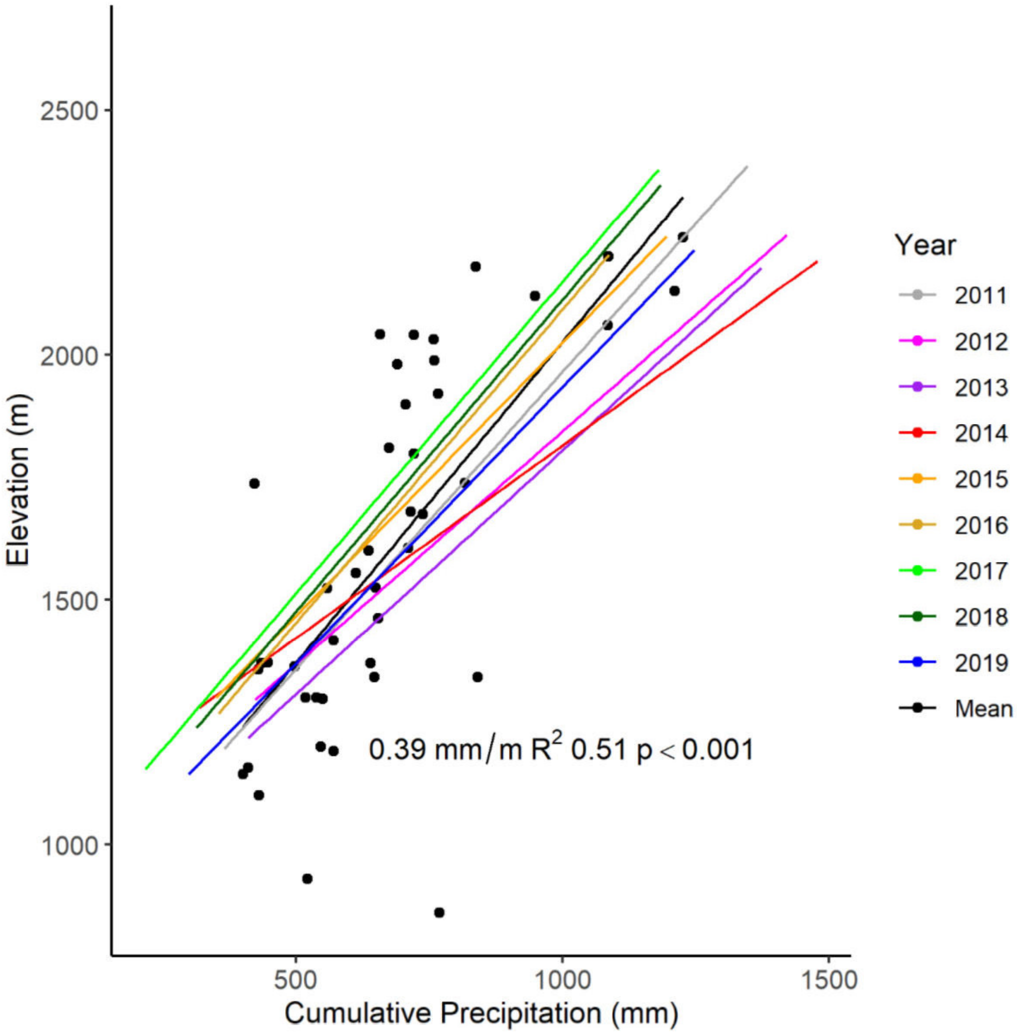

Figure 4.17. A linear model applied to change in elevation with annual precipitation, this change occurs at a rate of 1.31 m mm^{-1} or 0.39 mm m^{-1}. This value represents the slope when station values are averaged across time. Dots represent the mean value for annual precipitation over the 2011-2019 period. (Y=48+0.39Elev, n=43. (Intercept is not significant)).

Annual precipitation-elevation curves differed from SPADE precipitation-elevation curves in that the lowest elevation precipitation sites received more precipitation than mid-elevation sites during the annual time periods. The greatest variation in precipitation amounts between years occurred below about 1900 m above sea level in elevation. Longitude was a smaller predictor of cumulative precipitation (Figure 4.18). Only 2013 exhibited a significant correlation between longitude and precipitation during the LOESS regression. However, a very similar pattern for maximum precipitation accumulation emerges across years with maximum precipitation accumulation occurring between -114° and -115° longitude each year. The precipitation-elevation curve for longitude demonstrated the relatively large contribution of precipitation relative to elevation on the western side of the study area (Figure 4.19).

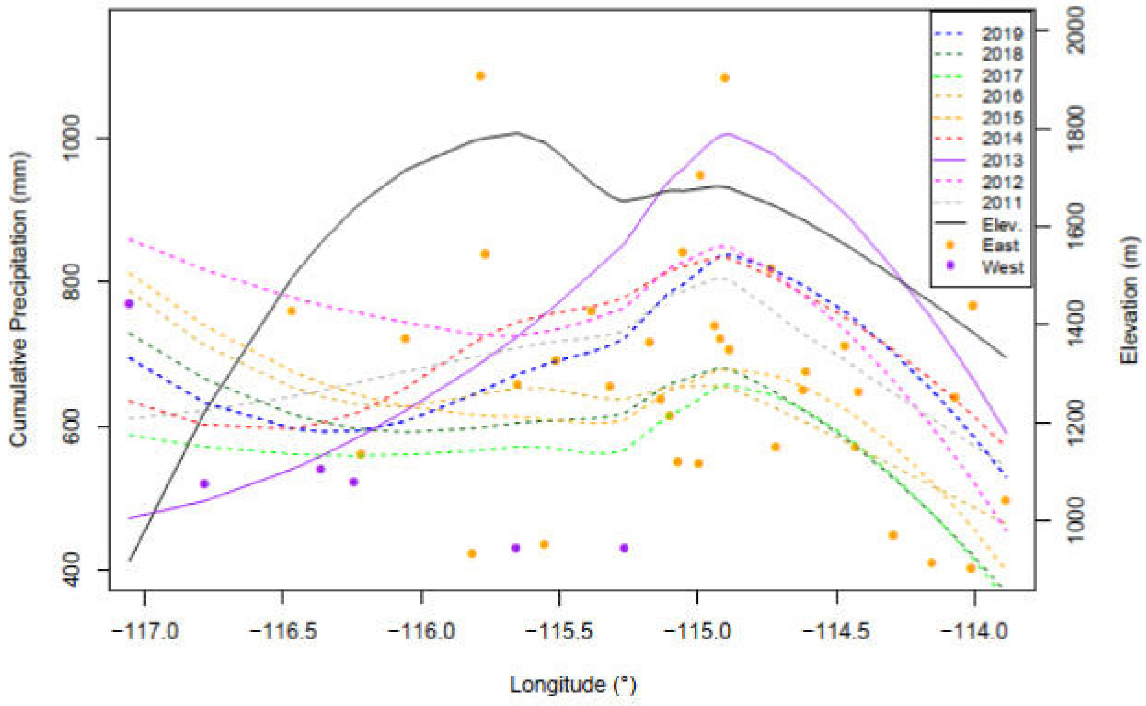

Figure 4.18. LOESS regression curves of annual cumulative precipitation against longitude. Dotted lines represent years in which there was not a significant ($p < 0.05$) correlation between cumulative precipitation and longitude. Dots denote cumulative precipitation at stations. The black line denotes average station elevations at a specific longitude. The elevational profile differs from the previous longitudinal regression because there were fewer stations available for annual time periods between 2011-2019.

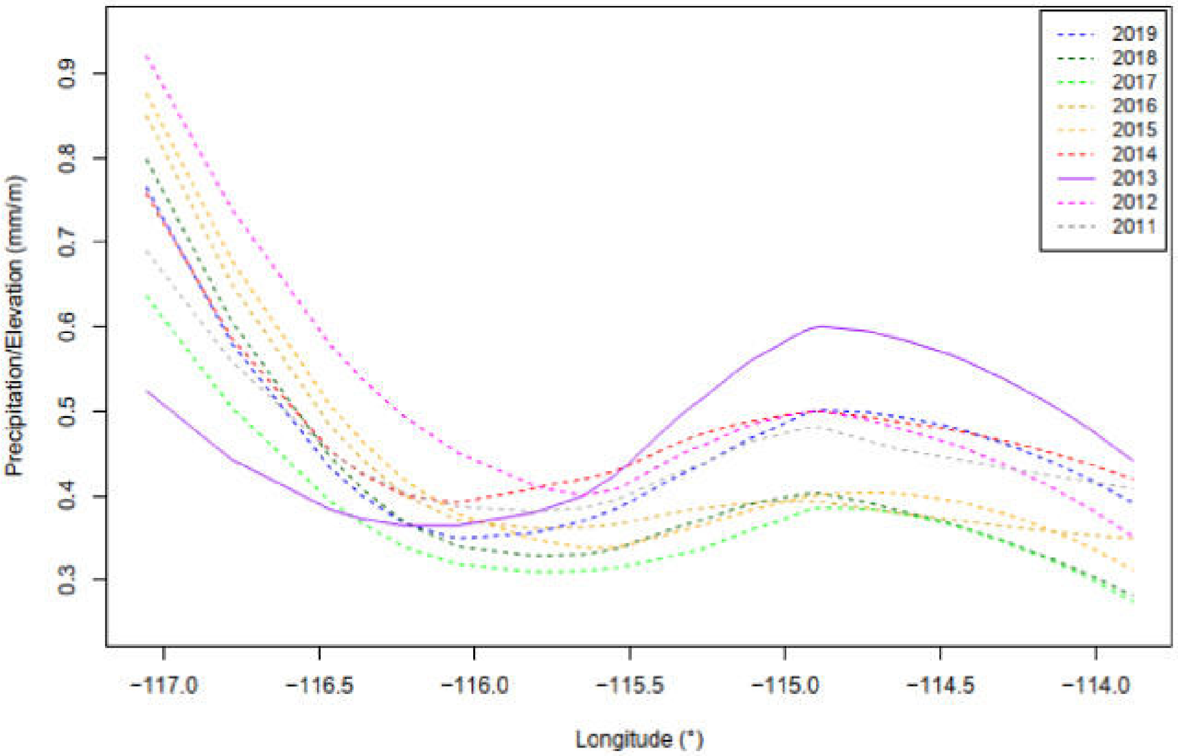

Figure 4.19. LOESS regression curves of annual cumulative precipitation against longitude. Dotted lines represent years in which there was not a significant ($p < 0.05$) correlation between cumulative precipitation and longitude. Dots denote cumulative precipitation at stations. The elevational profile differs from the previous longitudinal regression because there were fewer stations available for annual time periods between 2011-2019.

This plot should be analyzed with caution when examining precipitation on either side of the Continental Divide since this topographical feature is located at an angle across longitude in the southern Canadian Rockies. Latitude was a less important predictor of precipitation accumulation than either elevation or longitude. An examination of annual precipitation amounts in the study area determines that there were no years when latitude was significantly correlated with precipitation (Figure 4.20).

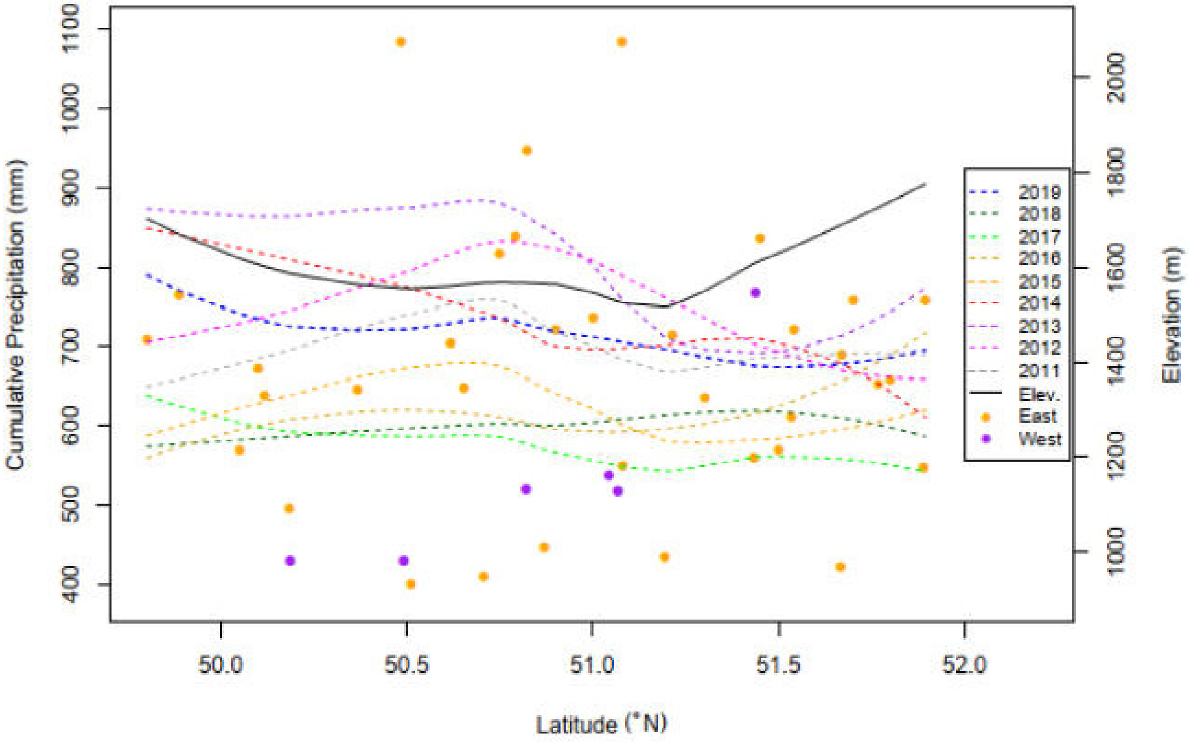

Figure 4.20. LOESS regression curves of annual cumulative precipitation against latitude. Dotted lines represent years in which there was not a significant ($p < 0.05$) correlation between cumulative precipitation and latitude. Dots denote cumulative precipitation at stations. The black line denotes average station elevation at a specific longitude. The latitudinal profile differs from the previous latitudinal regressions because there were fewer stations available for annual time periods between 2011-2019.

Accumulation patterns were less prominent than previous analyses for other variables. However, there was a tendency for slightly increased precipitation near stations at the middle of our study area with a slightly lower elevation (Figure 4.21).

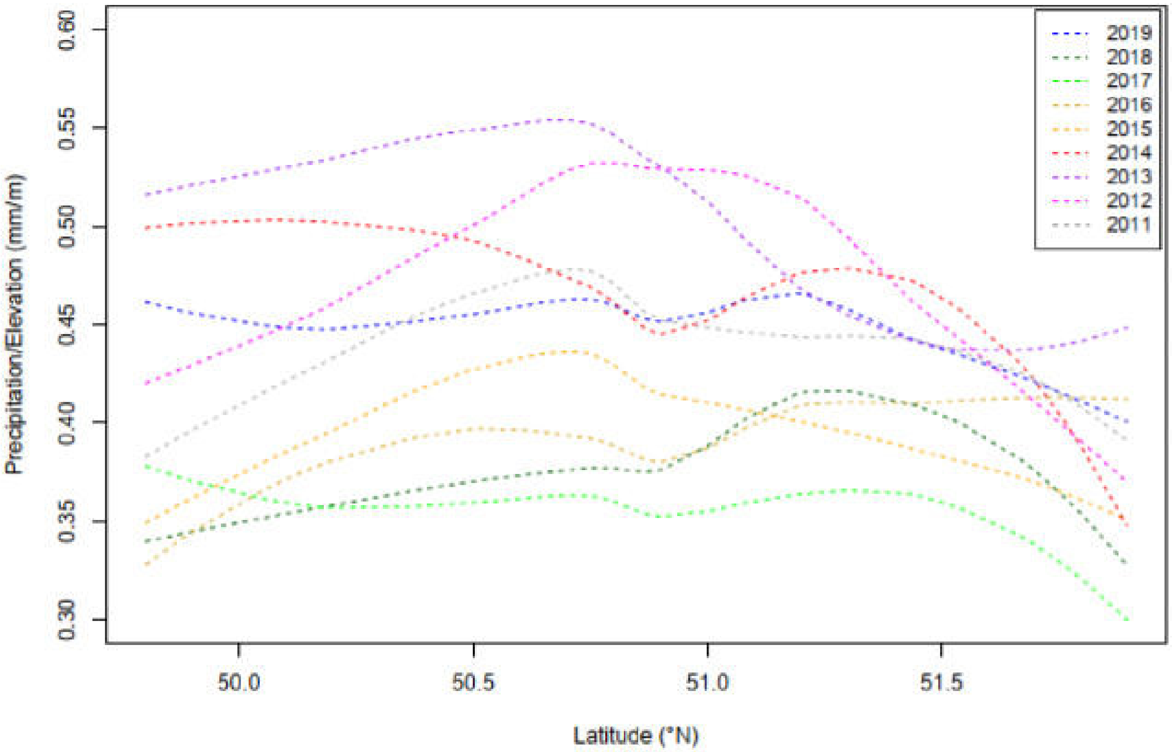

Figure 4.21. LOESS regression curves of annual cumulative precipitation against latitude. Dotted lines represent years in which there was not a significant ($p < 0.05$) correlation between cumulative precipitation and latitude. Dots denote cumulative precipitation at stations. Cumulative precipitation was divided by station elevation at each station.

The regression curve for the precipitation precipitation-elevation ratio versus latitude demonstrates that there could be less precipitation at the northernmost latitudes of the study area during the annual period in comparison to the SPADE period.

4.7 Variability in Precipitation Gradients Across Time

4.7.1 Inter-annual Variability

Cumulative precipitation amounts varied between years (2011-2019) for the SPADE period (Figure 4.22). The highest value precipitation accumulation occurred slightly to the east of the Continental Divide during the SPADE period, except for 2016 and 2017, when large amounts of precipitation accumulation occurred near the Continental Divide. In 2011 maximum precipitation patterns were located in the far eastern margins of the study area.

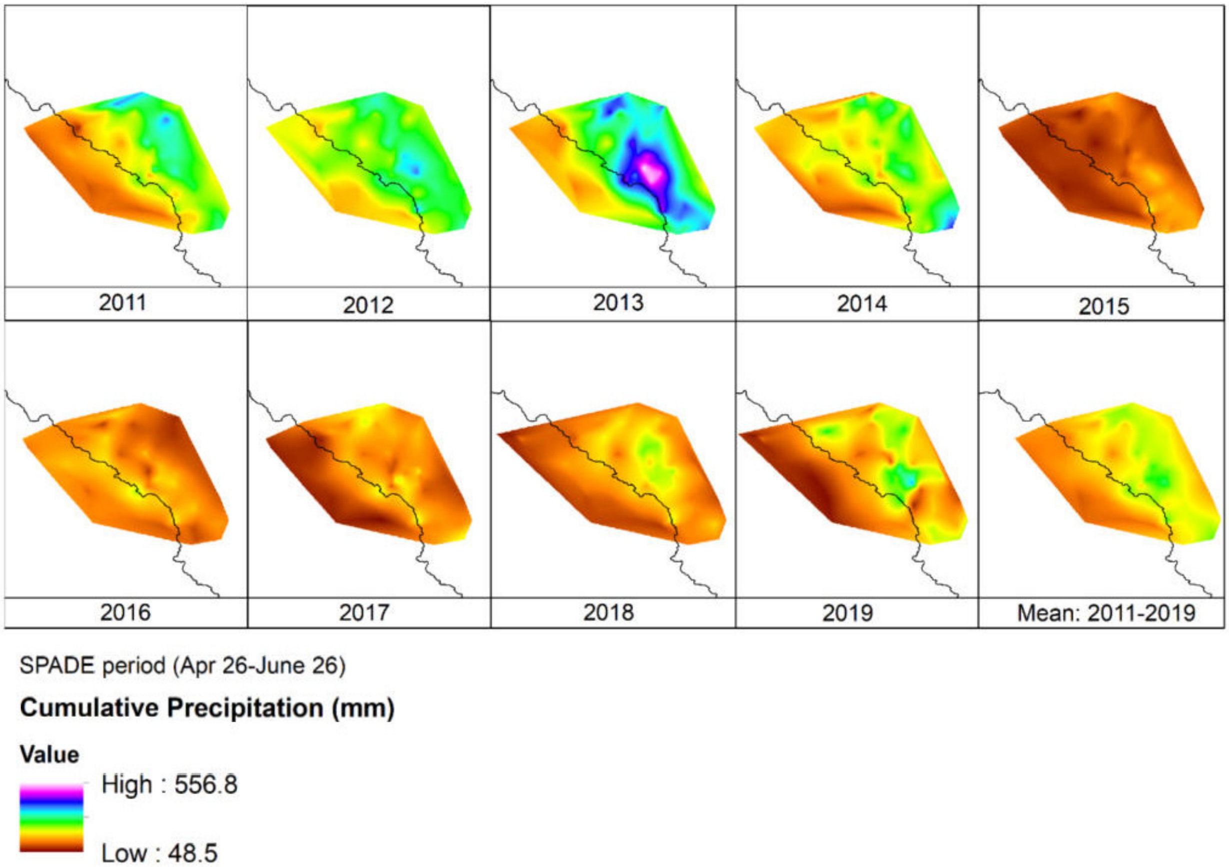

Figure 4.22. Cumulative precipitation during the SPADE period plotted for each year using interpolated accumulated precipitation. Each year was plotted against the maximum cumulative precipitation value for all years (556.8 mm in 2013 which included the Alberta flooding event) and the minimum cumulative precipitation value for all years to demonstrate the relative magnitude of cumulative precipitation for each year.

Substantially more precipitation fell between 2011 and 2014 than between 2015 and 2019 during the SPADE period. On average SPADE periods between 2011 and 2014 had 15%

more precipitation each year than the same time periods between 2015 and 2019, as cumulative precipitation values for this period suddenly decreased between 2014 and 2015. They have grown incrementally each year between 2015 and 2019, however they have not returned to pre-2015 values.

Average cumulative precipitation varied substantially between years (refer to Figure 4.1). The minimum cumulative precipitation amount occurred in 2017, and was 18% less than the annual average of 677 mm. This value was 237 mm less than the maximum value in 2013. Despite large fluctuations in annual precipitation accumulation, the locations of precipitation maxima remained similar across years, with these maxima occurring in a linear fashion along the Continental Divide (Figure 4.23). Occasionally precipitation maxima extended into areas to the east of the Continental Divide, particularly in 2013 and 2019.

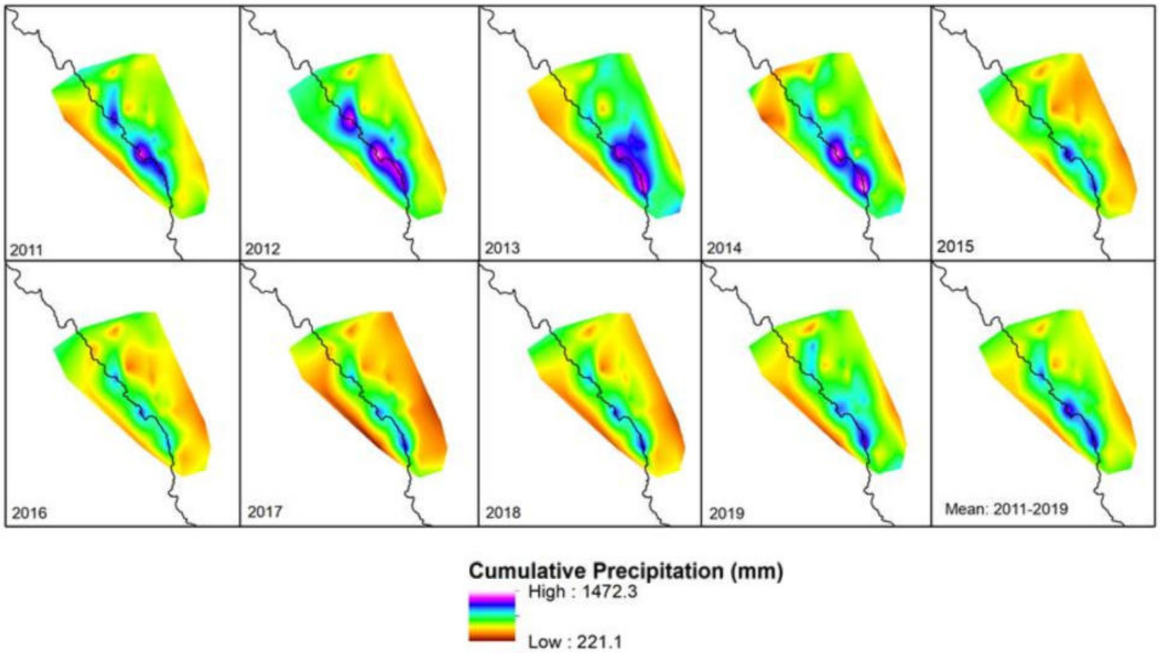

Figure 4.23. Annual precipitation accumulation interpolated against the maximum value and minimum values from all years. These plots display absolute values for precipitation amounts across the years 2011 to 2019.

Each year exhibited distinct precipitation patterns independent of elevation, but both 2013 and 2019 had comparatively large amounts of precipitation proportionate to elevation on the eastern side of the Continental Divide with large bands of precipitation parallel to the Canadian Rockies at lower elevations (Figure 4.24).

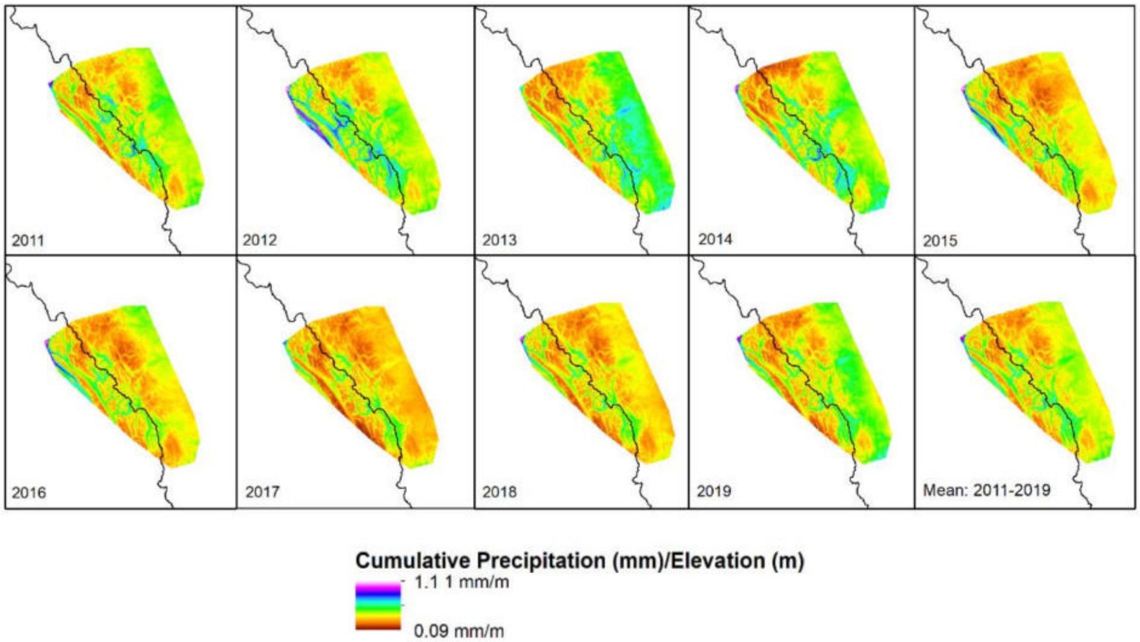

Figure 4.24. Cumulative precipitation amounts divided by elevation for each year. Plots were interpolated relative to the maximum value for all years. Plots highlight changes in precipitation patterns across years.

Precipitation/elevation amounts were relatively low on both sides of the Continental Divide in 2017, with only the Continental Divide exhibiting large amounts of precipitation relative to elevation. Each side of the Continental Divide had a different value for mean precipitation relative to elevation for each year (Figure 4.25). The eastern side of the Continental Divide had much larger average precipitation/elevation ratios in 2013 and 2019, while the reverse occurred during 2012. The western side of the Continental Divide had larger average precipitation/elevation ratios than the eastern side of the Continental Divide during 2015 and 2016, but this difference was not as pronounced as during 2012. Both sides of the Continental Divide had similar precipitation/elevation ratios in 2011, 2014, and 2017, with 2017 exhibiting the lowest values overall.

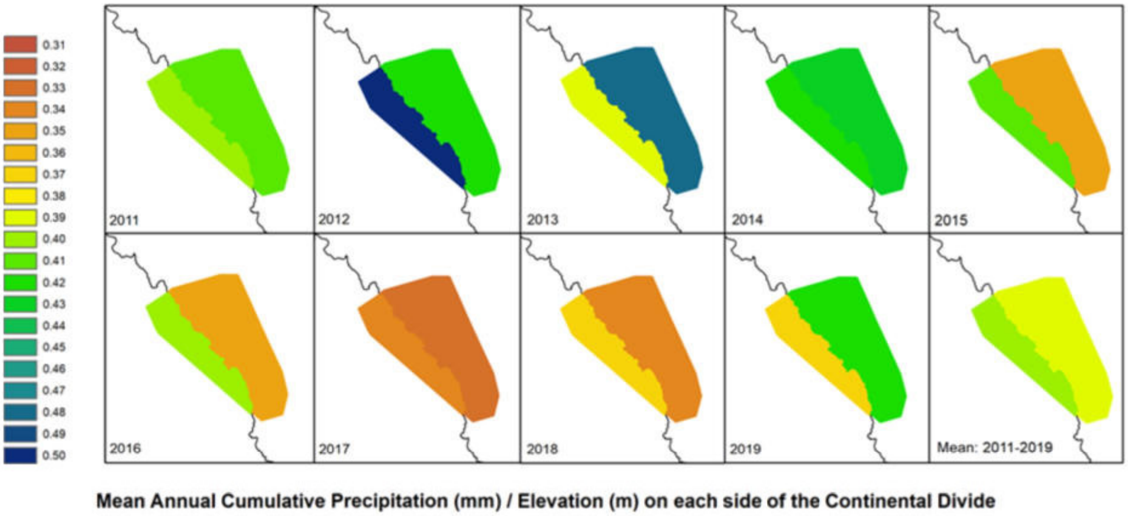

Figure 4.25. Mean annual cumulative precipitation/elevation compared across years on each side of the Continental Divide. Orange and yellow values indicate that a region had a comparatively low value of precipitation relative to elevation, while blue and green values indicate that a region had a comparatively high value of precipitation relative to elevation.

When station coefficient of variation was examined across years, coefficient of variation decreased with elevation (Figure 4.26). The lowest coefficient of variation was associated with some sites with the highest rates of annual precipitation.

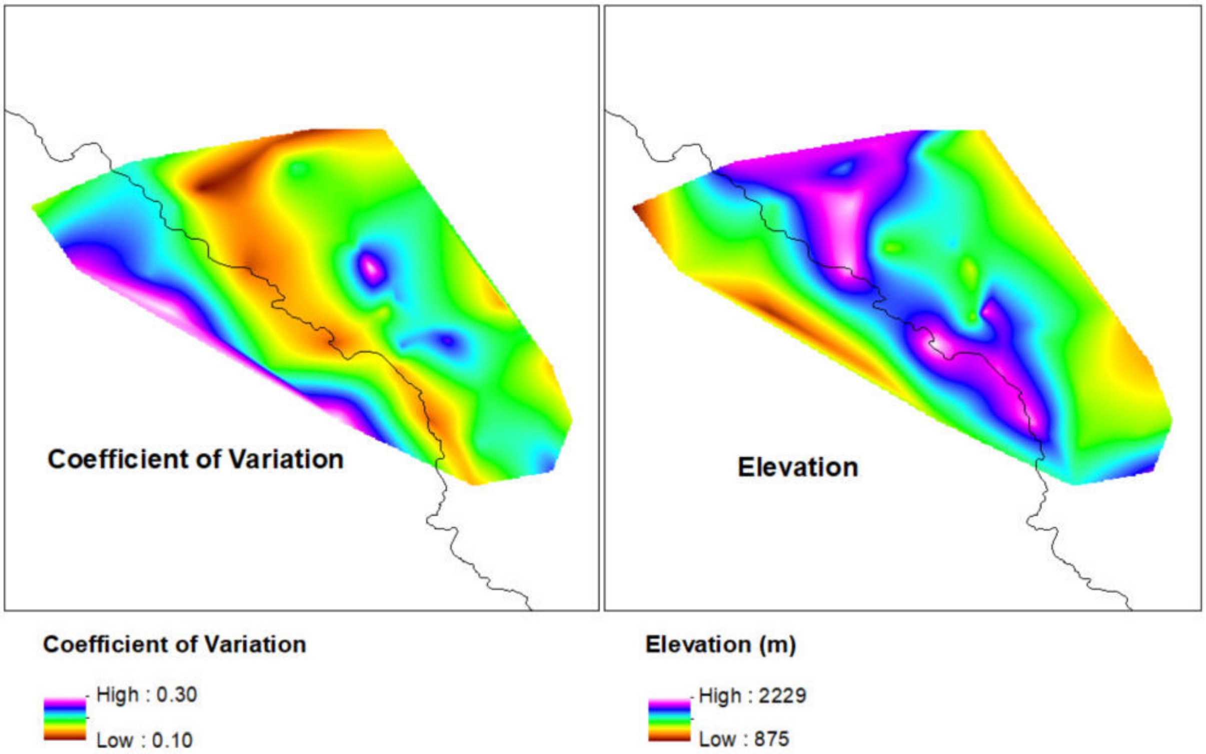

Figure 4.26. (Left) Interpolation of coefficient of variation for each meteorological station across years (2011 to 2019) in the study area (Right) Interpolation of elevation at each station.

4.7.2 Intra-annual Variability

Seasonal amounts of precipitation per day vary across years (Figure 4.27). Summer (June, July, and August) has the highest amounts of precipitation per day for all years except for 2011 and 2017 (in 2017 summer had the lowest average precipitation per day for all of the seasons). Winter precipitation may be inversely related to summer precipitation. Spring averaged slightly more precipitation per day in comparison to fall, however fall exhibited greater daily precipitation values than spring during a few years.

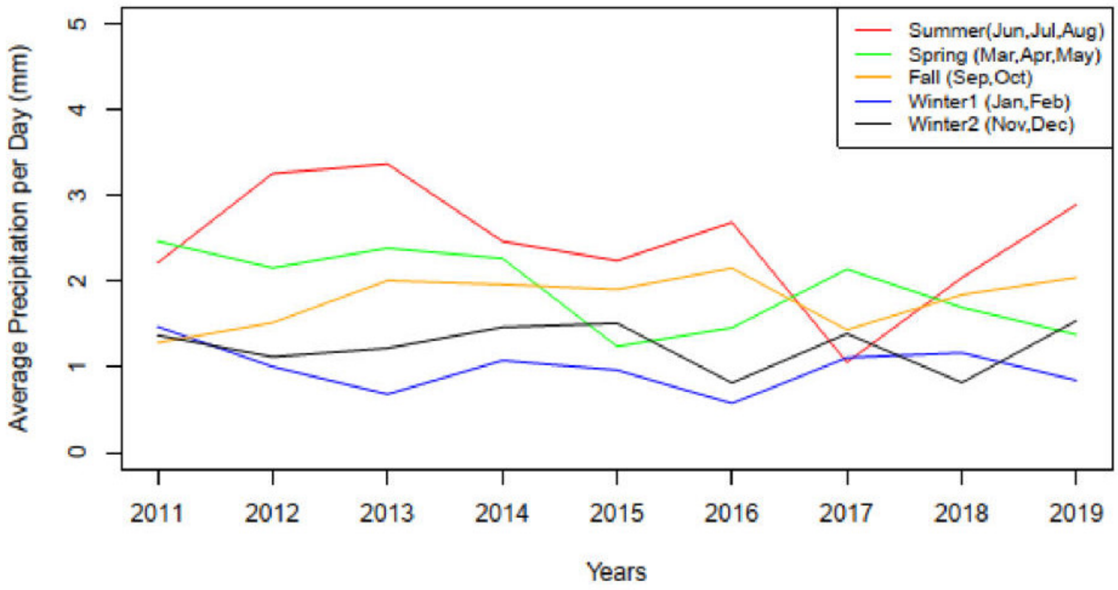

Figure 4.27. Average daily precipitation for each season plotted across years (2011-2019) for all stations in the study area.

Spring exhibited the highest daily precipitation values in 2011 and 2017 (Figure 4.28). In this study area summer exhibited the largest precipitation values and the greatest span in precipitation values across years, conversely fall exhibited relatively low precipitation values and a relatively small span in average daily precipitation values.

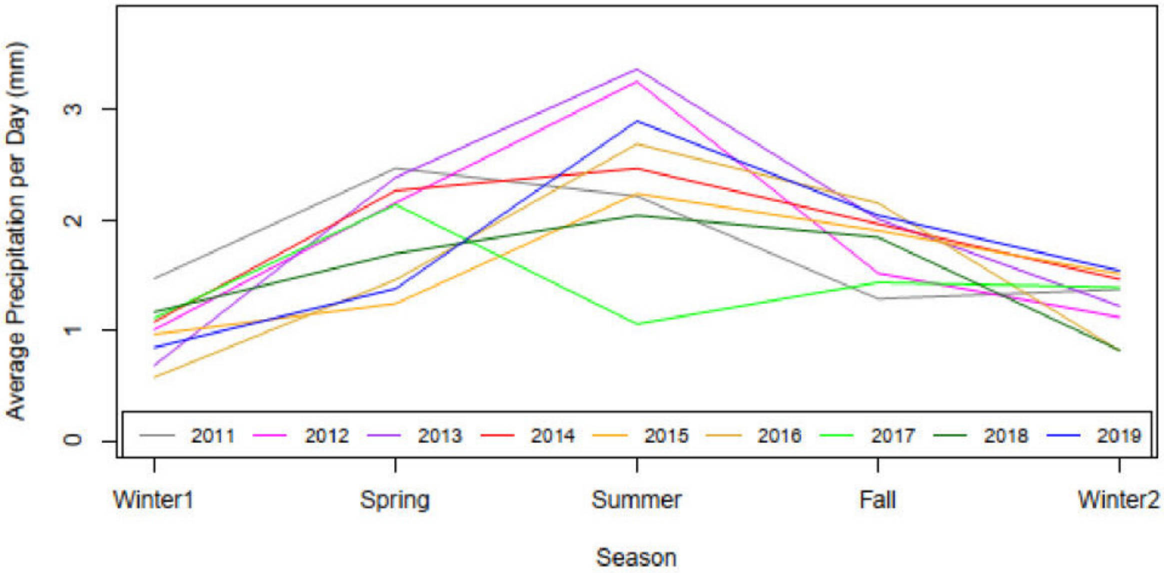

Figure 4.28. Average daily precipitation for each year plotted across seasons. (Winter: January, February, November, and December, Spring: March, April and May, Summer: June, July, and August, and Fall: September and October).

Precipitation patterns for the two warmest months exhibited a larger distribution of high precipitation accumulation across the study area than the two coldest months (Figure 4.29). Precipitation patterns for the two warmest months, July and August, exhibited little spatial homogeneity within and across years and the highest precipitation values were not associated with the highest elevation sites in the study area. Precipitation patterns for the two coolest months exhibited greater spatial homogeneity within and across years and larger precipitation values appeared to be more closely associated with higher elevation regions in the study area. A linear pattern of high accumulation along the crest of the Continental Divide often developed during these colder months.

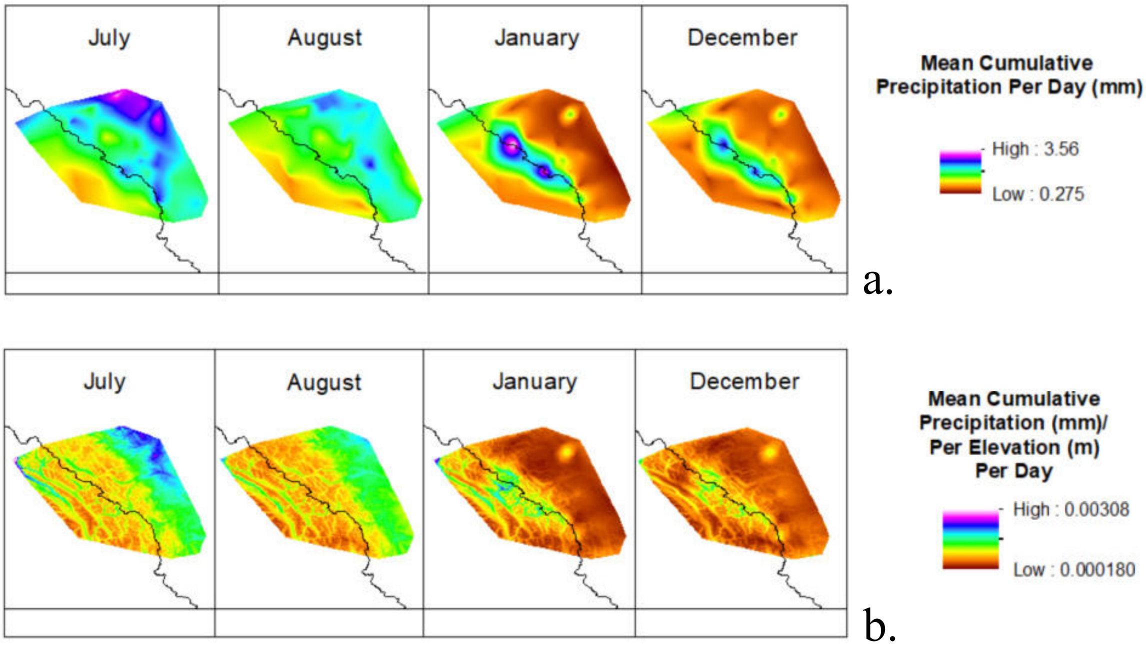

Figure 4.29. Some examples precipitation accumulation patterns interpolated from the two warmest months on either side of the Continental Divide (July and August), when precipitation is largely liquid, and from the two coldest months on either side of the Continental Divide (January and December), when precipitation is largely solid. Precipitation patterns are for the 2011-2019 period. (a.) Mean cumulative precipitation. (b.) Mean cumulative precipitation gradients.

When precipitation patterns were grouped according to season per year, cold seasons exhibited linear patterns that were closely aligned with higher elevation sites than other seasons (Figure 4.30). The summer season exhibited similar precipitation patterns to those belonging to July and August, with little spatial homogeneity. Spring and fall exhibited precipitation patterns that appeared as a slight blending between adjacent seasons. Both spring and fall were more similar to winter precipitation patterns than summer patterns upon visual inspection, with more precipitation occurring in higher elevation regions of the study area than lower elevation regions of the study area.

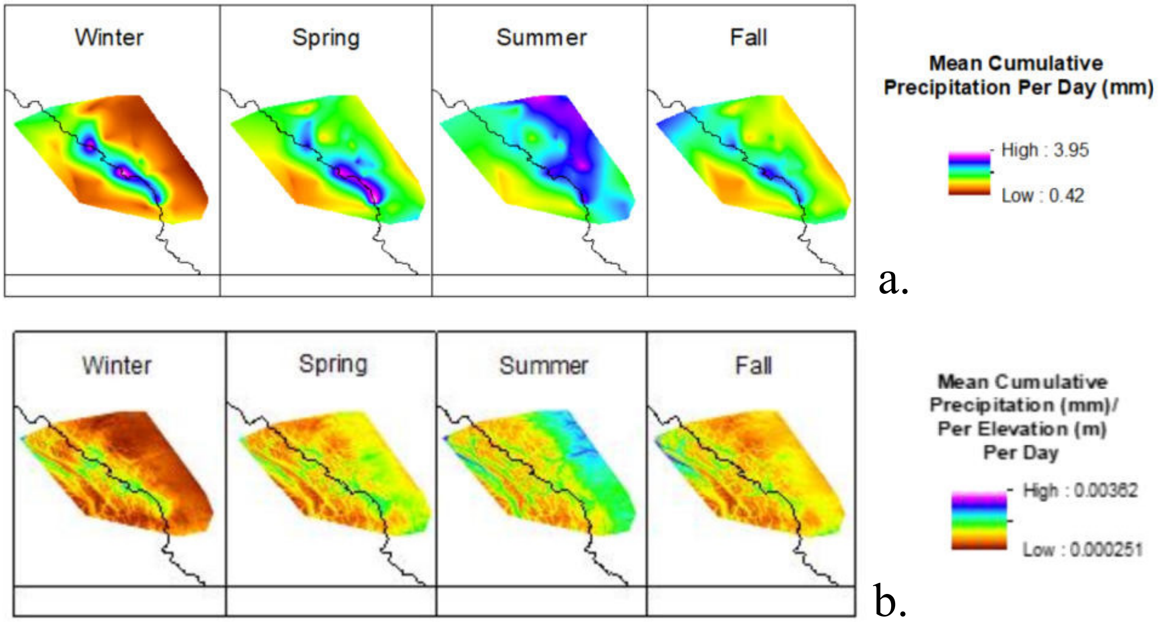

Figure 4.30. Interpolated precipitation patterns from each season for the 2011-2019 period. (a.) Mean cumulative precipitation patterns. (b.) Mean cumulative precipitation gradients.

4.8 Examining Temperature Patterns on either side of the Continental Divide

Stations on the western side of the Continental Divide, which have a lower average elevation than stations on the eastern side of the Continental Divide, exhibited higher values for annual maximum, average, and minimum temperature profiles in comparison to the eastern side of the Continental Divide. Maximum temperature profiles had similar shapes for both the eastern and western sides of the Continental Divide (Figure 4.31).

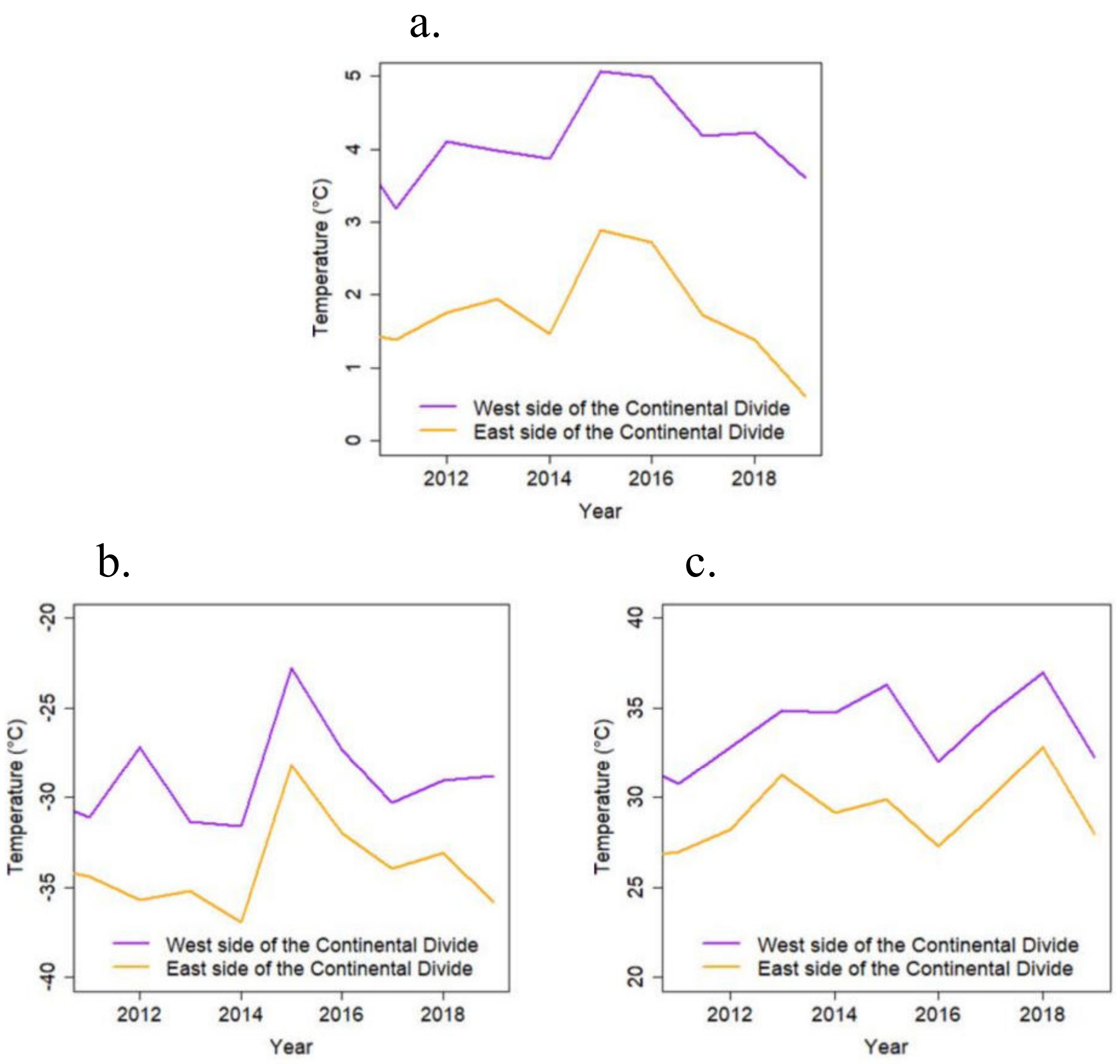

Figure 4.31. Temperature profiles of stations in the SPADE study area across years. (a.) Average temperatures across years (2006 to 2019) on either side of the Continental Divide. (b.) Minimum temperatures across years on either side of the Continental Divide. (c.) Maximum temperatures across years on either side of the Continental Divide.

There was a pronounced decrease in maximum temperatures on both sides of the Continental Divide during 2016. Meanwhile, the highest maximum temperatures occurred during 2018 on both sides of the Continental Divide. Average temperatures varied between years on both sides of the Continental Divide, with higher average temperatures during 2015 and 2016. There was a slight peak in average temperature during 2012 on the western side of the Continental Divide and during 2013 on the eastern side of the Continental Divide. The lowest average temperatures during this period occurred during 2019 on the eastern side of the Continental Divide. Average temperatures were unremarkable on the western side of the Continental Divide in 2019, resulting in the largest gap in temperatures between the two sides (about 4.5°C). There was a large peak in minimum temperatures in 2015 and 2016. Minimum temperature profiles were not as similar on either side of the Continental Divide as average and maximum temperature profiles, with a peak on the western side not being reflected on the eastern side.

When temperatures were corrected for elevation on either side of the Continental Divide using the average lapse rates, the eastern and western sides of the Continental Divide had similar temperatures (Figure 4.32). The eastern side of the Continental Divide exhibited a larger range of temperatures than the western side of the Continental Divide.

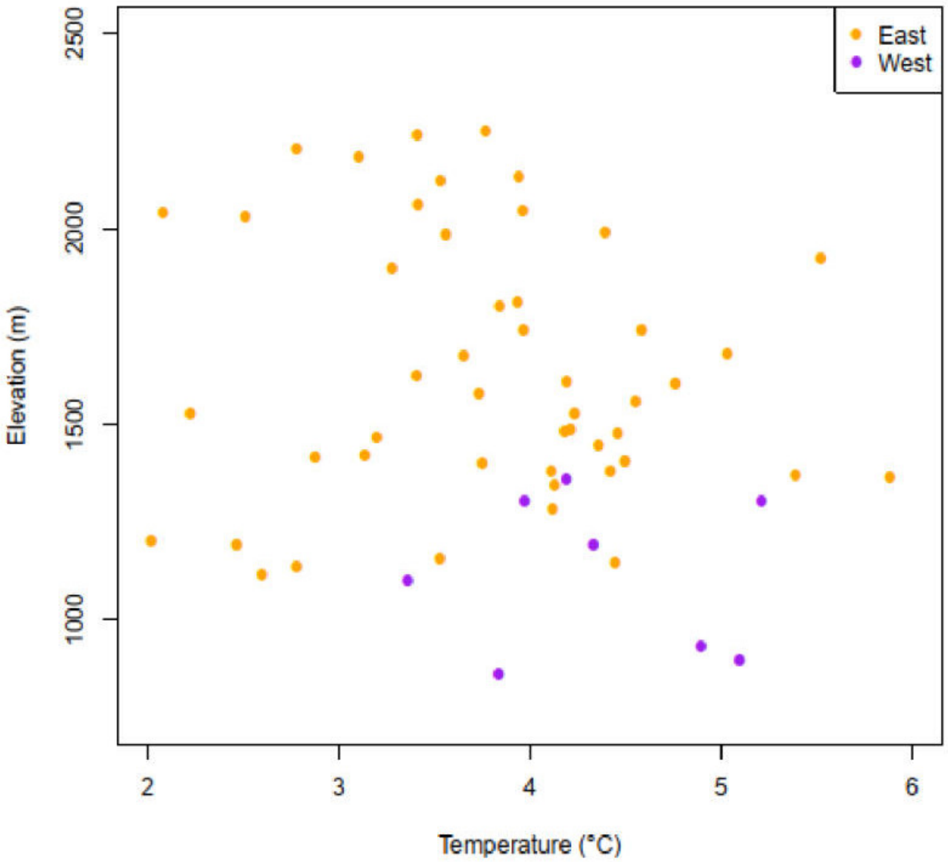

Figure 4.32. Adjusted temperatures from the eastern side of the Continental Divide (orange) and the western side of the Continental Divide (purple) from the 2011 to 2019 period. Temperatures are corrected to reflect an elevation of 1100 m which is equivalent to the elevation at Nipika. This was completed using the calculated lapse rates for each side of the Continental Divide. The lapse rate was calculated to be -3.8° C km^{-1} for the eastern side of the Continental Divide and -4.8° C km^{-1} for the western side of Continental Divide.

Temperatures decreased with elevation on either side of the Continental Divide (Figure 4.33). Although temperatures varied between years, the shape of the temperature profile across elevations did not visibly change between years. On the eastern side of the Continental Divide, temperatures remained relatively similar across elevations until about 2000 m above sea level, where temperatures decreased at a faster rate than at lower elevations.

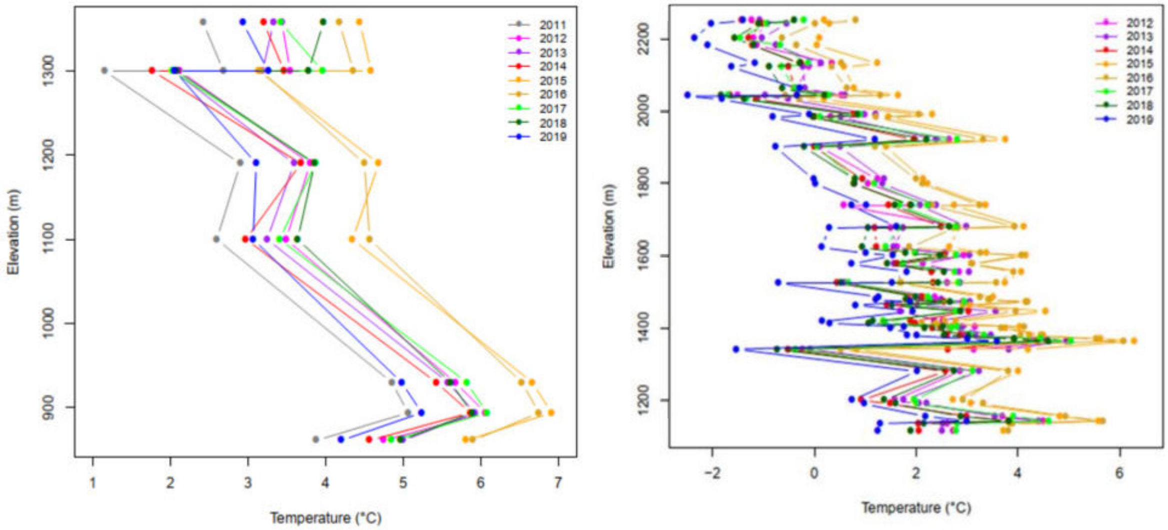

Figure 4.33. (Left) Mean annual temperature for each year at each station on the western side of the Continental Divide with a linear plot across elevation to illustrate changes in temperature across elevation. (Right) Mean annual temperature for each year at each station on the eastern side of the Continental Divide with a linear plot across elevation to illustrate changes in temperature across elevation.

Mean annual temperature does not appear to have a linear relationship with mean annual cumulative precipitation on either side of the Continental Divide (Figure 4.34). A period of lower precipitation on the eastern side of the Continental Divide coincided with warmer temperatures, while the reverse pattern was true for the western side of the Continental Divide.

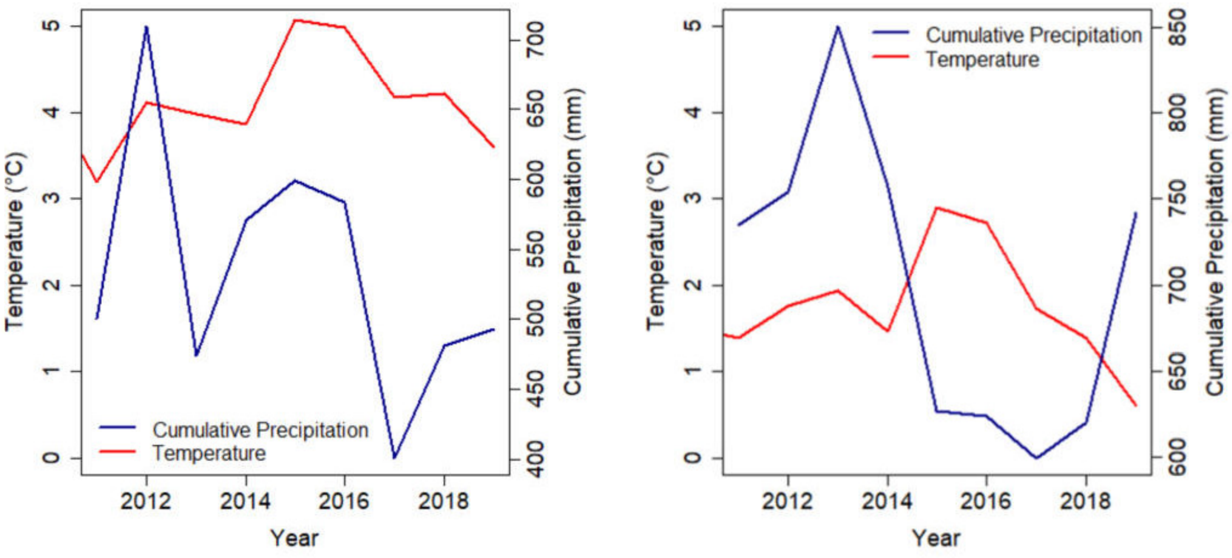

Figure 4.34. (Left) Cumulative precipitation in relation to temperature on the western side of the Continental Divide. (Right) Cumulative precipitation in relation to temperature on the eastern side of the Continental Divide.

4.9 Relationships between cumulative precipitation and wind/storm patterns

4.9.1 Wind-Precipitation Relationships at Observation Sites During SPADE events

The four largest precipitation events exhibited periods of relatively low wind velocities at Nipika (Figure 4.35 and Appendix F). Precipitation occurred most frequently when wind was blowing from a southerly component of the wind rose (Figure 4.34 (e-h)). These events were characterized by the largest amounts of precipitation across the SPADE study area and occurred over large time-frames relative to all events (except for Event 12 which also occurred over a similar time-frame (Table 5.1)).

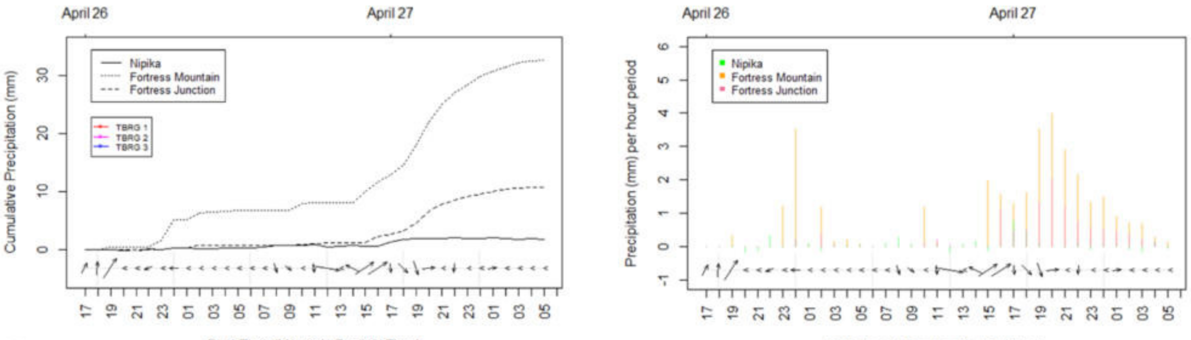
April 26
April 27
Cumulative Precipitation (mm)
Nipika
Fortress Mountain
Fortress Junction
TBRG 1
TBRG 2
TBRG 3
Date/Time (Mountain Daylight Time)
Precipitation (mm) per hour period
Nipika
Fortress Mountain
Fortress Junction
Date/Time (Mountain Daylight Time)

a.

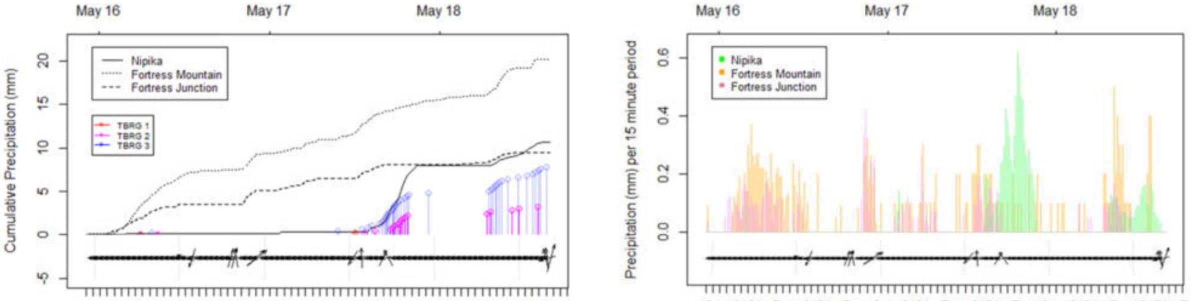
May 16
May 17
May 18
Cumulative Precipitation (mm)
Nipika
Fortress Mountain
Fortress Junction
TBRG 1
TBRG 2
TBRG 3
Date/Time (Mountain Daylight Time)
Precipitation (mm) per 15 minute period
Nipika
Fortress Mountain
Fortress Junction
Date/Time (Mountain Daylight Time)

b.

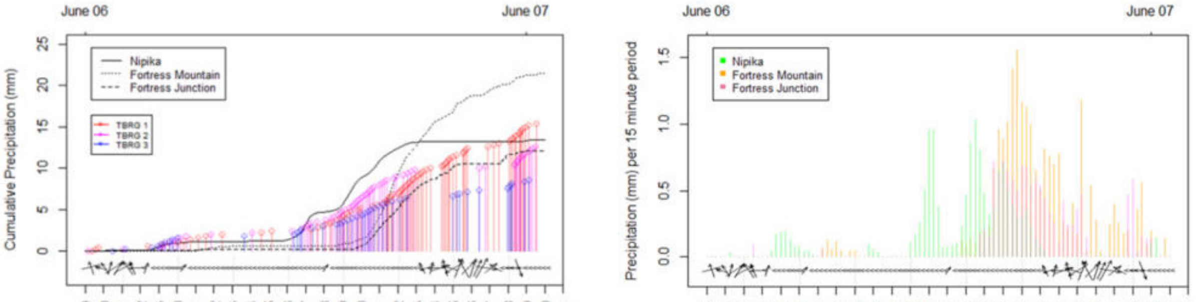
June 06
June 07
Cumulative Precipitation (mm)
Nipika
Fortress Mountain
Fortress Junction
TBRG 1
TBRG 2
TBRG 3
Date/Time (Mountain Daylight Time)
Precipitation (mm) per 15 minute period
Nipika
Fortress Mountain
Fortress Junction
Date/Time (Mountain Daylight Time)

c.

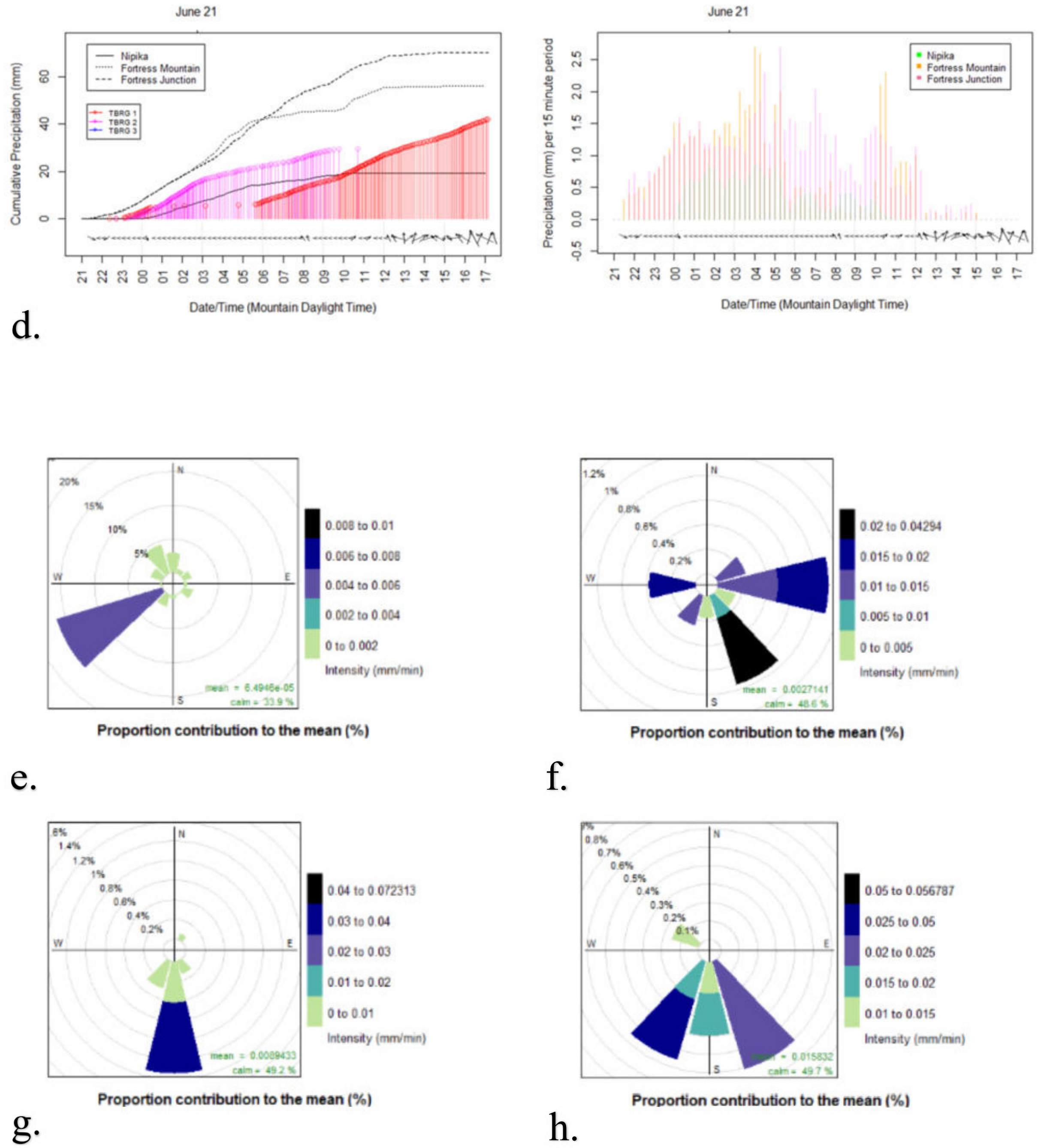

Figure 4.35. The four major SPADE precipitation events: (a) Event 1 (16:50 MDT 26 April 2019 to 5:00 MDT 28 April 2019) was 35.8 hours long. Water vapour flux was strongly upslope. (b) Event 5 (23:00 MDT 15 May 2019 to 16:30 MDT 18 May 2019) was 65.5 hours long. Water vapour flux was from the southeast (c) Event 9 (19:00 MDT 6 June 2019 to 20:00 MDT 7 June 2019) was 25 hours long. Moisture flux was upslope (d) Event 13 (21:30 MDT 20 June 2019 to 17:40 MDT 21 June 2019) was 20.25 hours. Water vapour flux was upslope, but transitioned to a northerly direction towards the end of the event. Precipitation roses for each of these events, Event 5 (e), Event 9 (f), Event 12 (g), and Event 13 (h) are also included with wind values less than 0.5 m s^{-1} removed.

Event 6 (Figure 4.36(a) and (d)) exhibited the strongest correlation between cumulative precipitation amounts and elevation of all events at SPADE stations ($r = 0.98$, and $p < 0.001$) (Event 7 exhibited a similar but slightly smaller relationship between precipitation and elevation). Modified Event 10a (Figure 4.36 (b) and (e)) was the only event where the western side of the Continental Divide received more precipitation than the eastern side of the Continental Divide. This event exhibited a negative, but non-significant correlation between elevation and cumulative precipitation amounts at SPADE stations ($r = -0.31$, $p > 0.05$). Event 12 (Figure 4.36 (c) and (f)) exhibited a change in a vapour flux, with this flux changing from a northerly direction to an upslope direction. Precipitation from several directions can be clearly seen on the precipitation rose. There was a low and non-significant correlation between elevation and precipitation amounts during this event at SPADE stations ($r = 0.48$, $p > 0.05$). Precipitation intensities varied across this event, particularly at the precipitation gauge transect.

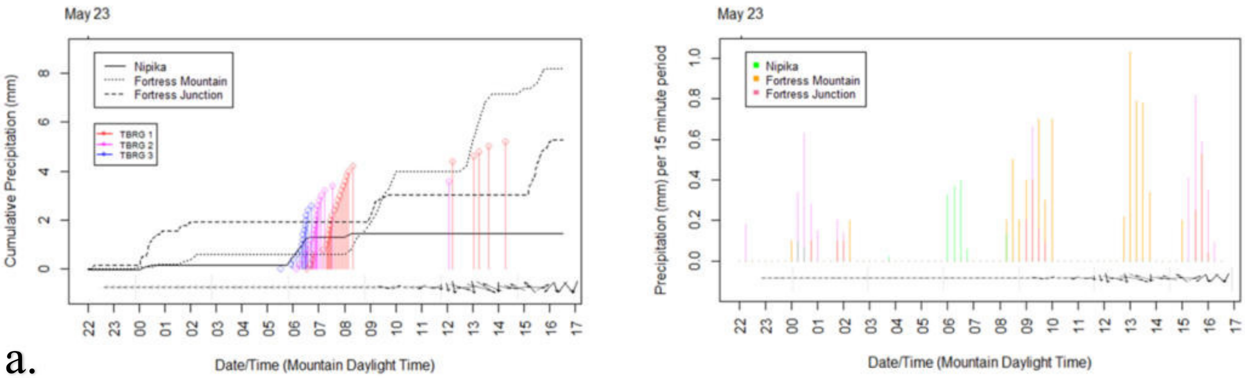
May 23
Cumulative Precipitation (mm)
Nipika
Fortress Mountain
Fortress Junction
TBRG 1
TBRG 2
TBRG 3
0
2
4
6
8
22 23 00 01 02 03 04 05 06 07 08 09 10 11 12 13 14 15 16 17
Date/Time (Mountain Daylight Time)
May 23
Precipitation (mm) per 15 minute period
Nipika
Fortress Mountain
Fortress Junction
0.0
0.2
0.4
0.6
0.8
1.0
22 23 00 01 02 03 04 05 06 07 08 09 10 11 12 13 14 15 16 17
Date/Time (Mountain Daylight Time)

a.

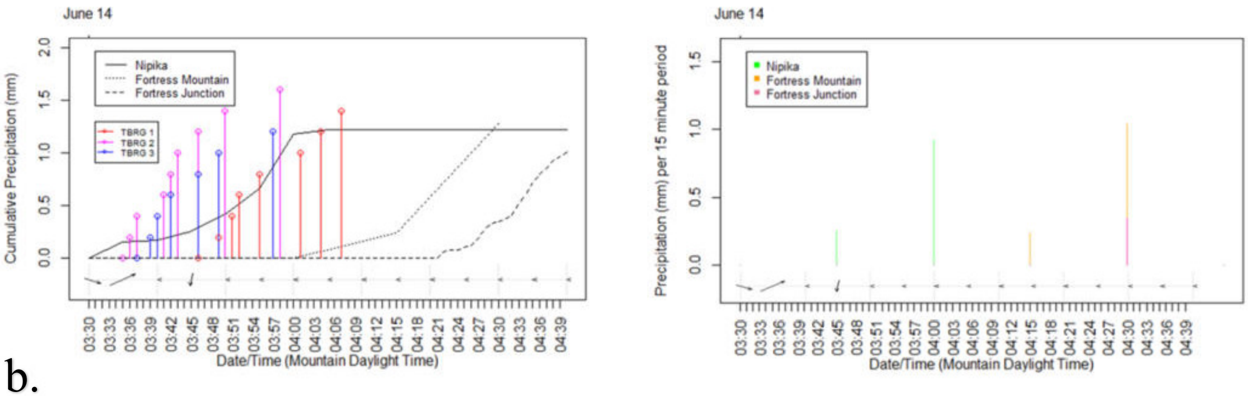
June 14
Cumulative Precipitation (mm)
Nipika
Fortress Mountain
Fortress Junction
TBRG 1
TBRG 2
TBRG 3
0.0
0.5
1.0
1.5
2.0
03:30 03:33 03:36 03:39 03:42 03:45 03:48 03:51 03:54 03:57 04:00 04:03 04:06 04:09 04:12 04:15 04:18 04:21 04:24 04:27 04:30 04:33 04:36 04:39
Date/Time (Mountain Daylight Time)
June 14
Precipitation (mm) per 15 minute period
Nipika
Fortress Mountain
Fortress Junction
0.0
0.5
1.0
1.5
03:30 03:33 03:36 03:39 03:42 03:45 03:48 03:51 03:54 03:57 04:00 04:03 04:06 04:09 04:12 04:15 04:18 04:21 04:24 04:27 04:30 04:33 04:36 04:39
Date/Time (Mountain Daylight Time)

b.

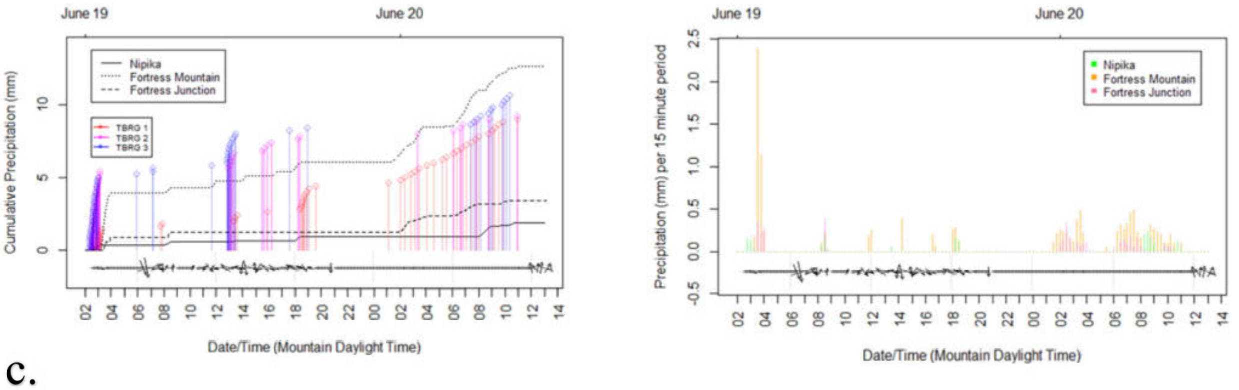
June 19
June 20
Cumulative Precipitation (mm)
Nipika
Fortress Mountain
Fortress Junction
TBRG 1
TBRG 2
TBRG 3
0
5
10
02 04 06 08 10 12 14 16 18 20 22 00 02 04 06 08 10 12 14
Date/Time (Mountain Daylight Time)
June 19
June 20
Precipitation (mm) per 15 minute period
Nipika
Fortress Mountain
Fortress Junction
-0.5
0.0
0.5
1.0
1.5
2.0
2.5
02 04 06 08 10 12 14 16 18 20 22 00 02 04 06 08 10 12 14
Date/Time (Mountain Daylight Time)

c.

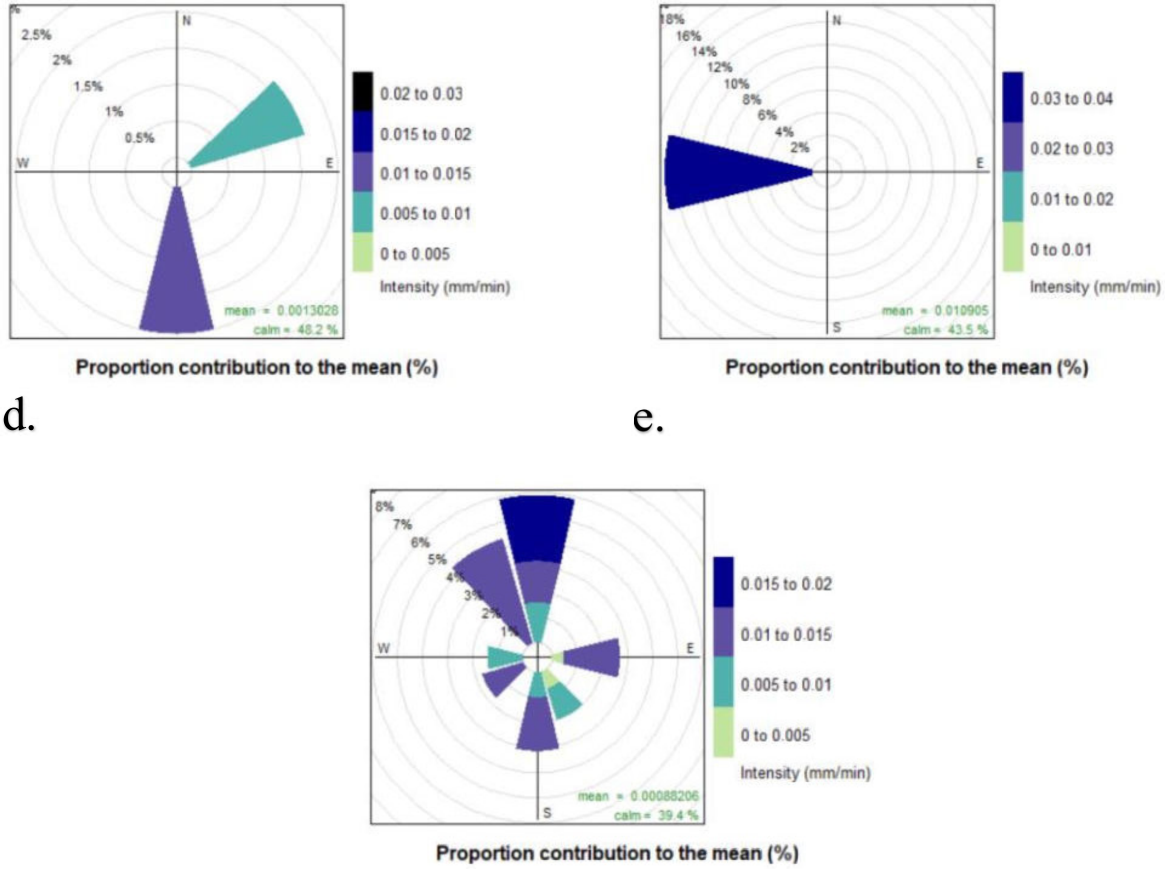

d.

e.

f.

Figure 4.36. SPADE precipitation events with noteworthy features relative to other precipitation events (a) Event 6 (22:45 MDT 23 May 2019 to 17:15 MDT 24 May 2019) was 18.5 hours long. Water vapour flux was from the east. This event was caused by local topographical effects. There was a strong correlation between elevation and precipitation during this event (b) Event 10 (4:10 MDT 14 June 2019 to 4:40 MDT 14 June 2019) lasted for 0.5 hours. My graphical analysis has been adjusted to include a period of time 40 minutes prior to the start of the official SPADE event. Water vapour flux was from the northwest. Event 10a exhibited a negative correlation between elevation and precipitation. (c) Event 12 (2:30 MDT 17 June 2019 to 13:40 MDT 17 June 2019) lasted 35 hours. Water vapour flux was downslope of the Canadian Rockies, before becoming parallel, and then strongly upslope. Event 12 exhibited a change in precipitation patterns. Precipitation roses for Event 6 (d), Event 10 (e), and Event 12 (f) are also included with wind values less than 0.5 m s^{-1} removed.

4.9.2 Wind-Precipitation Relationships at Meteorological Stations in the Study Region between 2011 and 2019

Average cumulative precipitation and average wind speed may sometimes have an inverse relationship on the eastern side of the Continental Divide with higher values of average cumulative precipitation being associated with lower wind speeds on this side of the Continental Divide (Figure 4.37). On the eastern side of the Continental Divide, 2017 had the lowest average cumulative precipitation and the highest wind speed (3.1 m s^{-1}). Although 2017 saw the lowest average cumulative precipitation as well on the western side of the Continental Divide, scalar wind speed was within the mid-range of values for the 2011 to 2019 period.

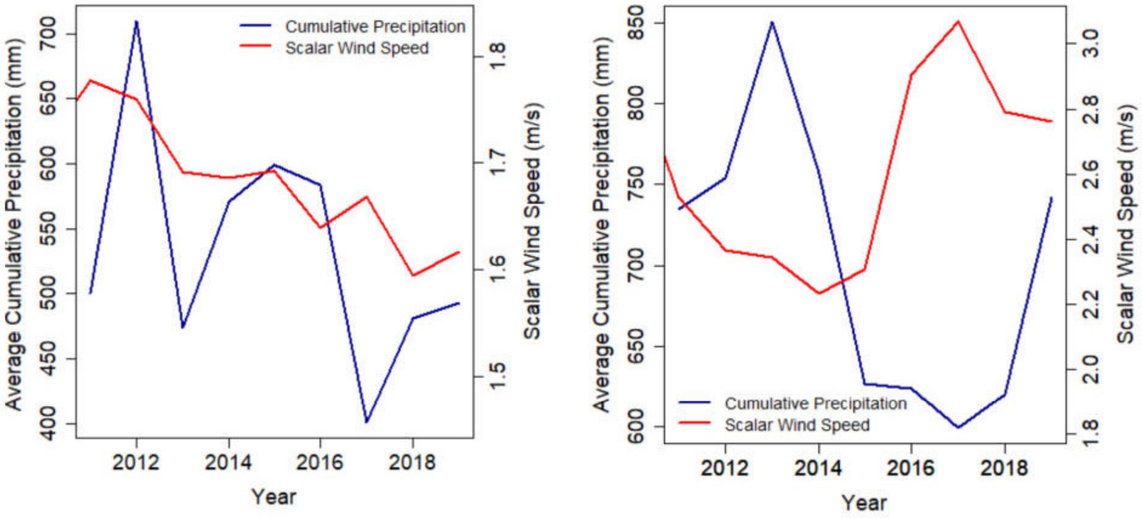

Figure 4.37. Average cumulative precipitation and average wind speed plotted across years for the western (Left) and eastern side (Right) of the Continental Divide.

Average cumulative precipitation showed distinct peaks and valleys on the western side of the Continental Divide, with 2012 having the highest average cumulative precipitation. Overall, cumulative precipitation values decreased slightly with time. Although wind speed exhibited some peaks and valleys in values from year to year, overall wind speed showed a decline in values from 2011 to 2019 with average wind speed decreasing by 0.14 m s^{-1} over this time period. Unlike the eastern side of the Continental Divide, the western side of the Continental Divide had comparatively high precipitation values in 2016, without a large peak in wind speeds. Lowest cumulative precipitation values occurred in 2017 in a similar pattern to that which was found on the eastern side of the Continental Divide. The highest cumulative precipitation values occurred in 2012 on the western side of the Continental Divide and in 2013 on the eastern side of the Continental Divide. Wind vectors pointed in a more westerly direction towards the end of the 2011 to 2019 period on the western side of the Continental Divide (Figure 4.38).

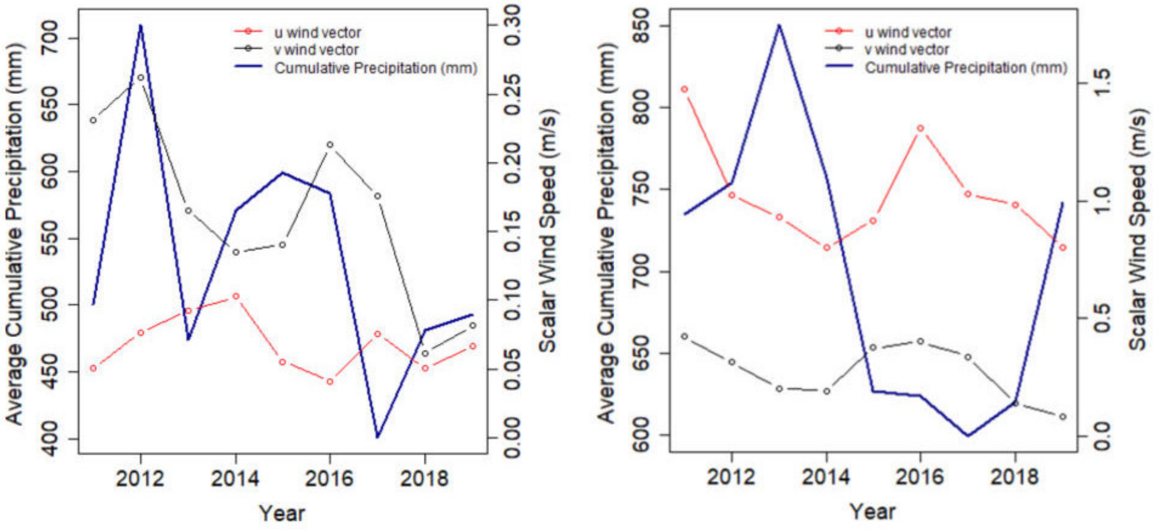

Figure 4.38. Mean annual u and v wind vectors and cumulative precipitation for all stations on the western (Left) and the eastern side (Right) of the Continental Divide between 2011 and 2019.

The v wind vector component decreased overall during this period. Wind vectors exhibited a more consistent direction on the eastern side of the Continental Divide in comparison to the western side of the Continental Divide. Years with relatively low cumulative precipitation on the eastern side of the Continental Divide were associated with a local maximum for u wind vectors on the eastern side of the Continental Divide. Average wind speed and direction varied slightly from year to year, but overall wind generally blew in a westerly direction on the eastern side of the Continental Divide and a south to southwesterly direction on the western side of the Continental Divide. During 2018 and 2019 there is a distinct westward shift in the average wind vectors.

Each side of the Continental Divide exhibited a very different scalar wind profile when average wind speed was plotted across each month of the year (Figure 4.39). The western side of the Continental Divide exhibited a relatively smooth profile with minimum values occurring during January and December and maximum values occurring during the Spring and Summer. The eastern side of the Continental Divide exhibited a relatively jagged wind speed profile with the lowest wind speeds occurring during the summer and early fall (July, August, and September), and relatively low wind speeds occurring during February (a local minimum).

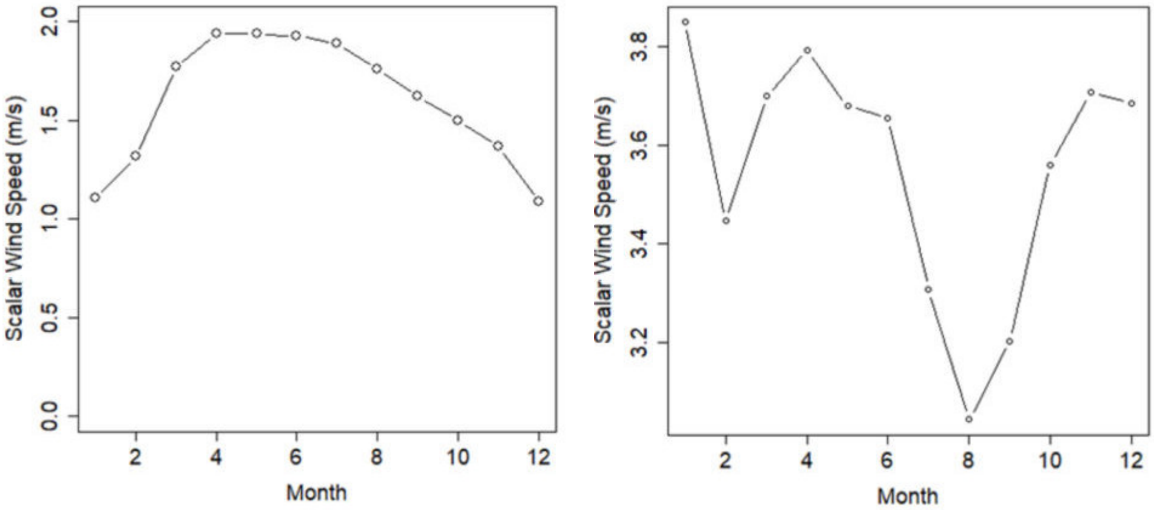

Figure 4.39. Mean scalar wind speeds for each month of the year for all stations on the western side (Left) and eastern side (Right) of the Continental Divide between 2011 and 2019.

Stations below 1446 m above sea level in elevation exhibited a small but significant decline in scalar wind values during the 2011 and 2019 period on the eastern side of the Continental Divide (Figure 4.40). All stations on the western side of the Continental Divide also had a linear decrease in average monthly scalar values except for one station that was located at the lowest elevation which exhibited an increase in scalar wind values that was statistically non-significant (Figure 4.41).

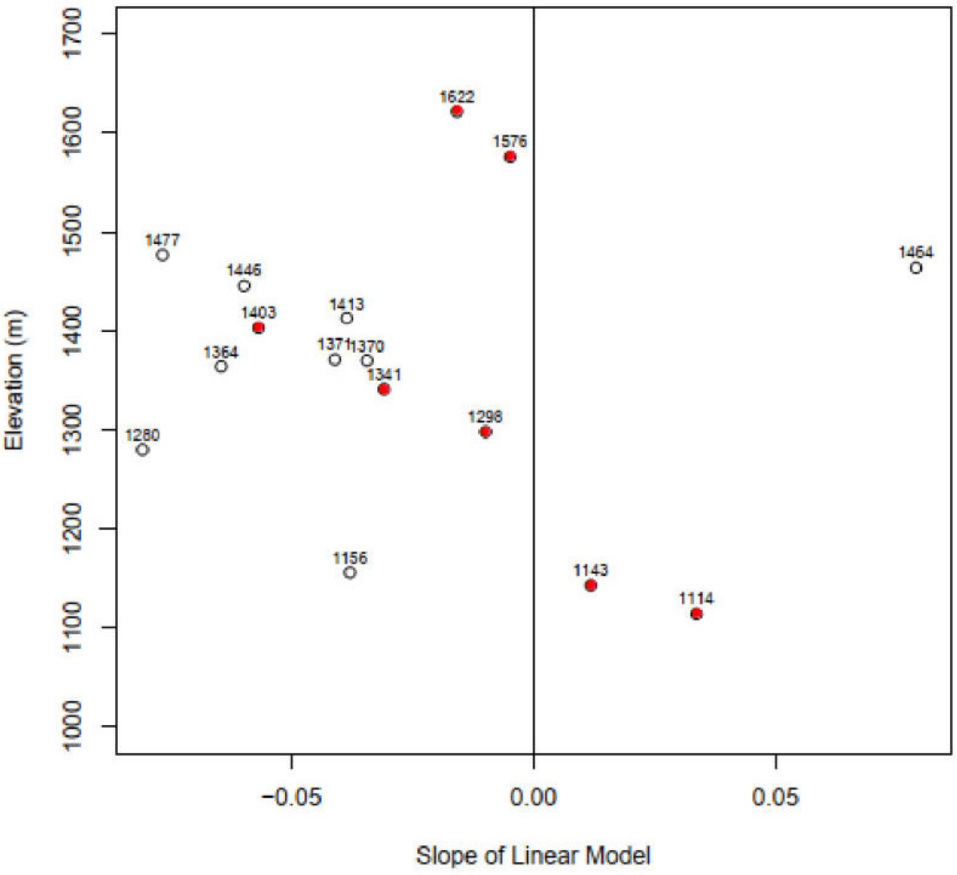

Figure 4.40. Slopes of linear models created from plots of daily average scalar wind speeds at stations on the eastern side of the Continental Divide between 2011 and 2019. Elevations (in metres above sea level) are listed above dots. Red dots indicate linear models that were not statistically significant. Positive (negative) values indicate that wind speed increased (decreased) between 2011 and 2019 according to a linear model. The two lowest elevation stations with positive values were located in the prairie. The higher elevation station with a positive value was located in a valley that is oriented in a north-south direction.

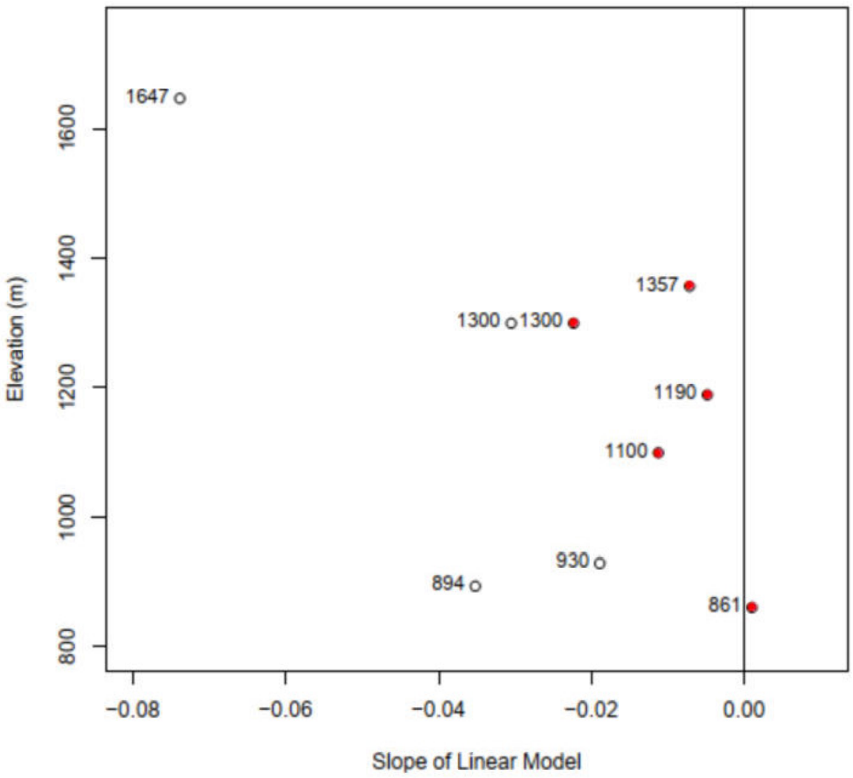

Figure 4.41. Slopes of linear models created from plots of daily average scalar wind speeds at stations on the eastern side and western side of the Continental Divide between 2011 and 2019. Elevations (in metres above sea level) are listed above dots. Red dots indicate linear models that were not statistically significant. Positive (negative) values indicate that wind speed increased (decreased) between 2011 and 2019 according to a linear model.

4.10 Diurnal Variability

The western side of the Continental Divide exhibited different diurnal precipitation patterns than the eastern side of the Continental Divide during the SPADE period (Figure 4.42). Low frequencies of precipitation occurred during the evening hours on the western side of the Continental Divide, and occurred more frequently during the first half of the day. This was verified using a Welch Two Sample t-test, with the first half of the 24-hour period exhibiting a significantly higher frequency of precipitation than the latter half of the day. Precipitation occurred more frequently during the afternoon hours on the eastern side of the Continental Divide, in comparison to the morning hours. This was also verified using a Welch Two Sample t-test, with the first half of the day exhibiting significantly less frequent precipitation than the latter half of the day. A consistently low frequency time for precipitation on the eastern side of the Continental Divide was between 5:00 and 6:00 MDT. When the SPADE period is divided into two month-long periods, precipitation patterns retained a similar diurnal pattern on each side of the Continental Divide. These were also statistically significant in a Welch Two Sample t-test. Precipitation was concentrated in different months for each side of the Continental Divide. The western side of the Continental Divide had a greater frequency of precipitation and greater total precipitation amounts during June. The eastern side of the Continental Divide had a greater frequency of precipitation and greater total precipitation amounts during May.

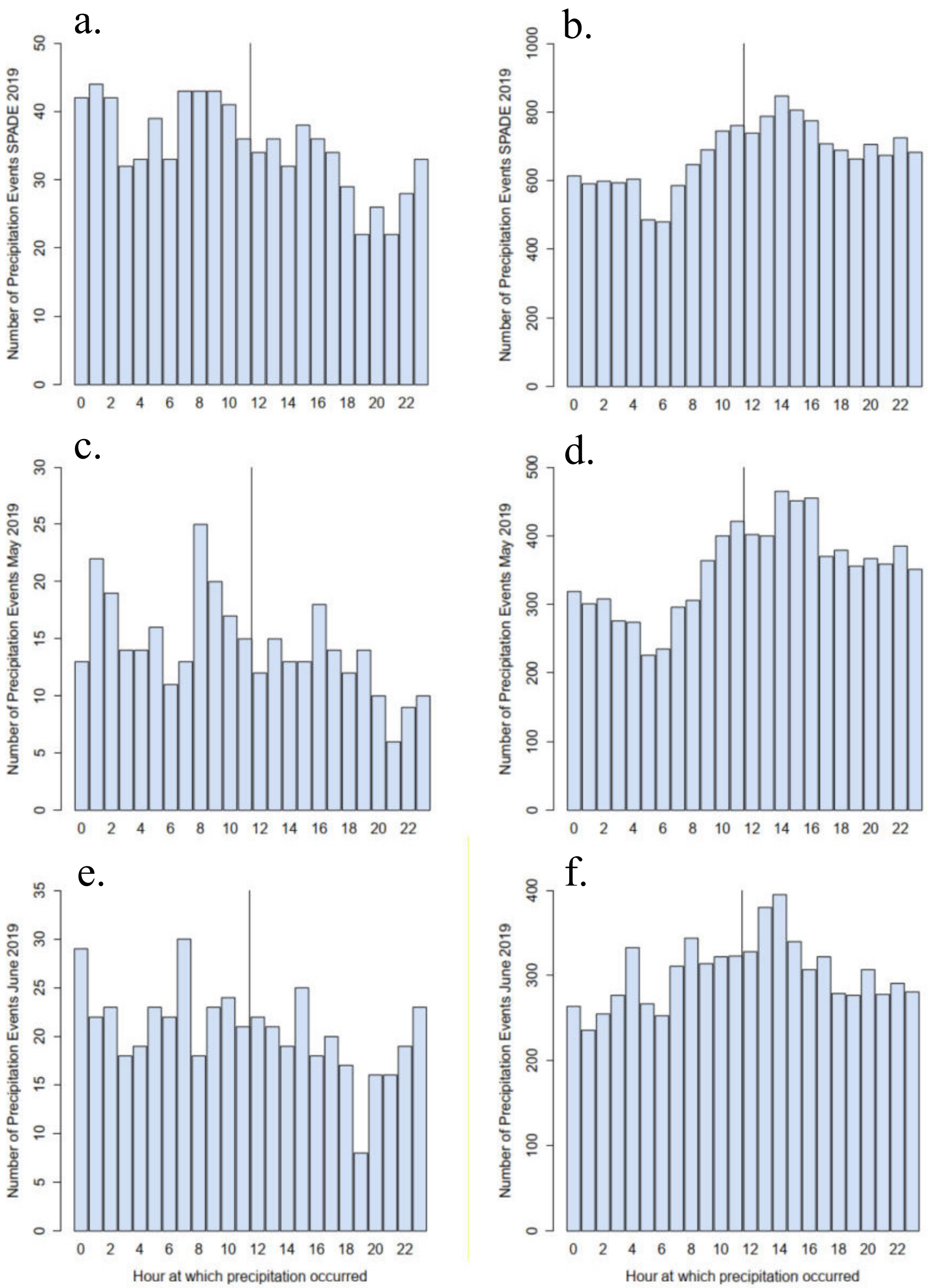

Figure 4.42. Precipitation frequency for precipitation amounts greater than 0.1 mm plotted against time of day (24-hour clock local time) on both sides of the Continental Divide during the SPADE period: (a) western side of the Continental Divide (total SPADE), (b) eastern side of the Continental Divide (total SPADE), (c) western side of the Continental Divide (May), (d) eastern side of the Continental Divide (May), (e) western side of the Continental Divide (June), (f) eastern side of the Continental Divide (June). (May: 26 April-26 May, 2019; June: 26 May-26 June 2019). These graphs contain data from FLNRORD and ACIS stations only.

Precipitation frequencies for precipitation greater than 0.1 mm increased in the eastern side of the study area as the day progressed (Figure 4.43).

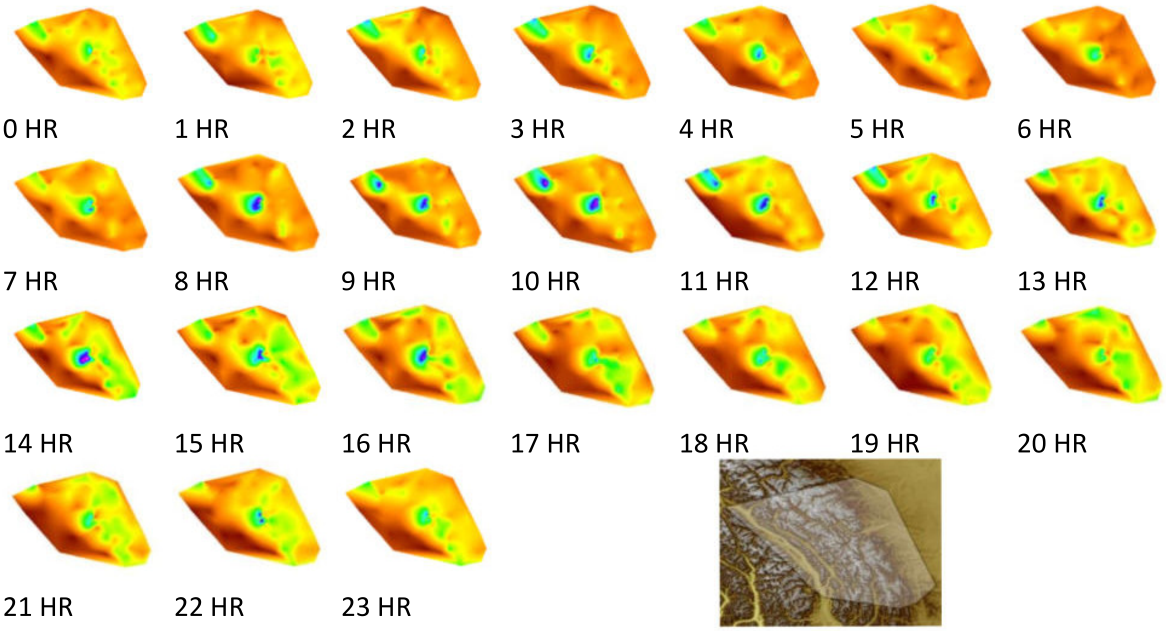

Figure 4.43. Precipitation frequency interpolated for precipitation amounts greater than 0.1 mm plotted across time in the study area during the 2019 SPADE campaign. Maximum and minimum values are relative to each hour to compare precipitation gradient shapes. An elevation plot is also included.

Chapter 5: Discussion

Relationships between precipitation gradients/patterns and elevation, cool and warm seasons, general wind patterns/storm trajectories, and inter-annual and intra-annual variability are examined and discussed in this chapter. Consequences of future climate change on this study area are discussed in relation to these findings. Finally, total cumulative annual precipitation for station data and ERA5-Land data are compared across the study period, and some potential reasons behind value divergence between these datasets are assessed. Potential limitations of this study are also discussed.

5.1 Research Questions

5.1.1 Relationships between Elevation and Precipitation Gradients (Precipitation/Elevation Ratios)

How does Elevation Influence Precipitation Gradients across the Continental Divide? Annual precipitation amounts have a positive and significant relationship when total accumulated precipitation data from both sides of the Continental Divide are pooled together (from 2011 to 2019) (Figure 4.17). When a linear model is developed from this pool, elevation explains about half of the variability ($R^2 = 0.51$) in total cumulative annual precipitation in our study area. Annual cumulative precipitation increases at a rate of 0.39 mm of precipitation per meter of elevation. An increase in cumulative precipitation with elevation only occurred on the eastern side of the Continental Divide, while annual cumulative precipitation did not increase with elevation on the western side of the Continental Divide (Figure 4.15). Total cumulative precipitation did increase with elevation on both sides of the Continental Divide for the 2019 SPADE field season. One feature that conflates this analysis is that the latter time period (2019 SPADE field season) had more stations available for analysis.

When annual cumulative precipitation data from both sides of the Continental Divide are pooled together, larger precipitation gradients or precipitation/elevation ratios (mm m^{-1}) occur at lower elevations than at mid-elevation sites (Figure 4.16). Precipitation/elevation ratios then remained somewhat constant up to elevations of about 2000 m above sea level, where these ratios increased. Annual precipitation/elevation patterns were similar when compared across years, but were distinctly different from those during the SPADE period. During this period, the precipitation/elevation ratio increased with elevation up to 2000 m, before decreasing (Figure 4.14).

The spring period, which coincides with much of the SPADE period, is associated with unstable air masses and a high lapse rate (Barry 2008; Shea et al. 2004), therefore, the differences in the shapes of the SPADE precipitation/elevation curves and the annual precipitation/elevation curves could be due to a proportionately larger amount of convective development confined within the valley during the SPADE period in comparison to the annual period. The 2015 to 2016 (El Niño) period had the lowest precipitation/elevation ratios on average for the SPADE period, with little change in precipitation/elevation ratios across elevations. This contrasted other SPADE periods, with distinct precipitation/elevation maxima at around 2000 m above sea level most of the time.

Annual precipitation curves had more precipitation at the lowest and highest elevations in comparison to the SPADE curves (Figure 4.15 in comparison to 4.9). Greater precipitation amounts at higher elevations may be due to low (Luce et al. 2013) to mid tropospheric westerly flow (Shea & Marshall 2007) during the winter in Pacific North America. Westerly flow is associated with greater amounts of orographic enhancement since it is perpendicular to the mountains (Luce et al. 2013). Summertime convection and increased low-elevation precipitation due to blocking from wintertime high pressure ridging patterns, in addition to other types of blocking patterns, could explain the larger precipitation/elevation ratio at lower elevations (Shea & Marshall 2007; Bohne et al. 2020). Low-level atmospheric blocking caused by anticyclonic conditions at any time of year could create a barrier between incoming precipitation and the topography, forcing precipitation upwind, or it may smooth topographical features diminishing orographic enhancement of precipitation, since orographic enhancement can be partially dependent upon orographic elevation gradients (Neiman et al. 2002; Barry 2008, p. 171; Ramelli et al. 2021). These features could have contributed to the relatively high amounts of precipitation at the lowest elevations. The coefficient of variation decreased with elevation, with the lowest coefficient of variation co-existing with some of the highest meteorological stations within the study area during the annual period (Figure 4.26). This could be indicative of atmospheric decoupling at lower elevations during certain periods of the year.

The eastern side of the Continental Divide has a comparatively large cumulative precipitation value spread in comparison to the western side of the Continental Divide during the 2019 SPADE period (Figure 4.7). This may be due to varied topography of this area. The strong positive precipitation/elevation relationship between about 1100 m above sea level and about 1400 m above sea level could be indicative of the transition from prairie sites to mountain sites on the eastern side of the Continental Divide. Precipitation values at elevations above 1500 m above sea level could be representative of higher elevation mountain sites. Another factor that could contribute to this precipitation spread is the prevalence of convective precipitation during summer on the eastern side of the Continental Divide (Barry 2008; Scaff et al. 2020), which could have occurred later during the SPADE period. Summertime convective precipitation does not exhibit a strong precipitation/elevation relationship in the Canadian Rockies (Shea et al. 2004; Shea & Marshall 2007).

According to existing literature, there is a strong positive precipitation/elevation relationship for precipitation events on the western side of the mountain ranges in western North America. This is due to interaction between moisture advection from the Pacific Ocean and orographic enhancement on mountain ranges oriented roughly perpendicular to the direction of this advection (Anders et al. 2007; Siler et al. 2013; Mass et al. 2015; Bohne et al. 2020). This relationship has also been identified in the Canadian Rockies, with the western side of the Canadian Rockies exhibiting a stronger precipitation/elevation relationship than the eastern side of the Canadian Rockies (Shea et al. 2004), but there is some evidence that a west-east rain shadow can develop under westerly flow regimes (Shea & Marshall 2007). Overall, the absence of a positive precipitation/elevation relationship on the western side of the Continental Divide in this study for the annual period (Figure 4.15) was unexpected in our study. Geographic areas with a negative precipitation/elevation relationship are rare in North America (Bohne et al. 2020).

The absence of a positive precipitation/elevation relationship on the western side of the Continental Divide during the annual period could be due to atmospheric blocking. In a study on orographic enhancement of precipitation in the western United States, precipitation amounts increased with elevation at most sites except for a couple of sites where low-level blocking was involved (Neiman et al. 2002; Bohne et al. 2020). When high pressure ridging or arctic air masses are impinging on the eastern side of the Continental Divide (such as Event 5 during the SPADE campaign), cooler air could be forced through mountain passes connected to the lowest elevation sites (such as Blaeberry and Brisco) on the western side of the Continental Divide. Uplift from cold air damming in these northwest-southeast valleys, could ensure that these locations receive more precipitation than higher elevation sites when moisture is being advected along the valley. Blocking could also force precipitation upwind of the Canadian Rockies (Neiman et al. 2002). This hypothesis is supported by the presence of a negative precipitation/elevation relationship on the western side of the Continental Divide during some time periods in which some of the westernmost sites received the largest amounts of precipitation. This negative precipitation/elevation relationship could be due in part to the station networks on the western side of the Continental Divide comprising of TBRGs which can underperform in cold conditions. This negative relationship may not be entirely due to the underperformance of TBRGs during cold conditions. Summer-time periods, which are ideal for TBRGs, exhibited a negative precipitation/elevation relationship as well.

The development of valley bottom inversions could also be implicated in the poor precipitation/elevation relationship above the valley. Inversions are indicative of atmospheric stability, which can limit orographic enhancement of precipitation by preventing air parcels from ascending mountains (Barry 2008). If a strong inversion layer persists, orographic enhancement may occur from the top of the inversion layer upwards since moisture could be trapped below the inversion. Arctic air masses could have also played a role in inhibiting the passage of storms over the Canadian Rockies, since they are prevalent on the prairies during the winter months (Cullen & Marshall 2011). The vertical extent of arctic air masses is expected to increase with climate change (Turner & Gyakum

2011). These air masses have already been identified at Lake Louise at 1600 m elevation in the interior of the Canadian Rockies (Cullen & Marshall 2011).

5.1.2 Relationships between Cool and Warm Seasons and Precipitation Gradients

Can Differences in Precipitation Gradients Be Detected between Cool and Warm Seasons? Precipitation gradients varied between cool and warm seasons. Precipitation/elevation relationships were weak during the winter on the western side of the Continental Divide, but across the study area precipitation/elevation relationships appeared to be the strongest during the winter with the greatest precipitation accumulation occurring along the Continental Divide (some of the highest elevation sites within the study area) and the lowest precipitation accumulation occurring at some of the lowest sites (Figures 4.29 and 4.30). This could be due to strong upper-level winds and northwesterly flow in winter months, which could advect moisture from the Pacific Ocean, coupled with high pressure ridging in the western part of the study area, which could re-direct storm tracks towards the Rockies (Shea & Marshall 2007). Perhaps in the presence of an inversion layer, orographic enhancement only occurred above the inversion. Also, orographic enhancement of snowfall means that precipitation maxima can occur at mountain crests during the winter (Mott et al. 2014). Meanwhile, during the summer, precipitation maxima occurred at some of the lower or mid-elevation sites. This could be due to diminished overall flow with increased cyclonic activity, and increased convective precipitation (Shea & Marshall 2007). Spring and fall patterns were hybrids of summer and winter precipitation patterns, with precipitation maxima situated near the Continental Divide, but with modest amounts of precipitation spread throughout the study region. Spring and fall precipitation patterns contain mixtures of winter and summer synoptic scale flow characteristics in the Canadian Rockies (Shea &

Marshall 2007). Interestingly, summer and winter precipitation amounts may have an inverse relationship according to graphical analysis, with less winter precipitation occurring during years with considerable summer-time precipitation (Figure 4.27).

Summer precipitation contours are less defined than winter contours, which could be indicative of greater variability in where precipitation was located over the years that were being examined (Figures 4.29 and 4.30). During the summer, enhanced convective activity could mean that precipitation occurs more erratically across the landscape. This might be due in part to the smaller size of convective storms. The linear components of summer precipitation contours could indicate larger amounts of precipitation migration in comparison to winter contours due to deeper warm layers during the summer months, since storms with high freezing levels can penetrate mountain ranges more easily (Foresti et al. 2018). During winter, precipitation contours are more clearly defined, they are circular in shape and focused on the highest elevation sites along the Continental Divide (likely near mountain peaks). These circular or bulls-eyed shaped precipitation contours could be congruent with snowfall maxima developing around topographical peaks due to seeder-feeder mechanisms (Mott et al. 2014). Future studies could determine if precipitation phase is implicated in the preferential accumulation of precipitation around the highest peaks (winter) or mid-elevation ridgelines or valleys (summer) and whether phase influences the ability of precipitation to migrate along topographical features.

Greater precipitation migration may occur during the summer because convective precipitation is enhanced by passage along mountain ridges, since convergence and ascent are maximized along the ridgetop during daytime heating (which also reduces the lee effect) (Barry 2008). In addition, higher freezing levels could have allowed areas of higher precipitation growth to penetrate further into the mountain range east of the Continental Divide and migrate into the prairies during the summer months (Foresti et al. 2018). Warm, deep layers of moisture and upward air motion can facilitate the transportation of precipitation across mountain barriers such as the Continental Divide (Thériault et al. 2022). Conversely, synoptic scale systems with low freezing levels, like many systems during winter, are more strongly impacted by orography and are blocked more effectively by mountain barriers (Foresti et al. 2018). Additionally, low scalar wind speeds during the latter part of summer on the eastern side of the Continental Divide could limit the frequency of upslope storms, which have a tendency of migrating westward (Figure 4.39). Precipitation maxima appeared to migrate eastward as the spring and summer seasons progress (Figures 4.29 and 4.30). During the spring season, precipitation maxima were located close to the Continental Divide. Subsequently, precipitation maxima were located above the easternmost Canadian Rockies and the Foothills during July, and then may have migrated even slightly further east during August when few precipitation maxima existed near the Continental Divide. These findings are consistent with greater diurnal heating and lee-side convergence and enhanced precipitation layer growth (Barry 2008; Thériault et al. 2022). Large precipitation events in the spring and early summer were associated with easterly flow during the SPADE campaign, which could create precipitation maxima near the Continental Divide due to orographic enhancement (Thériault et al. 2022). The switch from larger precipitation frequencies and amounts on the eastern side of the Continental Divide during May to larger frequencies and amounts of precipitation on the western side of the Continental Divide during June could be indicative of a transition from a more easterly flow regime to a more westerly flow regime.

The difference between the spring period, and time-frames later in the warm season may also be due in part to lower planetary boundary layer height that coincides with the spring period so the eastward propagation of convective precipitation could be more constrained by the Continental Divide or other topographical barriers such as mountain valleys during this period (Allabakash & Lim 2020). An additional constraint to eastward passage of storms is the stronger easterly flow that often occurs at this time of the year (Shea & Marshall 2007). Therefore, convective precipitation could have a strong positive precipitation/elevation relationship during the spring period, since many small convective storms are confined to mountain valleys on the western side of the Continental Divide, or migrate towards the Continental Divide from the east. Conversely, the precipitation/elevation relationship could be weakened during the summer months due to the eastward propagation of precipitation across lower elevation sites in the prairies in response to prevailing westerlies, a deeper precipitation layer, and an increasingly high convective boundary layer. Diurnal precipitation development during the SPADE period demonstrates elements of this convective migration (Figure 4.43).

According to graphical analysis, precipitation is limited on the western side of the Continental Divide during the summer (Figures 4.29 and 4.30). Evaporative loss of precipitation could be significant at stations on the western side of the Continental Divide. Precipitation was recorded most frequently at sites on the western side of the Continental Divide in cooler periods during the early morning hours of the 2019 SPADE campaign, and relatively little precipitation was recorded during convective events without synoptic forcing at Nipika (Thériault et al. 2022). Precipitation evaporated before it reached the ground on several occasions at this site, with instances of virga identified by both human observers and

Micro Rain Radar. Conversely, precipitation occurred more frequently during warmer periods of the day on the eastern side of the Continental Divide. During the SPADE campaign fast falling hydrometeors and a large condensate flux from the east side of the Continental Divide were necessary for precipitation to occur on both sides of the Continental Divide simultaneously (Thériault et al. 2022). A true comparison of evaporation on both sides of the Continental Divide may not be possible, since the lower mean elevation of stations on the western side could mean that greater amounts of precipitation is evaporating at these stations. Synoptic scale events recorded much larger amounts of precipitation at the valley bottom at Nipika in comparison to convective events. This may be due in part to the smaller temporal and spatial extent of convective storms at this location. These smaller storms may not be large enough to dampen the pervasive valley circulations, which could transport moisture from the valley floor (Figure 5.1). Additionally, synoptic scale events may create deep precipitation layers (Thériault et al. 2022). Future studies could determine if the evaporation of precipitation during convective events at sites similar to Nipika, enables greater amounts of water vapour to traverse the Continental Divide. If precipitation evaporates several thousand metres above the ground it is possible that moisture could be more readily advected over the Continental Divide, which ranges from 1130 to 3600 m in elevation. Virga above Nipika during both synoptic and convective events indicates that precipitation is evaporating upwards of several thousand metres above this site. There are some indications that large precipitation events are increasing in areas east of the Canadian Rockies (US Global Change Research Program 2017). Precipitation/elevation relationships or precipitation gradients were not examined directly, but the large difference in precipitation patterns across the same spatial domain between seasons demonstrates that warm and cold seasons exhibit distinct suites of precipitation gradients.

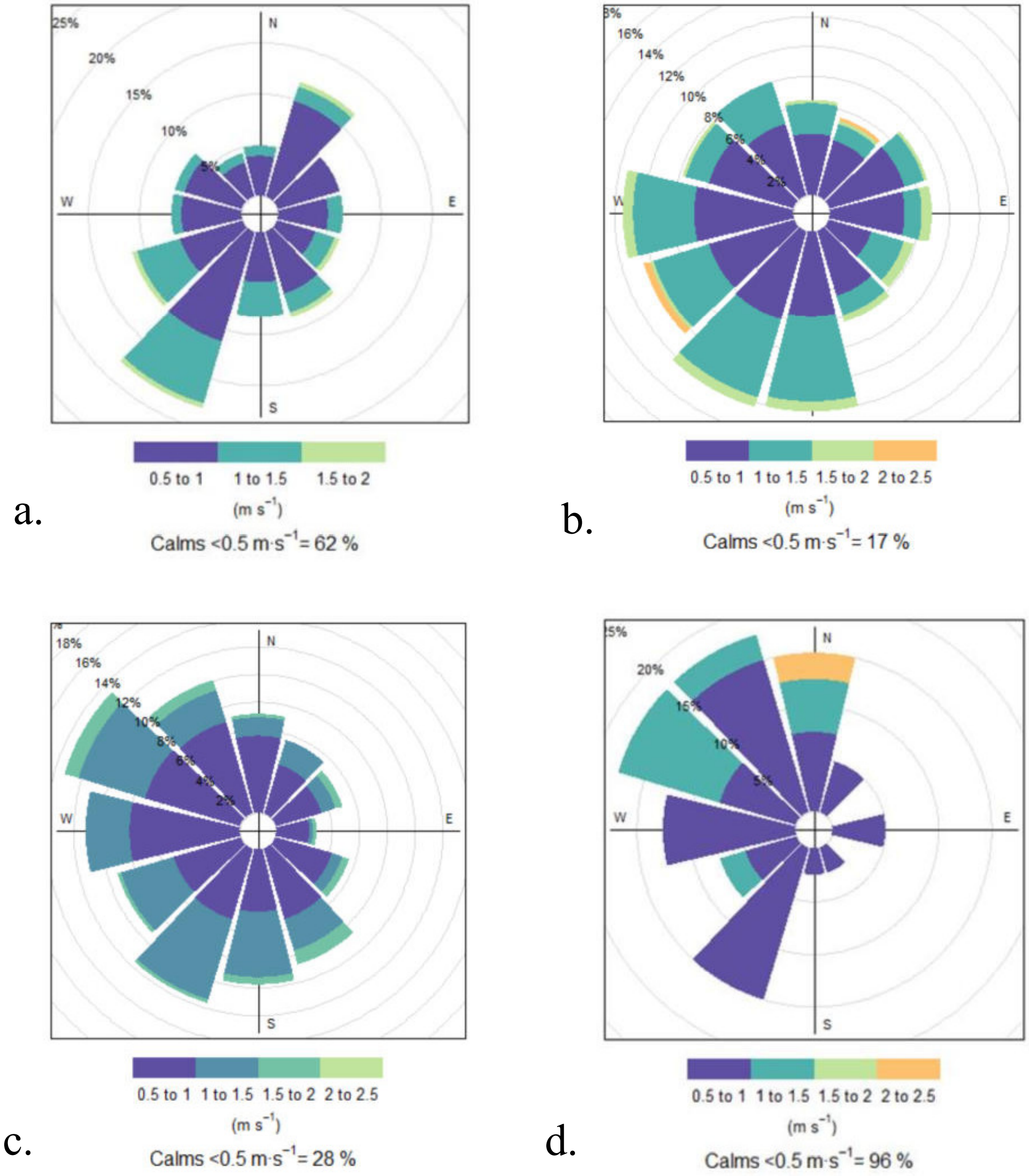

Figure 5.1. Wind patterns vary throughout a twelve-hour period of daylight at Nipika (26 May to 26 June 2019). a) During the morning (8:00 to 10:00 MDT) the wind profile had a prominent southwesterly component b) During the middle of the day (10:00 to 14:00 MDT) the wind profile had a prominent southerly component and a prominent westerly component. c) During the evening (14:00 to 20:00 MDT) the wind profile had a prominent northwesterly component. d) There was very little wind at night (12:00 to 04:00 MDT), but winds were most frequently from the northwest, with the strongest winds from the north.

5.1.3 Inter-annual and Intra-annual Variability in Precipitation Gradients

What is Inter-annual and Intra-annual Variability in Precipitation Gradients in this Region? Overall, 2013 exhibited the largest annual precipitation accumulation, specifically on the eastern side of the Continental Divide. This could be attributed in part to the 2013 Alberta flooding event. Inter-annual variations in cumulative precipitation predictors were identified. For the 2011 to 2014 SPADE period, longitude was identified as the best predictor (out of longitude, latitude, and elevation) for cumulative precipitation accumulation. However, elevation was the best predictor for cumulative precipitation for the 2015 to 2019 SPADE period. Elevation remained the strongest predictor for cumulative precipitation for all years for the annual period (Tables 4.2 and 4.3) when 60 stations were examined across all SPADE time-frames. Conversely, when 91 stations were examined across the 2019 SPADE period, longitude was the strongest predictor (Table 4.1). The emergence of longitude as a predictor with a higher resolution grid could be due in part to the tightly clustered spatial patterns of the additional stations (these stations mostly belonged to the Changing Cold Regions Network).

The change in predictors of SPADE period cumulative precipitation from longitude to elevation between the 2011 to 2014 period and the 2015 to 2019 periods could be indicative of a decrease in convective activity, since convective storms can create high density precipitation events at a specific location regardless of elevation (like Event 10 during the 2019 SPADE campaign) (Marshall & Shea 2007); they may also facilitate greater orographic enhancement of upslope storms, which can create strong localized precipitation gradients (like Event 13). The increased power of elevation as a predictor could also be a result of atmospheric decoupling with lower elevation sites having different precipitation regimes than higher elevation sites. The lower coefficient of variation with increasing elevation during the 2011 to 2019 period could demonstrate the presence of this phenomenon.

Cumulative precipitation amounts varied at specific elevations on either side of the Continental Divide. More precipitation fell per meter of elevation on the western side of the Continental Divide in comparison to the east side of the Continental Divide during 2012 and for all years encompassing 2015 to 2018 (Figure 4.25). More precipitation fell per meter of elevation on the east side of the Continental Divide in comparison to the western side of the Continental Divide for 2011, 2013, 2014, and 2019. Since the Pacific Ocean is a source of water vapour for the Canadian Rockies, particularly during the winter (Moran et al. 2007; Sinclair & Marshall 2009), differences in precipitation per meter of elevation on either side of the Continental Divide could be indicative of differences in moisture advection over the Continental Divide.

Convective precipitation near the Continental Divide has a propensity to move eastward (Barry 2008; Wallace & Minder 2021). In addition to westerly flow, the topography of the Canadian Rockies may be responsible for convection propagating eastward (Barry 2008). Peaks on a topographical plain that is sloped upward are good sites for generating convective precipitation when stream-lines converge behind the peaks (Cosma et al. 2002). This type of surface-atmosphere interaction may occur along the Continental Divide, since the uplift over a mountain range can be characterized as a wedge lift, except over large valleys (Barry 2008). Warmth generated along the upward slanted plain creates vertical uplift after the air parcel has moved beyond it (Cosma et al. 2002; Barry 2008).

Intra-annual variation can be considerable in the Canadian Rockies with each precipitation event producing large differences in precipitation across the study area (Figures 4.2 and 4.3). Precipitation amounts varied considerably between the 2019 SPADE events at each site. Nipika received < 1 mm of precipitation during one event (Event 11), and around 20 mm during another (Event 13). In most years, summer was the season that averaged the most precipitation per day, followed by spring, fall, and then winter (Figures 4.27 and 4.28; Table 5.1). The SPADE period averaged the most precipitation per day. The 2019 SPADE period had slightly less precipitation than average at 2.81 mm day^{-1}.

Table 5.1. Mean daily precipitation for each seasonal period in this thesis in millimetres (mm). Winter has been examined across different time periods.

Mean Daily Precipitation in millimetres (mm/day)						
Winter 1 (Jan.-Feb.)	Spring (Mar.-May)	Summer (Jun.-Aug.)	Fall (Sept.-Oct.)	Winter 2 (Nov.-Dec.)	Winter (Nov.-Feb.)	SPADE (May-Jun.)
0.99	1.92	2.47	1.80	1.26	1.12	3.11

5.1.4. General Wind Patterns/Storm Trajectories and Precipitation Gradients

How do General Wind Patterns/Storm Trajectories Affect Precipitation Gradients? Wind patterns shifted on the western side of the Continental Divide during the 2011 to 2019 period, with southerly wind vectors decreasing in magnitude (Figure 4.38). In part, this could be indicative of an increased build-up of high pressure on the eastern side of the Canadian Rockies due to an increased positive Pacific North American anomaly pattern, since this range is oriented in a northwest-southeast direction with mountain valleys running perpendicular to the axis of the range (Yu & Zwiers 2007). Additionally, arctic air masses that are prevalent east of the Canadian Rockies could be increasing in thickness as a consequence of climate change and could form a greater impediment to southerly winds (Turner & Gyakum 2011). Alternatively, decreased southerly flow could be indicative of a strengthening of northerly regional flow. Mid-tropospheric westerlies are declining in the Pacific Northwest of the United States (Luce et al. 2013), and this could manifest as decreased southerly flow in the Canadian Rockies given the valley geometry.

Large precipitation events at Nipika were often associated with a large component of low velocity winds with a southerly wind component (Figures 4.34 and 5.2; and Appendix G).

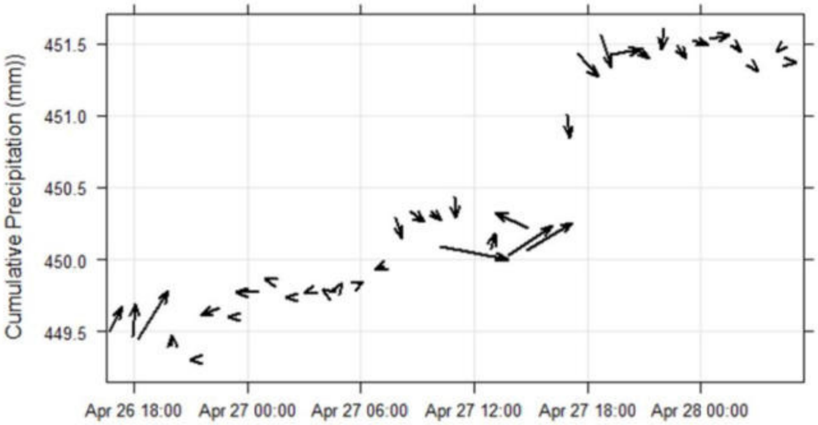

Figure 5.2. Cumulative precipitation plotted using hourly wind vectors for Event 1 at Nipika. A southwesterly wind vector was associated with increased cumulative precipitation.

This valley has a southwest orientation, so low velocity winds oriented in this direction may allow moisture advection into the valley. Conversely, strong valley wind might facilitate the development of valley circulations that could transport moisture out of the valley bottom, or the drying of the valley bottom due to the elimination of a thermal boundary between the atmosphere and the valley. This may have occurred during Event 11 (Figure D.11), which had relatively high wind velocities and negligible precipitation at Nipika). Gentle southwesterly winds in the presence of valley clouds, may allow moisture to be advected into the valley in an up-valley direction, increasing relative humidity, while cloud cover dampens valley circulation patterns caused by incoming solar radiation.

High magnitude precipitation events on the western side of the Continental Divide could be associated with strong southerly synoptic-scale flow as supported by other studies (Shea & Marshall 2007). In our study, years with large precipitation accumulations on the western side of the Continental Divide can be associated with a relatively strong southerly wind vector paired with a relatively weak westerly vector, which could be associated with blocking or meridional flow, in comparison to other years (Figure 4.38); but this relationship remains to be tested. This may be due to the northwest-southeast orientation of the mountain range, with weak westerlies allowing more precipitation to remain on the western side of the Continental Divide. This pattern may occur more frequently due to the trend of decreasing mid-tropospheric westerlies, which are further reduced by large scale modes of climate variability such as ENSO, the PDO, and the PNA pattern (Luce et al. 2013).

Overall, the southerly vector decreased across the 2011-2019 time-period and general precipitation decreased across this time period on the western side of the Continental Divide (but the relationship was not linear). The scalar wind speed also decreased on the western side of the Continental Divide during the 2011 to 2019 period (Figure 4.37). The decrease in precipitation over this period could be due to the reliance upon advection of moisture up the northwest-southeast valleys on the western side (Pacific side) of the Continental Divide. This is one of the dominant mechanisms for moisture transportation into the region, particularly during winter (Stewart et al. 1995; Shea & Marshall 2007).

Wind vectors changed direction throughout the 2011-2019 period on the western side of the Continental Divide, but had a relatively constant direction on the eastern side of the Continental Divide (Figure 4.38). Wind vectors had a larger magnitude during the 2015 to 2017 period on the eastern side of the Continental Divide, but less precipitation on this side than during other years. Fewer storms may have moved through this area during this time, and strong regional flow may have been oriented differently (Siler et al. 2013). Increased anticyclonic activity may have enhanced atmospheric stability during this period may have forced wind down the lee side of the Canadian Rockies and through valleys at lower elevations where most meteorological stations were located (Barry 2008). Additionally, forced lower level divergence around these mountain barriers could have facilitated some subsidence (Barry 2008). Increased stability could have facilitated smaller amplitude gravity waves, which impacted the ground more frequently, or gravity wave trains oriented in a downward direction. Foehn winds without precipitation on the western side of the Canadian Rockies could have developed due to anticyclonic damming of cold air (Barry 2008). In addition, anticyclonic conditions are also good precursors for katabatic winds. Comparatively high atmospheric pressure during the winters of 2015 and 2016 according to ERA5-Land data, and relatively clear skies, and high stability could be conducive to katabatic winds (Figure 5.3). The 2015 to 2017 period was warmer as well. In addition to changes in regional flow, large-scale warming could due to adiabatic processes as air is advected over a cold air dam, or warm Pacific air displaces a cold air pool on the lower east slopes of the Canadian Rockies as it crosses them (Barry 2008).

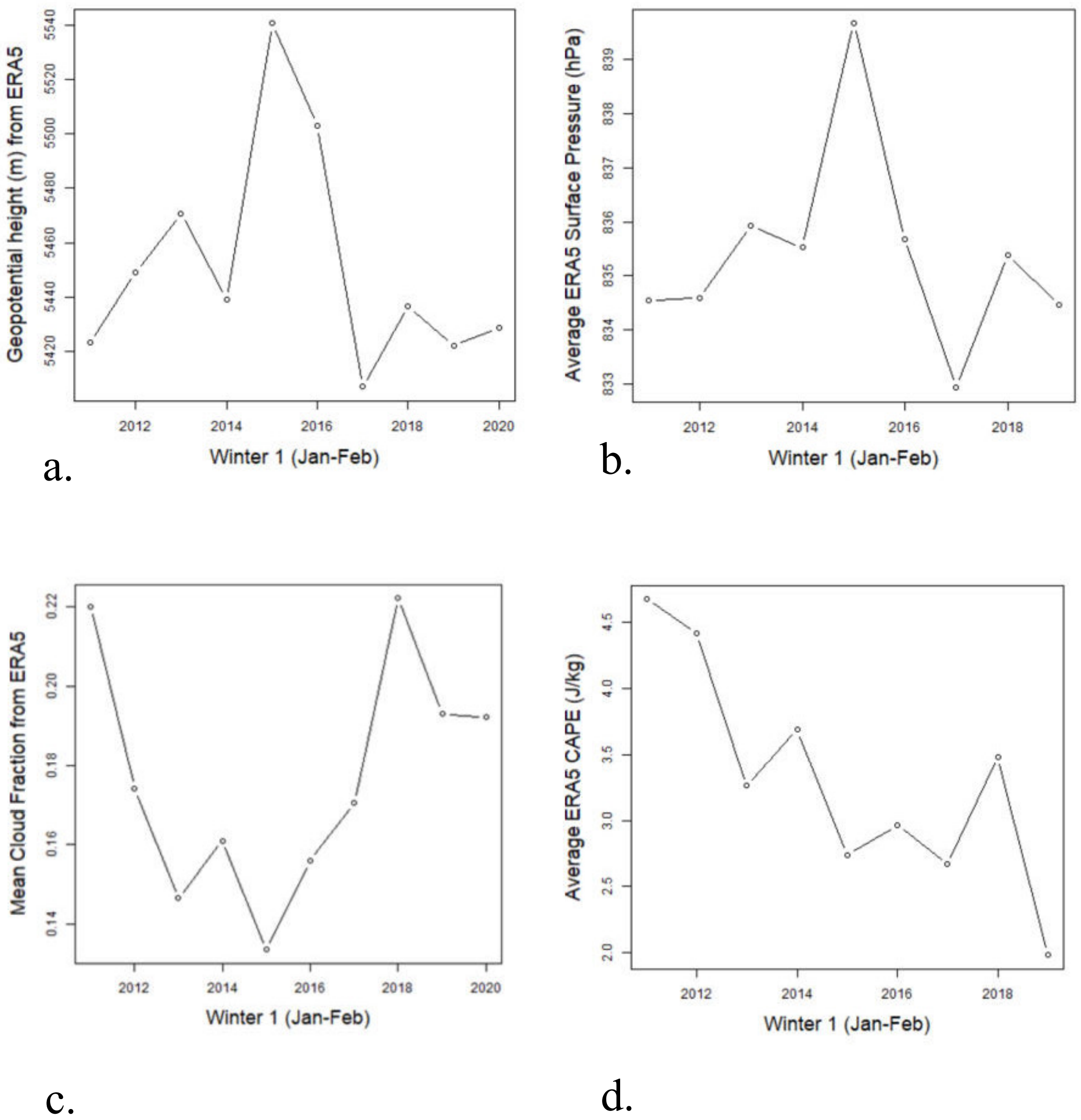

Figure 5.3. An examination of stability for January to February winter period from 2011 to 2019. (a) Mean geopotential heights (m) at 500 hPa from ERA5 during the Winter 1 (Jan-Feb.) period. (b) Mean surface pressure during the Winter 1 (Jan-Feb.) period. (c) Mean cloud fraction from ERA5 during the Winter 1 (Jan-Feb.) period. (d) Average ERA5 CAPE values for the Winter 1 (Jan-Feb.) period.

Other studies demonstrated that there is decreased orographic enhancement of precipitation during El Niño events in the Cascade Mountains, but theorized that this could be due to the increased southerly direction of the storm-track over a north-south oriented mountain range (Siler et al. 2013), or increased southerly direction of flow (Mass et al. 2015). During the

2014 to 2016 El Niño period the increased southwesterly wind vector magnitude on the eastern side of the Continental Divide, oriented perpendicular to the Canadian Rockies, should have led to increased orographic enhancement of precipitation due to increased uplift (Colle 2004). However, mountains of a similar elevation to the Canadian Rockies are considerable obstacles for both air flow and weather systems (Barry 2008). Increased stability may mean that less moisture is advected across the Continental Divide due to the inability of an incoming airmass to surmount the barrier, and the increased propensity of wind to be forced around the barrier (Barry 2008). Increased stability may have enhanced the Continental Divide's capacity to block moisture (Figure 5.3).

The flattening of the longitudinal precipitation profile on the eastern side of the study area during the 2015 to 2016 SPADE period (Figures 4.7 and 4.8), and the comparatively large precipitation/elevation ratio on the western side of the study area, could be due to decreased orographic enhancement during storms which might impede the storm's ability to surmount the Continental Divide. Decreased mountain wave development increased southerly flow during El Niño events, and weakened zonal winds, could decrease the passage of precipitation across the Canadian Rockies (Siler et al. 2016). In this scenario, southerly flow coupled with adiabatic warming could explain some of the annual temperature increases that occurred during the El Niño period (Barry 2008; Siler et al. 2013).

Low scalar wind speeds on the eastern side of the Continental Divide occur in both February and August while the lowest wind speeds on the western side of the Continental Divide occur during the winter months (Figure 4.39). This decrease in scalar wind speeds on the eastern side of the Continental Divide may be due to the preferential formation of areas of high pressure on the eastern side of the Continental Divide during these months (February and August). Increased atmospheric stability at lower elevations may be due to the passage of arctic air masses during February, and the development of summer high pressure systems during August. The lower wind speeds that occur on the western side of the Continental Divide during the winter could be due to lower amounts of valley heating, and greater amounts of atmospheric stability due to inversions, since these stations occur at lower elevations than stations on the eastern side of the Continental Divide on average.

The in-phase sea surface temperature anomaly harmonization of the ENSO and the PDO, which were both in the positive phase during 2014 to 2016 period and during the summer of 2017 (Figure 5.4), creates stationary waves which facilitate positive PNA-like anomaly structures (Yu & Zwiers 2007), such as a high pressure ridge above northwestern North America and a storm track located further to the south. This type of high pressure ridging is associated with stronger split flow, and low orographic precipitation gradients, and low mean precipitation values in the western United States and could have similar manifestations in western Canada (Bohne et al. 2020). Trends towards decreasing wind speeds on both sides of the Continental Divide during the 2011 to 2019 could be indicative of increasing atmospheric stability (Figures 4.40 and 4.41).

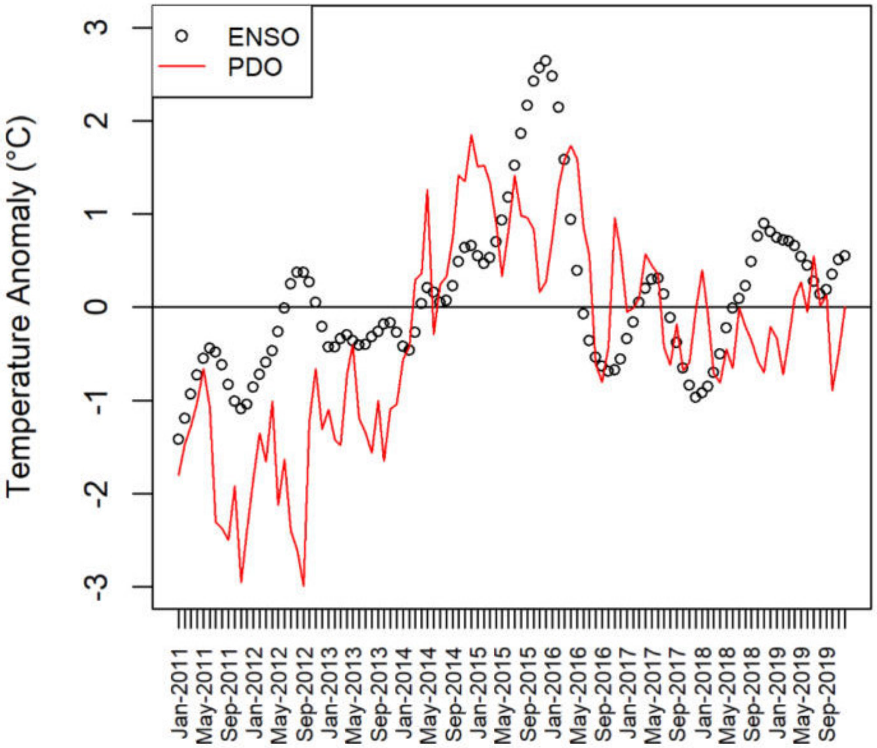

Figure 5.4. Temperature anomalies for El Niño-Southern Oscillation (ENSO) and Pacific Decadal Oscillation (PDO) ocean temperature indices in degrees Celsius. These temperature anomaly patterns are in phase and positive when both indices are above the 0°C anomaly line.

Interestingly, the positive PNA structure was sometimes coincident with the presence of "the Blob", anomalously warm sea temperatures near the coast of North America. Future studies could examine how local Pacific Ocean temperatures affect high pressure ridging in the Canadian Rockies, in addition to feedback mechanisms where precipitation and snow melt in the Canadian Rockies impacts local Pacific Ocean temperature regimes.

Evidence of atmospheric blocking may be found during the summer of 2017, which had low precipitation amounts and high temperatures relative to other summers and comparatively high geopotential heights in comparison to other summers (Figures 4.27, 4.28 and 5.5).

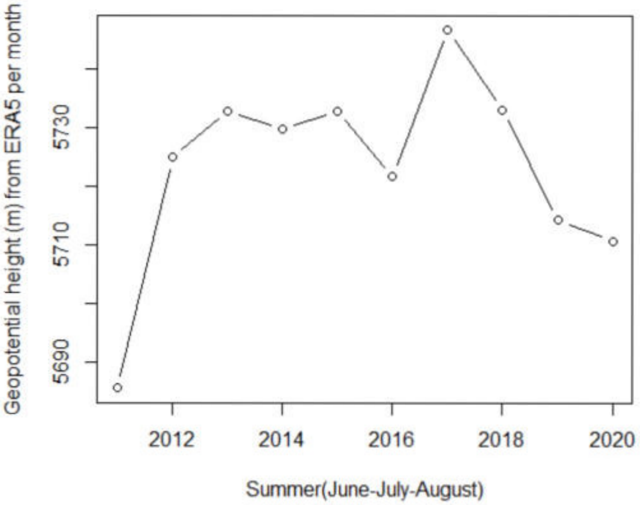

Figure 5.5. Geopotential height (m) derived from ERA5 data at the 500 hPa pressure level for the summer months (June, July, and August).

Some sites did not receive any precipitation for an extended period of time during this summer. This type of blocking of mid-latitude cyclones by a positive pressure anomaly in western Canada is associated with high magnitude wildfire seasons, and is caused by a positive phase in the PNA pattern due to anomalous Pacific Ocean temperatures (Johnson & Wowchuk 1993). There could be a strengthening of the positive phase of the PNA pattern for parts of our study period. Perhaps the large wildfire seasons in BC during 2017 and 2018 were a consequence of the positive phase of the Pacific North American Pattern. A study by Rood et al. (2005) determined that a half century oscillation in streamflow existed in Alberta, where periods of warm water off the Pacific Coast could cause reduced precipitation and increased evaporation. They predicted that this slow oscillation of Pacific sea surface temperatures may facilitate a warm and dry phase by the 2020’s that would exacerbate existing streamflow decline (Rood et al. 2005).

5.2 Potential Links Between this Study and Future Climate Change

Anthropogenic climate change is expected to decrease snow cover and soil moisture within the Canadian Rockies (Wallace & Minder 2021). Subsequently, decreased snow cover is expected to change characteristics of convective precipitation formation within this mountain range (Wallace & Minder 2021). Differences in temperatures between snow covered ground and snow free ground can affect the lapse rate in the atmosphere in a mountain valley, and the spatial and temporal location of snowmelt can determine where steep lapse rates occur, particularly during high pressure systems with large-scale subsidence (Barry 2008). The altered land surface is expected to change convective precipitation rates by increasing daytime upslope flows, facilitating greater moisture convergence over high terrain (Wallace & Minder 2021). Anthropogenic climate change is expected to increase frequency of convective precipitation during synoptically weak days in the spring period (Wallace & Minder 2021). However, convective precipitation characteristics may be different than predicted during the summer period because soil moisture may become depleted (Wallace & Minder 2021). During 2017, the year with the highest mean summer temperature and some very high spring temperatures, there were large amounts of spring precipitation, but little summer precipitation, and the strongest precipitation/elevation relationships were restricted to the high elevations during this year within the SPADE domain (Figures 4.17, 4.24 and 5.6). This could represent a deviation from the normal regime. Alterations to the summer convective precipitation regime could have substantial implications for annual precipitation amounts, since the highest mean daily precipitation often occurs during summer (Shea & Marshall 2007).

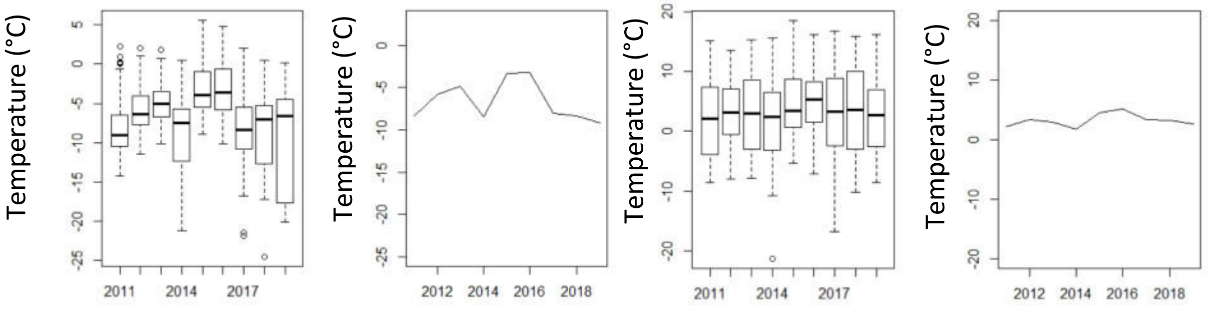

a.

Winter 1

b.

Spring

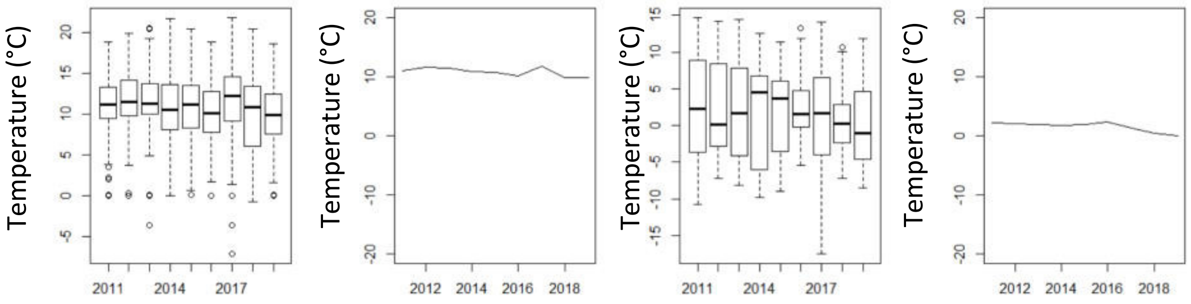

c.

Summer

d.

Fall

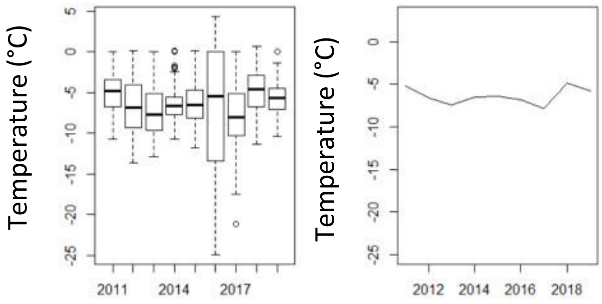

e.

Winter 2

Figure 5.6. Box plots for temperatures plotted across years beside average temperatures plotted across years from station data taken from any stations with temperature data on both sides of the Continental Divide including stations from ACIS, CCRN, and FLNRORD networks. (a) Temperatures during Winter 1 (January and February). (b) Temperatures during Spring (March, April, and May). (c) Temperatures during Summer (June, July, and August). (d) Temperatures during Fall (September and October). (e) Temperatures during Winter 2 (November and December).

Although larger synoptic scale features are likely responsible for generating most of the precipitation during the SPADE period (Thériault et al. 2022), convective processes could enhance precipitation amounts by increasing orographic enhancement (e.g. Event 9 in Thériault et al. 2022). Additionally, valley flows and anabatic flows could force moisture to vent above neighbouring ridgelines (De Wekker et al. 2004). The increased proportion of precipitation per unit of elevation on the western side of the Continental Divide in comparison to the eastern side of the Continental Divide during the 2014 to 2016 period could be due in part to decreased amounts of precipitation moving across the Continental Divide (Figure 4.25). Diminished convective activity and decreased venting could be factors involved in this. These two phenomena could facilitate the development of deep precipitation layers, which is conducive to precipitation occurring simultaneously on both sides of the Continental Divide (Thériault et al. 2022).

Increasingly elevated snow-lines associated with climate change are creating preferential warming at mid-elevations in parts of the Canadian Rockies due to the snow-albedo feedback (Minder et al. 2018). This type of warming is occurring in the late winter and spring from January through to May (Minder et al. 2018). January and February of both 2015 and 2016 were abnormally warm (Figure 5.6a). Warmer temperatures during this period could have ensured that more precipitation fell as rain instead of snow, and rain on snow events could have facilitated premature melting (Pomeroy et al. 2018). The subsequent SPADE periods (spring/early summer) in 2015 and 2016 period saw little precipitation (Figure 4.22). Decreased precipitation may have been a consequence of both decreased storm activity due to the strong El Niño event and lower precipitation from existing storms in the mountain valleys due to diminished feeder cloud development from convective heat transfer. Valley bottom convection is driven by convective heat transfer from the ground to atmosphere, which could occur until the snowline (Barry 2008). Valley clouds generated from wind interactions with topography and snowpack could create an important seeder-feeder mechanism, which could enhance spring precipitation from synoptic scale storm systems, and entrain moisture at the valley bottom by limiting incoming solar radiation and evaporation (Ramelli et al. 2021). Valley clouds may form at higher elevations in the mountains in response to unusually elevated snow lines.

Large amounts of precipitation only occurred at Nipika when the cloud base descended towards ground level and encompassed most of the valley as valley fog during observations for the SPADE campaign (in the spring/early summer of 2019). Retreating snowlines may affect where clouds form in mountain valleys due to the connection between lifting condensation level to heat and soil moisture. Higher lifting condensation levels from retreating snowlines could mean reduced valley bottom feeder clouds during the spring and early summer periods. Diminished seeder-feeder mechanisms could decrease total precipitation, and the amount of moisture available for evaporation and evapotranspiration later in the year.

Valley clouds could provide a critical interface between weather generated in higher levels of the atmosphere and the bottom of the valley, and could provide a conduit for precipitation to reach the valley bottom without being evaporated (Ramelli et al. 2021). Virga was present above Nipika on several occasions. Graphical analysis reveals that relative humidity has become increasingly low since 2011 on the western side of the Continental Divide with a large decrease at many stations during and after the strong El Niño event (Figure 5.7).

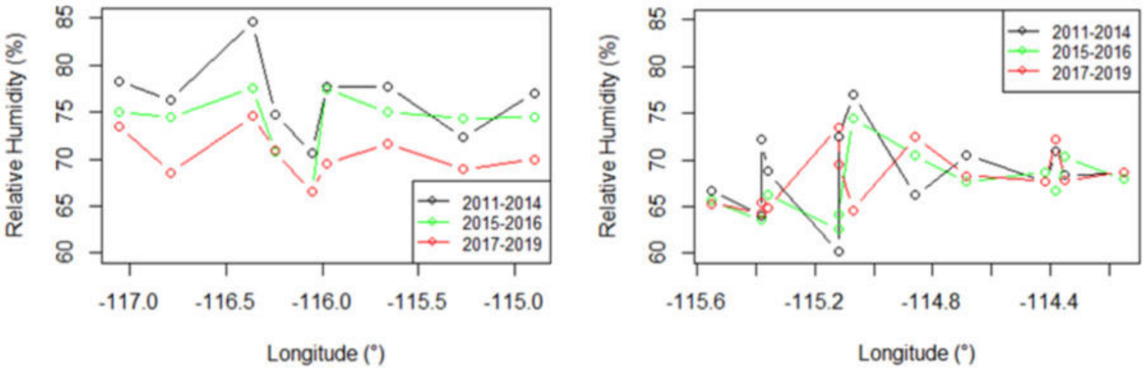

Figure 5.7. Average relative humidity plotted over longitude from meteorological stations on the western side of the Continental Divide (Right) and on the eastern side of the Continental Divide (Left) averaged over time periods that encompass the period of study before the strong El Niño event (2011-2014), during the strong El Niño event (2015-2016), and after the strong El Niño event (2017-2019).

Warmer temperatures and comparatively low amounts of precipitation associated with the 2015 spring period and 2016 spring and winter period could have created lower relative humidity, which in turn could have prevented less precipitation from reaching the ground due to increased evaporation during precipitation events. As this pattern persists, lower moisture content on the valley floor could cause drying and increased ablation in mountain valleys during valley circulations. This may explain the persistence of a large discrepancy between ERA5-Land cumulative precipitation and station cumulative precipitation into 2018, as precipitation fell preferentially at elevations, above these meteorological networks, due to evaporation.

Other factors that may have allowed relative humidity to continue to decrease could include diminished summer precipitation in 2017, increased amounts of high pressure ridging over this study area, and a decreasing southerly wind vector which can be responsible for bringing precipitation to the area (Figures 4.27 and 4.38, Stewart et al. 1995; Shea & Marshall 2007). A prevalent southerly wind vector was associated with comparatively large amounts of precipitation at Nipika during our study and comparatively large amounts of precipitation at a regional scale (Figure 4.34, Shea & Marshall 2007). A large amount of winter precipitation in southern British Columbia is associated with southerly flow from the United States (Stewart et al. 1995).

Increased atmospheric stability and cold air pooling are other factors that could enhance atmospheric decoupling and drying at lower elevations (Daly et al. 2010). Strong atmospheric blocking could have forced feeder clouds upstream of the Canadian Rockies (Ramelli et al. 2021).

5.3 Precursors for large precipitation gradients versus small precipitation gradients

Events 6 and 7 exhibited relatively strong precipitation-elevation relationships for both SPADE stations and regional networks in comparison to other precipitation events (Table 5.2). Analysis of synoptic systems indicates that during Events 6 and 7, moisture was advected westward from northeastern Alberta towards an area of low pressure to the south or southeast of the Canadian Rockies during the morning (Thériault et al. 2022). Graphical analysis of the tipping bucket transect indicates that during Event 6 a precipitation event travelled up the Cross River valley along the entire tipping bucket transect, and may have traversed the Continental Divide, impacting both sites on the eastern side (Figure 4.35 a). Graphical analysis of Event 7 demonstrates that precipitation could have migrated in a similar fashion during this event as well (Figure D.7). These smaller precipitation events could have been the consequence of convection, with previously advected moisture being warmed during morning insolation. This may have enhanced precipitation amounts at higher elevations due to convergence, facilitating relatively strong precipitation-elevation relationships. This late spring period could see the development of a higher planetary boundary layer that could facilitate the passage of convective moisture over the Continental

Divide (like Events 6 and 7), since higher diurnal temperatures and drier soils result in a higher elevation cloud base due to an elevated lifting condensation level (Barry 2008; Allabakash & Lim 2020).

Table 5.2. Summary of SPADE precipitation events including event number, event start time, length of event, total precipitation and mean temperature at Fortress, total precipitation and mean temperature at Nipika, and moisture flux across the study area.

Event	SPADE (2019)		Obs. (hrs)	Fortress Total Precip. (mm)	Fortress Mean Temp. (°C)	Nipika Total Precip. (mm)	Nipika Mean Temp. (°C)	Moisture flux
	Start (UTC)	End (UTC)						
1	22:50 26-Apr	11:00 28-Apr	35.8	32.5	-3.2	1.8	2.7	Westward
2	19:00 30-Apr	1:30 1-May	6.5	4.2	-5.8	0.0	6.6	Southeastward
3	17:00 4-May	11:20 5-May	18.5	15.3	-4.7	1.4	9.4	Eastward
4	18:00 8-May	00:00 9-May	6	1.2	2.6	0.0	16.4	Southeastward
5	5:00 16-May	22:30 18-May	65.5	20.2	-0.9	12.3	8.4	Northeastward
6	4:45 24-May	23:15 24-May	18.5	8.5	-2.1	1.4	9.7	Westward
7	12:20 25-May	00:00 26-May	11.5	15.1	0.4	1.3	10.4	Westward
8	16:00 30-May	22:10 30-May	6	6.5	7.8	0.7	11.8	Southeastward
9	1:00 7-Jun	2:00 8-Jun	25	21.4	0.1	14.5	6.5	Westward
10	10:10 14-Jun	10:40 14-Jun	0.5	2.0	5.9	0.0	10.6	Southeastward
11	20:00 17-Jun	23:50 17-Jun	3.5	1.1	12.2	0.0	25.2	Eastward
12	8:30 19-Jun	19:40 20-Jun	35	12.6	2.3	3.5	8.5	Westward
13	3:30 21-Jun	23:40 21-Jun	20.3	57.8	1.6	19.0	6.7	Westward
Shading = significant (long) event								

Poor precipitation-elevation relationships in a storm could be the result of the interactions between warm fronts and cool stable air masses. In one circumstance, the passage of a warm front over the crest of a mountain towards stable layers in the lee facilitates the persistence of these stable layers due to enhanced atmospheric stability (Siler & Durran 2016). Subsequently, spill-over from an impending storm across a mountain crest can migrate horizontally since the stable layer dampens gravity waves and diminishes lee-side evaporation and descent (Siler & Durran 2016). This type of precipitation migration can diminish the magnitude of the rain shadow effect in the lee (Siler & Durran 2016).

Precipitation Event 5 could demonstrate aspects of this interaction, with poor precipitation-elevation relationships at SPADE stations and across the study area, and a negative precipitation-elevation relationship between stations along the TBRG transect (Table 5.3). Relatively cool temperatures, a high pressure centre east of the Canadian Rockies, and a comparatively high rate of precipitation at the lowest elevation and most westerly station (Nipika) in relation to higher elevation sites along the transect and Fortress Junction, could also indicate lower-elevation blocking of an impending storm by cool and stable air masses. Another feature that could have contributed to low precipitation-elevation relationships during this event was moisture advection from the south, a direction which is roughly parallel to mountain crests in the Canadian Rockies.

Table 5.3. Correlation between precipitation and elevation for regional networks, and correlation between precipitation and elevation for SPADE stations during each 2019 precipitation event. Only a maximum of six SPADE stations was available for each event. Events with a strong precipitation-elevation relationship for both groups of stations are highlighted in red (Events 6 and 7), while an event (Event 5) with a weak precipitation-elevation relationship for both groups of stations is highlighted in blue.

Event Number	2019 Events		Precipitation-Elevation Relationship: Regional Networks		Precipitation-Elevation Relationship: SPADE Stations		Moisture flux
	Start	End	Corr.	*p*-value	Corr.	*p*-value	
1	22:50 26-Apr	11:00 28-Apr	0.401	< 0.001	0.831	< 0.05	Westward
2	19:00 30-Apr	1:30 1-May	0.309	< 0.01	0.823	< 0.05	Southeastward
3	17:00 4-May	11:20 5-May	0.489	< 0.001	0.815	< 0.05	Eastward
4	18:00 8-May	00:00 9-May	0.0656	not sig.	0.791	not sig.	Southeastward
5	5:00 16-May	22:30 18-May	0.149	not sig.	0.424	not sig.	Northeastward
6	4:45 24-May	23:15 24-May	0.412	< 0.001	0.980	< 0.001	Westward
7	12:20 25-May	00:00 26-May	0.381	< 0.001	0.932	< 0.01	Westward
8	16:00 30-May	22:10 30-May	0.439	< 0.001	0.805	not sig.	Southeastward
9	1:00 7-Jun	2:00 8-Jun	0.188	not sig.	0.772	not sig.	Westward
10	10:10 14-Jun	10:40 14-Jun	0.075	not sig.	0.843	not sig.	Southeastward
11	20:00 17-Jun	23:50 17-Jun	0.093	not sig.	0.800	not sig.	Eastward
12	8:30 19-Jun	19:40 20-Jun	0.441	< 0.001	0.485	not sig.	Westward
13	3:30 21-Jun	23:40 21-Jun	0.474	< 0.001	0.733	not sig.	Westward

5.4 Comparison between ERA5-Land Data and Station Data

This study on precipitation gradients in the southern Canadian Rockies from 2011 and 2019 revealed that total annual precipitation amounts were significantly larger in the years before 2014 than they were for the years during and after a strong El Niño event (e.g. Figure 4.23). Total precipitation was 15% higher during the 2011 to 2014 period than it was during the 2015 to 2019 period. When total precipitation from stations located within the study area was compared to total precipitation from ERA5-Land reanalysis data from these locations, ERA5-Land reanalysis data agreed well with station data from the 2011 to 2014 period, but had significantly larger values than station values for the 2015 to 2019 period (Figure 4.1). ERA5-Land precipitation values for each cell are derived from all land elevations simultaneously, and station precipitation values were derived mainly from comparatively lower elevation stations in this study (Figure 3.5 a). Local atmospheric decoupling could explain the difference between the ERA5-Land precipitation values and station values. Since ERA5 precipitation data are derived from a higher mean elevation than station data used in this study, they comprise of a smaller proportion of meteorological data from low elevation sites. Localized atmospheric decoupling between synoptic systems and lower elevation sites could happen through a variety of mechanisms including increased evaporation and increased atmospheric stability.

5.5. Study Limitations

This study has numerous limitations, and should be considered a preliminary survey of precipitation gradients in the southern Canadian Rockies. One of the main limitations to this study is the amount of meteorological data that is available for each study period. Weather station data are much more numerous over shorter periods of time than they are for longer periods of time. One consequence of this constraint is that precipitation maps for the shorter-time periods have a greater resolution, and they also incorporate more high elevation stations. This is due to the higher likelihood that meteorological stations will experience some sort of failure due to long-term exposure to mountain weather, particularly at higher elevations. As a consequence of inclement weather, higher elevation stations are often only operational during the summer months.

Wind-induced undercatch of precipitation is prominent at high elevation sites due to strong winds, and cold temperatures (Pan et al. 2016). Due to a strong relationship with snow, wind-induced undercatch occurs in greater proportions during cool periods in comparison to warm periods. Large amounts of wind-induced undercatch were identified at the CCRN station Marmot/Fisera Ridge which is located in open alpine tundra. This station was used to examine the 2019 SPADE period which straddles the warm period (May to October) and the cool period (October to May) (Pan et al. 2016). Therefore, it is likely that wind-induced undercatch affected precipitation totals at this site. Additionally, it is likely that other high elevation sites in exposed areas were also subjected to some wind-induced undercatch.

Some environmental features may have reduced rates of wind-induced undercatch at high elevation sites. Many of my higher elevation sites were shielded by brush or forest vegetation (e.g. the Pluvio at Fortress Mountain and various precipitation gauges belonging to ACIS and FLNRORD). Sites with brush or forest shielding have been demonstrated to require negligible adjustments (Pan et al. 2016). In addition to vegetative shielding, metal shields such as Alter shields reduce wind-induced undercatch (Colli et al. 2015; Kochendorfer et al. 2017; Milewska et al. 2019). These shields are present on many of the gauges used in my study, particularly those belonging to the ACIS and CCRN networks. A site with proper shielding may experience negligible wind-induced undercatch.

General transfer functions, or mathematical equations that are used to adjust for wind-induced undercatch may be difficult to apply to mountainous environments (Kochendorfer et al. 2017). Overall mountainous sites are more difficult to correct for bias. This may be due to the presence of standing vertical circulations affecting winds. In one study, gauges in mountainous environments had to be adjusted both upward and downward for bias (Kochendorfer et al. 2017). Wind-induced undercatch may have been present at many of my sites but site location and Alter shield installation may have mitigated some of it. Also, general transfer functions may not be easily applied in this mountainous region.

Station malfunction can occur even during ideal weather conditions and over short time-frames. During our study, two TBRGs became inoperable due to the accumulation of vegetative debris and pedestal failures. The remote locations of these instruments meant that we were unable to determine if these failures resulted in precipitation loss. Despite substantial efforts at quality control, some ambiguity around TBRG precipitation accumulation from the 2019 SPADE precipitation events remains. While these data represent a very small portion of the larger dataset, these issues are indicative of the tenuous lifespan of meteorological instruments in remote environments. Some unreported errors from instruments belonging to other organizations could exist in my dataset.

Another limitation to this study is the short period of time over which it occurred. This study spans nine years, therefore it is difficult to determine what base-line conditions are for this region. Additionally, one of the largest El Niño events of all time occurred during this period. It is possible that this large-scale anomaly is subtly impacting precipitation maps and analyses that are aggregates of the entire study period.

The placement of these meteorological stations in the terrain could limit accurate measurements of precipitation accumulation in this region. My meteorological sites disproportionately favour lower elevation sites; therefore, higher elevation site characteristics are under-represented.

Another major problem with my study is the denser array of stations on the eastern side of the Continental Divide in comparison to the western side of the Continental Divide. Additionally, many stations on the western side of the Continental Divide, which are geared towards forest fire prevention, do not receive as rigourous a quality control as stations on the eastern side of the Continental Divide, which are geared towards agriculture. Most of the stations on the western side of the Continental Divide are tipping buckets. This prevalence of tipping buckets could lead to inaccurate precipitation amounts for the network during solid precipitation events or cold seasons. This deficiency could affect the precipitation-elevation relationship since higher elevation sites are disproportionately exposed to cold weather. Some poor precipitation-elevation relationships were identified using these buckets, but these poor relationships persisted in seasons with liquid precipitation, so it is likely that this finding is not entirely due to TBRG underperformance.

The time-frames for the 2019 SPADE precipitation events underwent several iterations in an attempt to accurately capture each event on the landscape. However, the large geographical extent of the SPADE study area and complexities associated with orographically enhanced precipitation, means that segments of precipitation events could remain undocumented. Additionally, the majority of precipitation gauges in the SPADE study area measure precipitation at hourly intervals at the start of each hour, but precipitation events often did not end at the start of the hour. Consequently, we had to assume that precipitation accumulation from the rest of the hour could be assigned to the precipitation event.

Finally, in addition to errors associated with measuring precipitation, there may be errors associated with mapping these data and creating precipitation gradients across the geographical extent of the SPADE study area. The ArcGIS Natural Neighbour interpolation technique depends on assumptions about relationships between points on a two dimensional surface. This GIS technique did not refer to digital elevational models during the interpolation process. Therefore, orographic enhancement of precipitation that occurred in sites without precipitation gauge data is likely missing from my precipitation gradients. This could include areas of substantial orographic enhancement, such as mountain tops, where meteorological instruments are mostly absent.

Chapter 6: Conclusion

Cumulative precipitation amounts varied considerably across various time-frames including inter-annual periods such as the SPADE period and intra-annual periods such as seasons. Certain patterns in precipitation gradients were identified despite changes in precipitation amounts. Cumulatively, elevation was a good predictor for precipitation, with the highest elevation sites receiving the most precipitation during most periods of measurement including years and SPADE periods when the entire study area was examined. The highest elevation sites also received the most precipitation during spring, fall, and winter; but some mid-elevation sites received the most precipitation during the summer period. Elevation was not a good predictor on the western side of the Continental Divide for many time periods. This pattern may have been due to broader synoptic scale meteorological features such as high pressure systems and arctic air masses impinging on the Canadian Rockies. It may have also been due precipitation crossing the Continental Divide.

Differences in precipitation can be detected between warm and cool seasons. Large precipitation maxima exist at the highest sites during the cool seasons. However, during winter there is no obvious precipitation/elevation relationship until 2000 m, with a large positive precipitation/elevation relationship only above this elevation. This may be due to increased atmospheric stability during this season, coupled with increased winds and storm activity at higher elevations. Precipitation maxima were spread throughout the eastern side of the Continental Divide during the summer season, with some high elevation sites and some mid-elevation sites receiving the most cumulative precipitation. Bulls-eye shaped precipitation maxima were situated along the Continental Divide during the cool seasons. Linear precipitation maxima existed around parts of Continental Divide and throughout the eastern part of the study area during the summer. These linear features suggest that precipitation or precipitation events migrated further during warm seasons in comparison to cold seasons. Winter and summer exhibited distinct sets of precipitation patterns, while spring and fall appeared to be hybrids of these two seasons.

Inter-annual precipitation amounts varied considerably with the 2011-2014 period receiving more precipitation than the 2015-2019 period for both the annual and the SPADE periods. Longitude was the best predictor of precipitation amounts for the 2011-2014 SPADE periods, but elevation was the best predictor of precipitation amounts for the 2015-2019 SPADE periods. Elevation was the best predictor for precipitation amounts across all annual periods. Intra-annual variability varied considerably since each precipitation event during SPADE exhibited unique precipitation gradients and precipitation amounts at each site varied between storms. Intra-annual precipitation gradients varied considerably between cool and warm seasons as discussed above.

Connections between wind patterns/storm-trajectories and precipitation gradients were tenuous. At Nipika, large precipitation events seemed to have a southerly wind vector for at least some of the event. At a regional scale, southerly flow may be connected to larger amounts of precipitation on the western side of the Continental Divide, but this relationship should be tested further. Differences in cumulative precipitation amounts between the 2011-2014 period and the 2015-2019 period could be related to changes in storm trajectories due to the strong El Niño of event of 2014-2016 and other temperature anomalies in the Pacific Ocean.

6.1 Broader Implications of this Work

This work serves as a cursory examination of precipitation in the Southern Canadian Rockies. Some broader implications of this work highlight the dearth of literature on precipitation patterns in this region. Contrary to existing literature, this study was unable to identify strong positive precipitation-elevation relationships on the western side of the Continental Divide. This study highlights the need for additional examinations of this geographical area to determine if this is a new meteorological phenomenon or a consequence of low station density and/or poor station performance. Another implication of this study is that precipitation amounts varied substantially across time (although precipitation patterns exhibited similarities across time). This study highlights the need for greater monitoring to manage for future water resources.

6.2 Future Research

Temperatures have increased in the southern Canadian Rockies and are expected to continue to rise as a consequence of anthropogenic climate change (Ahrens et al. 2012; Marshall 2014; Wallace & Minder 2021). Globally, the year 2016 was the warmest annual surface temperature on record (NOAA (a) 2021), which was coincident with the strongest El Niño event on record (which persisted from the winter of 2014 through to the spring of 2016) (NOAA (b) 2021). In the southern Canadian Rockies, the mean annual temperature was about 1°C higher for 2015 and 2016 in comparison to annual mean temperatures for adjacent years at meteorological stations in our study area (Figure 4.31 (a.)). Although the impacts of climate change remain unknown, the sharp increase in temperature associated with this very strong El Niño event could allow us to examine potential consequences of climate change induced temperature changes in Canadian Rocky Mountain precipitation gradients.

Future research could include distributing a larger array of meteorological stations. This may include higher density arrays, allowing for a higher resolution analysis of precipitation amounts and gradients. A denser array of meteorological stations may enable precipitation gradients to be linked to specific topographical features. It may also allow features such as circular winter precipitation patterns to be compared with the more linear patterns that are characteristic of summertime precipitation in our study. This might allow for mechanisms behind these patterns, and atmospheric phenomena such as blocking and west to east drying patterns, to be isolated.

Numerous all weather automated weighing gauges could be deployed on the western side of the Continental Divide to make more accurate comparisons to the existing network of automated weighing gauge network on the eastern side of the Continental Divide, additionally a regional weather radar could be deployed. Additionally, ERA5-Land and station data could be compared further to determine why bias varies substantially between years.

Inter-annual and intra-annual precipitation amounts vary considerably within years and between years in this hydrologically important region, but precipitation gradients demonstrate some consistency between years. Further work identifying and monitoring precipitation gradients in this region may enhance our ability to manage valuable water resources in this region in response to a changing climate.

References

Agriculture and Irrigation, Alberta Climate Information Service (ACIS). https://acis.alberta.ca. Retrieved from January 2020 to December 2022.

Ahrens, C.D., Jackson, P.L., & Jackson, C.E. (2012). *Meteorology Today: An Introduction to Weather, Climate, and the Environment.* (1st Can. ed.). Toronto, Ontario: Nelson Education.

Allabakash S., & Lim, S. (2020). Climatology of planetary boundary layer height-controlling meteorological parameters over the Korean peninsula. *Remote Sensing, 12*(16), 2571. https://doi.org/10.3390/rs12162571

Anders, A.M., Roe, G.H., Durran, D.R., & Minder, J.R. (2007). Small scale spatial gradients in climatological precipitation on the Olympic Peninsula. *Journal of Hydrometeorology, 8*(5), 1068-1081. https://doi.org/10.1175/JHM610.1

Barnes, C., & Hopkinson, C. (2022). Quality control impacts on total precipitation gauge records for montane valley and ridge sites in SW Alberta, Canada. *Data, 7*(6)*,* 73. https://doi.org/10.3390/data7060073

Barry, R.G. (2008). *Mountain weather and climate* (3rd ed.). Cambridge University Press.

Bobrowsky, P., & Rutter, N.W. (1992). The quaternary geologic history of the Canadian Rocky Mountains. *Geographie physique et Quarternaire, 46*(1), 5-50. https://doi.org/10.7202/032887ar

Bohne, L., Strong, C., & Steenburgh, W.J. (2020). Climatology of orographic precipitation gradients in the contiguous Western United States. *Journal of Hydrometeorology, 21*(8), 1723-1740.

Colle, B.A. (2004). Sensitivity of orographic precipitation to changing ambient conditions and terrain geometries: an idealized modeling perspective. *Journal of the Atmospheric Sciences, 61*(5), 588-606. https://doi.org/10.1175/1520-0469(2004)061<0588:SOOPTC>2.0.CO;2

Colli, M., Rasmussen, R., Thériault, J.M., Lanza, L.G., Baker, C.B., & Kochendorfer, J. (2015). An improved trajectory model to evaluate the collection performance of snow gauges. *Journal of Applied Meteorology and Climatology, 54*(8), 1826-1836. https://doi.org/10.1175/JAMC-D-15-0035.1

Cosma, S., Richard, E., & Miniscloux, F. (2002). The role of small-scale orographic features in the spatial distribution of precipitation. *Quarterly Journal of the Royal Meteorological Society, 128*(576), 75-92. https://doi.org/10.1256/00359000260498798

Cullen, R., & Marshall, S. (2011). Mesoscale temperature patterns in the Rocky Mountains and foothills region of Southern Alberta. *Atmosphere-Ocean, 49*(3), 189-205. https://doi.org/10.1080/07055900.2011.592130

Daly, C., Conklin, D.R., & Unsworth, M.H. (2010). Local atmospheric decoupling in complex topography alters climate change impacts. *International Journal of Climatology, 30*(12), 1857-1864. https://doi.org/10.1002/joc.2007

De Wekker, S.F.J., Steyn, D.G., & Nyeki, S. (2004). A comparison of aerosol-layer and convective boundary-layer structure over a mountain range during Staaarte '97. *Boundary Layer Meteorology, 113*(2), 249–271. https://doi.org/10.1023/B:BOUN.0000039371.41823.37

Duchon, C.E. & Biddle, C.J. (2010). Undercatch of tipping-bucket gauges in high rain rate events. *Advances in Geosciences, 25*, 11–15. https://doi.org/10.5194/adgeo-25-11-2010

Environment and Climate Change Canada. (2020). Canadian Weather Radar. Retrieved from https://www.weather.gc.ca/map_e.html?layers=radar

Feng, Z., Houze, R., Leung, L.R., Song, F., Hardin, J., Wang, J., Gustafson, W., & Homeyer, C. (2019). Spatiotemporal characteristics and large-scale environments of mesoscale convective systems east of the Rocky Mountains. *Journal of Climate, 32*(21), 7303-7309. https://doi.org/ 10.1175/JCLI-D-19-0137.1

Foresti, L., Sideris, I.V., Panziera, L., Nerini, D., & Germann, U. (2018). A 10-year radar-based analysis of orographic precipitation growth and decay patterns over the Swiss Alpine region. *Quarterly Journal of the Royal Meteorological Society, 144*(716), 2277-2301. https://doi.org/10.1002/qj.3364

Fox, J., & Weisberg, S. (2018). Appendix: Nonparametric Regression in R (PDF) In *An R Companion to Applied Regression* (3rd ed.). Sage Publications https://socialsciences.mcmaster.ca/jfox/Books/Companion/appendices/Appendix-Nonparametric-Regression.pdf. Last accessed July 9, 2022.

Hik, S., & Williamson, S.N. (2019). Need for mountain weather stations climbs. *Science, 366*(6469), 1083. https://.doi.org/10.1126/science.aaz7450

Immerzeel, W.W., Lutz, A.F., Andrade, M, Bahl, A., Biemans, H., Bolch, T., Hyde, S., Brumby, S., Davies, B.J., Elmore, A.C., Emmer, A., Feng, M., Fernández, A., Haritashaya, U., Kargel, J.S., Koppes, M., Kraaijenbrink, P.D.A., Kulkarni, A.V., Mayewski, P.A., … Baillie, J.E.M. (2020). Importance and vulnerability of the world's water towers. *Nature, 577***,** 364–369. https://doi.org/10.1038/s41586-019-1822-y

Johansson, B., & Chen, D. (2003). The influence of wind and topography on precipitation distribution in Sweden: statistical analysis and modelling. *International Journal of Climatology, 23(*12), 1523 – 1535. https://doi.org/10.1002/joc.951

Johnson, E., & Wowchuk, D.R. (1993). Wildfires in the southern Canadian Rocky Mountains and their relationship to mid-tropospheric anomalies. *Canadian Journal of Forest Research, 23*(6), 1213-1222. https://doi.org/10.1139/x93-153

Kochendorfer, J., Nitu, R., Wolff, M., Mekis, E., Rasmussen, R., Baker, B., Earle, M. E., Reverdin, A., Wong, K., Smith, C. D., Yang, D., Roulet, Y.-A., Buisan, S., Laine, T., Lee, G., Aceituno, J. L. C., Alastrué, J., Isaksen, K., Meyers, T., Brækkan, R., Landolt, S., Jachcik, A., and Poikonen, A. (2017). Analysis of single-Alter-shielded and unshielded measurements of mixed and solid precipitation from WMO-SPICE. *Hydrology and Earth System Sciences*, *21*(7), 3525–3542, https://doi.org/10.5194/hess-21-3525-2017

Kochendorfer, J., Earle, M., Rasmussen, R., Smith, C., Yang, D., Morin, S., Mekis, É., Buisan, S., Roulet, Y-A., Landolt, S., Wolff, M., Hoover, J., Thériault, J., Lee, G., Baker, B., Nitu, R., Lanza, L., Colli, M., Meyers, T. (2021). How well are we measuring snow post-SPICE? *Bulletin of the American Meteorological Society, 103*(2) 1-49. https://doi.org/10.1175/BAMS-D-20-0228.1

Luce, C.H., Abatzoglou, J.T., & Holden, J.T. (2013). The missing mountain water: slower westerlies decrease orographic enhancement in the Pacific Northwest USA. *Science, 342*(6164), 1360-1364. https://doi.org/10.1126/science.1242335

Marshall, S.J. (2014). Meltwater run-off from Haig Glacier, Canadian Rocky Mountains, 2002-2013. *Hydrology and Earth System Sciences, 18*(12), 5181-5200. https://doi.org/10.5194/hess-18-5181-2014

Mass, C., Johnson, N., Warner, M., & Vargas, R. (2015). Synoptic control of cross-barrier precipitation ratios for the Cascade Mountains. *Journal of Hydrometeorology, 16*(3), 1014-1028.

Mekis, E., Donaldson, N., Reid, J., Zucconi, A., Hoover, J., Li, Q., Nitu, R., & Mello, S. (2018). An overview of surface-based precipitation observations at Environment and Climate Change Canada. *Atmosphere-Ocean, 56*(2), 71-95. https://doi.org/10.1080/07055900.2018.1433627

Milewska, E.J., Vincent, L.A., Hartwell, M.M., Charlesworth, K., & Mekis, E. (2019). Adjusting precipitation amounts from Geonor and Pluvio automated weighing gauges to preserve continuity of observations in Canada. *Canadian Water Resources Journal, 44*(2), 127-145. https://doi.org/10.1080/07011784.2018.1530611

Minder, J. R., Letcher, T. W., & Liu, C. (2018). The character and causes of elevation-dependent warming in high-resolution simulations of Rocky Mountain climate change. *Journal of Climate, 31*(6), 2093-2113. https://doi.org/10.1175/JCLI-D-17-0321.1

Mo, R., Brugman, M., Milbrandt, J., Goosen, J., Geng, Q., Emond, C., Bau, J., Erfani, A. (2019). Impacts of hydrometeor drift on orographic precipitation: Two case studies of landfalling atmospheric rivers in British Columbia, Canada. *Weather and Forecasting, 34*(5), 1211-1237. https://doi.org/10.1175/WAF-D-18-0176.1

Mo, R., So, R., Brugman, M., Mooney, C., Liu, A., Jakob, M., Castellan, A., & Vingarzan, R. (2021). Column relative humidity and primary condensation rate as two useful supplements to atmospheric river analysis. *Water Resources Research, 57*(11), e2021WR029678. https://doi.org/10.1029/2021WR029678

Moran, T., Marshall, S.J., Evans, E.C., & Sinclair, K.E. (2007). Altitudinal gradients of stable isotopes in lee-slope precipitation in the Canadian Rockies. *Arctic, Antarctic, and Alpine Research, 39*(3), 455-467. https://doi.org/10.1657/1523-0430(06-022)[MORAN]2.0.CO;2

Mott, R., Daniels, M., & Lehning, M. (2015). Atmospheric flow development and associated changes in turbulent sensible heat flux over a patchy mountain snow cover. *Journal of Hydrometeorology, 16*(3), 1315-1340. https://doi.org/1315–1340. 10.1175/JHM-D-14-0036.1

Mott, R., Egli, L., Grünewald, T., Dawes, N., Manes, C., Bavay, M., & Lehning, M. (2011). Micrometeorological processes driving snow ablation in an Alpine catchment. *The Cryosphere, 5*(4), 1083–1098. https://doi.org/10.5194/tc-5-1083-2011

Mott, R., Paterna, E., Horender, S., Crivelli, P., & Lehning, M. (2016). Wind tunnel experiments: cold-air pooling and atmospheric decoupling above a melting snow patch. *The Cryosphere, 10*(1), 445–458. https://doi.org/10.5194/tc-10-445-2016

Mott, R., Scipión, D., Schneebeli, M., Dawes, N., Berne, A., & Lehning, M. (2014). Orographic effects on snow deposition patterns in mountainous terrain. *Journal of Geophysical Research: Atmospheres, 119*(3), 1419–1439. https://doi.org/10.1002/2013JD0198802914

Mott, R., Vionnet, V., & Grünewald, T. (2018). The seasonal snow cover dynamics: Review on wind-driven coupling processes. *Frontiers in Earth Science, 6*:197. https://doi.org/10.3389/feart.2018.00197

Muchan, K. & Dixon, H. (2019). Insights into rainfall undercatch for differing raingauge rim heights. *Hydrology Research, 50*(6), 1564–1576. https://doi.org/10.2166/nh.2019.024

Neiman, P.J., Ralph, F.M., White, A.B., Kingsmill, D.E., & Persson, P.O.G. (2002). The statistical relationship between upslope flow and rainfall in California's coastal mountains: observations during CALJET. *Monthly Weather Review, 130*(6), 1468-1492.

NOAA (a). 2020 was Earth's 2nd Hottest year, just behind 2016. https://www.noaa.gov/news/2020-was-earth-s-2nd-hottest-year-just-behind-2016. Last accessed November 11, 2021.

NOAA (b). 2014-2016 El Niño Assessment Report. https://www.ncdc.noaa.gov/sites/default/files/attachments/ENSOTT_Report_02.26.2018%20FINAL%20draft.pdf. Last accessed November 11, 2021.

Pan, X., Yang, D., Li, Y., Barr, A., Helgason, W., Hayashi, M., Marsh, P., Pomeroy, J., and Janowicz, R. J. (2016). Bias corrections of precipitation measurements across experimental sites in different ecoclimatic regions of western Canada. *The Cryosphere, 10*(5), 2347–2360, https://doi.org/10.5194/tc-10-2347-2016

Pollock, M.D., O'Donnell, G., Quinn, P., Dutton, M., Black, A., Wilkinson, M.E., Colli, M., Stagnaro, M., Lanza, L.G., Lewis, E., Kilsby, C.G., O'Connell, P.E. (2018). Quantifying and mitigating wind-induced undercatch in rainfall measurements. *Water Resources Research, 54*(6), 3863– 3875. https://doi.org/10.1029/2017WR022421

Pomeroy, J.W., Stewart, R.E., & Whitfield, P.H. (2016). The 2013 flood event in the South Saskatchewan and Elk River basins: Causes, assessment and damages. *Canadian Water Resources Journal, (41)*1-2, 105-117. http:// doi.org/10.1080/07011784.2015.1089190

Ramelli, F., Henneberger, J., David, R., Lauber, A., Pasquier, J., Wieder, J., Bühl, J., Seifert, P., Engelmann, R., Hervo, M., & Lohmann, U. (2021). Influence of low-level blocking and turbulence on the microphysics of a mixed-phase cloud in an inner-alpine valley. *Atmospheric Chemistry and Physics, 21*(6), 5151–5172. https://doi.org/10.5194/acp-21-5151-2021

Roe, G. (2005). Orographic precipitation. *Annual Review of Earth and Planetary Sciences, 33*, 645-671. https://doi.org/10.1146/annurev.earth.33.092203.122541

Rood, S.B., Pan, J., Gill, K.M., Franks, C.G., Samuelson, G.M., & Shepherd, A. (2008). Declining summer flows of the Rocky Mountain rivers: changing seasonal hydrology and probable impacts on floodplain forests. *Journal of Hydrology, 349*(3-4), 397-410. https://doi.org/10.1016/j.jhydrol.2007.11.012

Rood, S.B., Samuelson, G.M., Weber, J.K, & Wywrot, K.A. (2005). Twentieth-century decline in streamflows from the hydrographic apex of North America. *Journal of Hydrology, 306*(1-4), 215-233. https://doi.org/10.1016/j.jhydrol.2004.09.010

Scaff, L., Prein, A., Li, Y., Liu, C., Rasmussen, R., & Ikeda, K. (2020). Simulating the convective precipitation diurnal cycle in North America’s current and future climate. *Climate Dynamics, 55*(1-2). 369-382. https://doi.org/10.1007/s00382-019-04754-9

Schindler, D.W., & Donahue, W.F. (2006). An impending water crisis in Canada’s western prairie provinces. *Proceedings of the National Academy of Sciences of the United States of America, 103*(19), 7210-7216. https://doi.org/10.1073/pnas.0601568103

Sharma, A.R., & Déry, S.J. (2016). Elevational dependence of air temperature variability and trends in British Columbia’s Cariboo Mountains. *Atmosphere-Ocean, 54*(2), 153-170. http://dx.doi.org/10.1080/07055900.2016.1146571

Shea, J., Marshall, S.J., & Livingston, J.M. (2004) Glacier distributions and climate in the Canadian Rockies. *Arctic, Antarctic, and Alpine Research, 36*(2), 272-279. https://doi.org/10.1657/1523- 0430(2004)036[0272:GDACIT]2.0.CO;2

Shea, J., & Marshall, S. (2007). Atmospheric flow indices, regional climate, and glacier mass balance in the Canadian Rockies. *International Journal of Climatology, 27*(2). 233-247. https://doi.org/10.1002/joc.1398

Siler, N., & Durran, D. (2016). What causes weak orographic rain shadows? Insights from case studies in the Cascades and idealized simulations. *Journal of the Atmospheric Sciences, 73*(10), 4077-4099. https://doi.org/10.1175/JAS-D-15-0371.1

Siler, N., Roe, G., & Durran, D. (2013). On the dynamical causes of variability in the rain-shadow effect: a case study of the Washington Cascades. *Journal of Hydrometeorology, 14*(1), 122-139. https://doi.org/10.1175/JHM-D-12-045.1

Sinclair, K.E., & Marshall, S.J. (2009). Temperature and vapour-trajectory controls on the stable-isotope signal in the Canadian Rocky Mountain snowpacks. *Journal of Glaciology, 55*(191), 485-497. https://doi.org/10.3189/002214309788816687

Smith, C. D. (2008). The relationship between monthly precipitation and elevation in the Alberta Foothills during the Foothills Orographic Precipitation Experiment. In M. Woo (Ed.), *Cold Region Atmospheric and Hydrologic Studies, The Mackenzie GEWEX Experience Volume 1: Atmospheric Dynamics*, pp. 167-183, Berlin, Heidelberg: Springer.

Stewart, R.E., Bachand, D., Dunkley, R.R., Giles, A.C., Lawson, B., Legal, L., Miller, S.T., Murphy, B.P., Parker, M.N., Paruk, B.J. & Yau, M.K. (1995). Winter storms over Canada. *Atmosphere-Ocean, (33)*2, 223-247. https://doi.org/10.1080/07055900.1995.9649533

Stockham, A.J., Schultz, D.M., Fairman, J.G., & Draude, A.P. (2018). Quantifying the rain-shadow effect: results from the Peak District, British Isles. *Bulletin of the American Meteorological Society, 99*(4), 777–790. https://doi.org/10.1175/BAMS-D-17-0256.1

Thériault, J. M., Déry, S. J., Pomeroy, J. W., Smith, H. M., Almonte, J., Bertoncini, A., Crawford, R. W., Desroches-Lapointe, A., Lachapelle, M., Mariani, Z., Mitchell, S., Morris, J. E., Hébert-Pinard, C., Rodriguez, P., and Thompson, H. D. (2021). Meteorological observations collected during the Storms and Precipitation Across the continental Divide Experiment (SPADE), April–June 2019. *Earth System Science Data, 13*(3), 1233–1249. https://doi.org/10.5194/essd-13-1233-2021

Thériault, J.M., Hung, I., Vaquer, P., Stewart, R.E., & Pomeroy, J.W. (2018). Precipitation characteristics and associated weather conditions on the eastern slopes of the Canadian Rockies during March–April 2015. *Hydrology and Earth System Sciences, 22*(8), 4491-4512. https://doi.org/10.5194/hess-22-4491-2018

Thériault, J. M., Leroux, N. R., Stewart, R. E., Bertoncini, A., Déry, S. J., Pomeroy, J. W., Thompson, H. D., Smith, H., Mariani, Z., Desroches-Lapointe, A., Mitchell, S., & Almonte, J. (2022). Storms and Precipitation Across the continental Divide Experiment (SPADE). *Bulletin of the American Meteorological Society*, *103*(11), E2628-E2649. https://doi.org/10.1175/BAMS-D-21-0146.1

Thornton, P.E., Thornton, M.M., Mayer, B.W., Wilhelmi, N., Wei, Y., Devarakonda, R., & Cook, R.B. (2014). Daymet: Daily Surface Weather Data on a 1-km Grid for North America, Version 2. ORNL DAAC, Oak Ridge, Tennessee, USA. https://doi.org/10.3334/ORNLDAAC/1219

Turner, J.K., & Gyakum, J.R. (2011). The development of arctic air masses in Northwest Canada and their behavior in a warming climate. *Journal of Climate, 24*(17), 4618-4633. https://doi.org/10.1175/2011JCLI3855.1

US Global Change Research Program. (2017). Climate Science Special Report. NCA4. Volume 1. https://science2017.globalchange.gov/chapter/7/. Last accessed November 20, 2021.

Wallace, B., & Minder, J.R. (2021). The impact of snow loss and soil moisture on convective precipitation over the Rocky Mountains under climate warming. *Climate Dynamics, 56*(13)**,** 2915–2939. https://doi.org/10.1007/s00382-020-05622-7

Wang, X.L., Xu, H., Qian, B., Feng, Y., & Mekis, E. (2017). Adjusted daily rainfall and snowfall data for Canada. *Atmosphere-Ocean, 55*(3), 155-168. https://doi.org/10.1080/07055900.2017.1342163

Werner, A.T., Shrestha, R.R., Cannon, A.J., Schnorbus, M.S., Zwiers, F.W., Dayon, G., & Anslow, F. (2019). A long-term, temporally consistent, gridded daily meteorological dataset for northwestern North America. *Scientific Data, 6*:180299. https://doi.org/10.1038/sdata.2018.299

Wong, J.S., Razavi, S., Bonsal, B.R., Wheater, H.S., & Asong, Z.E. (2017). Inter-comparison of daily precipitation products for large-scale hydro-climatic applications over Canada. *Hydrology and Earth System Sciences, 21*(4), 2163-2185. https://doi.org/10.5194/hess-21-2163-2017

Yu, B., & Zwiers, F. (2007). The impact of combined ENSO and PDO on the PNA climate: A 1,000-year climate modeling study. *Climate Dynamics, 29*(7). 837-851. https://doi.org/10.1007/s00382-007-0267-4

Appendix A

Periods of Time During which Stations were not Operational During SPADE

See Theriault et al. (2021) for additional information.

Nipika Mountain Resort: A Parsivel and an MRR2 were included at Nipika on 1 May, 2019. First full day of data was from 2 May, 2019. They were dismantled on 24 June, 2019 (10:45 MDT). The Parsivel was not operational between 9 May, 2019 (20:41 MDT) and 11 May, 2019 (11:04 MDT). Parsivel programming contained bugs from 9 May, 2019 until 16 May, 2019 (01:23 MDT). Parsivel was stopped for a few seconds every few days for the rest of the campaign to ensure that it did not run out of memory. There were five gaps in time in the MRR2 data file on 1 June, 2019. Most gaps were 40 seconds long, but one was 2 minutes long (all of the gaps occurred between 02:38 and 04:29 MDT). On June 8th there was one 3-minute gap in the MRR2 data file (04:50 MDT). The CR1000X including the Geonor was not operational at Nipika between 1 May, 2019 (13:30 MDT) and 2 May, 2019 (10:30 MDT). Geonor flat-lined 31 May, 2019 (10:25 MDT). It was re-programmed and became fully operational on 2 June, 2019 (14:20 MDT). Programming was adjusted again on 4 June, 2019 (11:25-11:35 MDT). The CR1000X including the Geonor was decommissioned on 24 June, 2019 (12:00 MDT).

Fortress Junction: Reduced MRR file size on 10 May, 2019, no MRR data between 11-13 May, 2019 inclusive, and a reduced MRR file on 14 May, 2019. with an. HMP, Parsivel, Pluvio, and WXT were not transmitting information between 11 May, 2019 (22:09 MDT) and 12 May, 2019 (01:02 MDT). For HMP, Parsivel, Pluvio, and WXT, file sizes were reduced on 10 May, 2019 and 13 May, 2019.

Fortress Mountain: MRR was not functioning properly between 9 May, 2019 and 14 May, 2019. All instruments were turned off briefly on 15 May, 2019 to correct MRR. MRR was not operational between 20 May, 2019 (08:32 MDT) and 24 May, 2019 (15:52 MDT). A Rubber DAQY error on 19 June, 2019 19:05-20:20 may have caused some errors in measurement readings. A reduced MRR file size is available on 22 June, 2019 and no MRR files are available after that.

Biogeoscience Institute: MRR pro was relocated from BGI to Storm Mountain Lodge June 6th-8th inclusive.

Precipitation Gauge Transect: Precipitation gauge transect was activated on 12 May, 2019 (00:00) and disassembled on 23 June, 2019 (Precipitation Gauge 1 at 13:05 MDT, Precipitation Gauge 2 at 13:42 MDT, and Precipitation Gauge 3 at 14:05 MDT). A damaged pedestal for Precipitation Gauge 1 was discovered on 20 May (12:11 MDT), it had rendered the gauge non-functional. Similar damage to the Precipitation Gauge 1 pedestal was discovered on 2 June, 2019 (11:30 MDT), again it had rendered the gauge non-functional. A clogged aperture for Precipitation Gauge 3 discovered on 23 June, 2019 (14:05 MDT), it had also rendered the gauge non-functional.

Appendix B

Technical Information for Meteorological Instruments used for the SPADE Campaign.

See Appendix A in Theriault et al. (2021) for additional information.

Geonor T-200B Single Alter shield: Capacity: 600 mm. Collecting Area: 200 cm^2. Sensitivity: 0.05 mm. Accuracy: 0.1% FS. Repeatability: 0.1 mm. Mouth of Geonor: 1.83 m above the ground.

Pluvio 2 Single Alter shield: Capacity: 750 mm. Collecting Area: 200 cm^2. Sensitivity: 0.05 mm. Accuracy: ± 0.05 mm for 60 minutes of collection time. Resolution: 0.1 mm. Mouth of Pluvio: ~2 m above the ground at Fortress Junction. Mouth of Pluvio: ~3 m above the ground at Fortress Mountain.

Davis Tipping Buckets: Tipping bucket rain gauge with magnetic switch. Designed for liquid precipitation. Increment of Measure: 0.2 mm per tip. Accuracy: for rain rates up to 100 mm/hr ±4% of the total or ± 1 tip of the bucket (whichever is greater). Temperature range: 0 to 50°C. Base of bucket was about 1 m above the ground. Orifice of tipping bucket was about 1.25 mm above the ground.

Campbell scientific HS2-C3-L: Extended temperature range -50 to +50°C. Accuracy at 23°C: ±0.1°C with standard configuration settings. Long Term Stability: < 0.1°C/year. Installed 2 m above the ground.

Vaisala HMP155: Temperature Measurement range: -80 ... +60°C (-112 ... +140°F); Accuracy with voltage output at -80 ... +20°C ±(0.226 - 0.0028 x temperature)°C ; +20 ... +60°C ±(0.055 + 0.0057 x temperature)°C; passive (resistive) output according to IEC 751 1/3 Class B ±(0.1 + 0.00167 x |temperature|)°C RS485 output -80 ... +20°C ±(0.176 - 0.0028 x temperature) °C +20 ... +60°C ±(0.07 + 0.0025 x temperature)°C; Accuracy over temperature range (opposite); Temperature sensor Pt100 RTD Class F0.1 IEC 60751; Response time with additional temperature probe in 3 m/s air flow 63%. Installed about 2 m above the ground at Fortress Junction and Fortress Mountain.

Campbell Scientific RM Young 5103AP-10-L: Wind Speed: Measurement Range: 0 to 100 m/s; Accuracy: ±0.3 m/s or 1% of reading; Starting Threshold: 1.0 m/s; Distance Constant: 2.7 m 63% recovery; Resolution: (0.0980 m s-1)/(scan rate in seconds). Anemometer was installed about 3 m above the ground. Wind Direction: Mechanical Range: 0 to 360°; Electrical Range: 355° (5° open); Accuracy: ±3°; Starting Threshold: 1.1 m/s at 10° displacement; Distance Constant: 1.3 m, 50% recovery. Anemometer installed 3 m above the ground.

Vaisala WXT520: Wind Speed: Measurement Range: 0 to 60 m/s; Response Time: 0.25 s; Accuracy ±0.3 m s-1 or ±3% whichever is greater (0 to 35 m s-1) ±5% (36 to 60 m s-1); Wind Direction: Measurement Range: 0° to 360°; Response Time: 0.25 s; Accuracy: ±3°, Output

Resolution 1°. Installed at about 2 m above the ground at Fortress Junction and Fortress Mountain.

Appendix C

Quality Control of SPADE TBRG Transect Data

See Appendix A in Theriault et al. (2021) for additional information.

There were two instances where the stand for Precipitation Gauge 1 was damaged, and in each case the pedestal was angled to a point where the precipitation gauge was no longer functional. For quality control purposes, precipitation volume data were examined for anomalies during the time-frames in which the tipping bucket was potentially off-line. Periods of zero or near-zero precipitation values, when other precipitation gauges were recording precipitation, were highlighted in the graphical analysis. Values were highlighted between May 17th and 20th, and between May 30th and June 2nd.

Precipitation Gauge 1 tipped nearly 0.2 mm of precipitation when it was off-line during maintenance on June 11th. This occurred during a dry period, so it is possible that this precipitation would have evaporated before the tipping bucket was activated. Therefore, this small amount of precipitation loss was ignored.

Precipitation Gauge 3 became filled with pine needles, and timestamps were duplicated over the last three days of the experiment. Pine needle interference occurred to the extent that Precipitation Gauge 3 logged information for June 25th, when in reality, the experiment was terminated on June 23rd. Quality control for Precipitation Gauge 3 was performed in much the same way it was performed for Precipitation Gauge 1, where, during the time-frame under question, periods where station precipitation values were low in comparison to other stations, were highlighted during the graphical analysis. Values were highlighted between June 21st and June 23rd,

Problems with Precipitation Gauge 1 occurred during periods of low precipitation volumes, so although these issues may have altered the shape of the resulting graph, these problems may not have drastically altered total precipitation amounts. A comparison with the nearest precipitation gauge, Precipitation Gauge 2, suggests that about 4-5 mm of precipitation, or about 3.5% above the current total of 125 mm, may have been lost at this station. The margin of error for this tipping bucket is around 4%.

The problem with Precipitation Gauge 3 may have occurred during a period of intense precipitation, as recorded by all other stations. Therefore, this problem may have drastically altered the last three days of the resulting graph and may have resulted in a diminished value for total precipitation at this gauge.

Appendix D

A Comparison of Wind Roses and Precipitation Events at Nipika and Fortress (the Lowest and Highest Primary SPADE Observation Sites)

Note: Wind speeds of less than 0.5 ms^{-1} have not been removed from these wind roses.

Appendix D represents a preliminary examination of wind speeds across events.

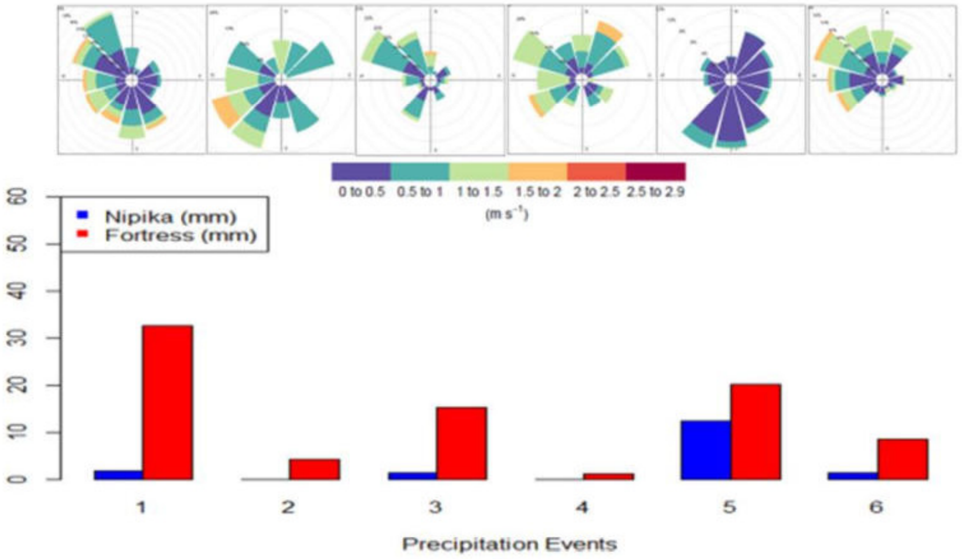

Figure D.1. Total precipitation at Nipika and Fortress Mountain for the first six SPADE precipitation events (Bottom) compared with wind direction by percent frequency of counts at Nipika for each precipitation event (Top).

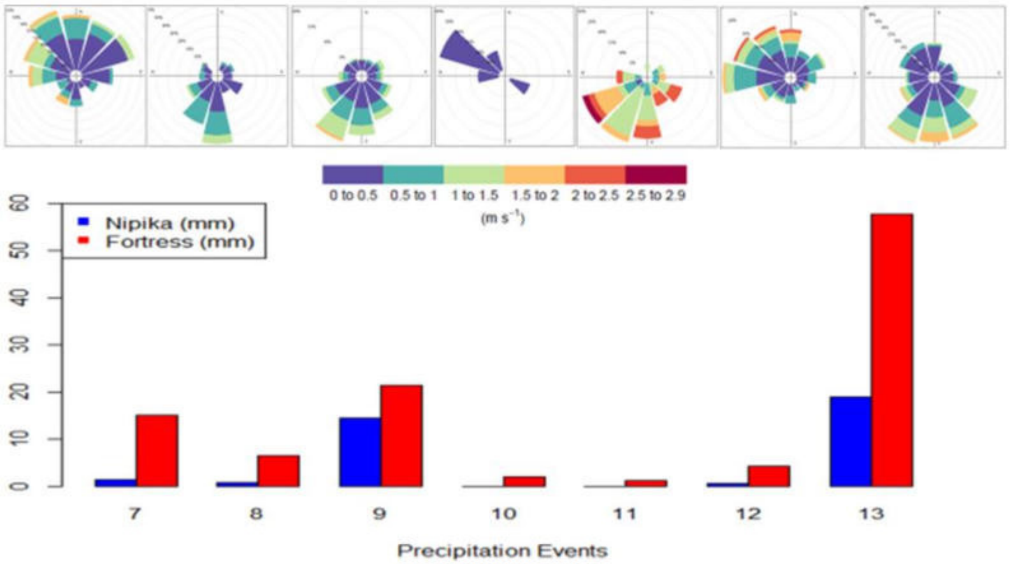

Figure D.2. Total precipitation at Nipika and Fortress Mountain for the last seven SPADE precipitation events (bottom) compared with wind direction by percent frequency of counts at Nipika for each precipitation event (top).

Nipika consistently receives wind from all directions (Figure 4.18) and this round wind profile remained relatively similar between the SPADE period and the smaller period within in it when the precipitation gauge transect was active.

Nipika received less precipitation than Fortress Mountain for each precipitation event (Figures D.1 and D.2). The three precipitation events where Nipika received more than 10 mm of precipitation had wind direction most frequently from the southwest, some comparatively large periods with wind speeds below 0.5 $m \cdot s^{-1}$, and temperatures between 5-10°C (Figures D.3 and D.4). Temperatures were lower at Nipika during these high precipitation events than they were during adjacent events with lower amounts of precipitation. The two largest precipitation events, Events 9 and 13 had very similar temperatures with average temperatures of 6.5°C and 6.7°C respectively.

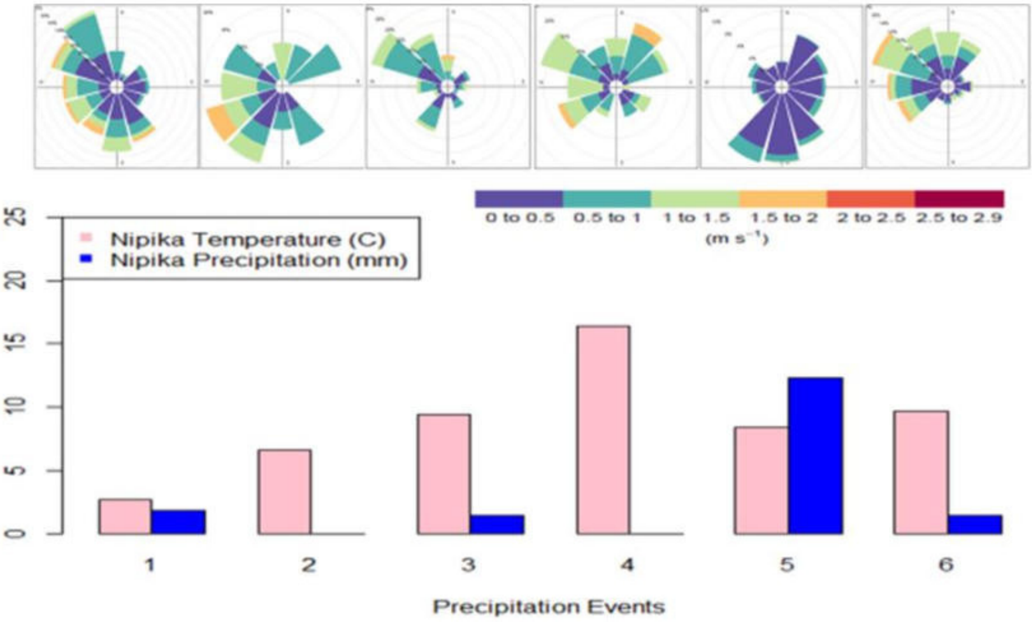

Figure D.3. Total precipitation and temperature at Nipika for the first six SPADE precipitation events (bottom) compared with wind direction by percent frequency of counts at Nipika for each precipitation event (top).

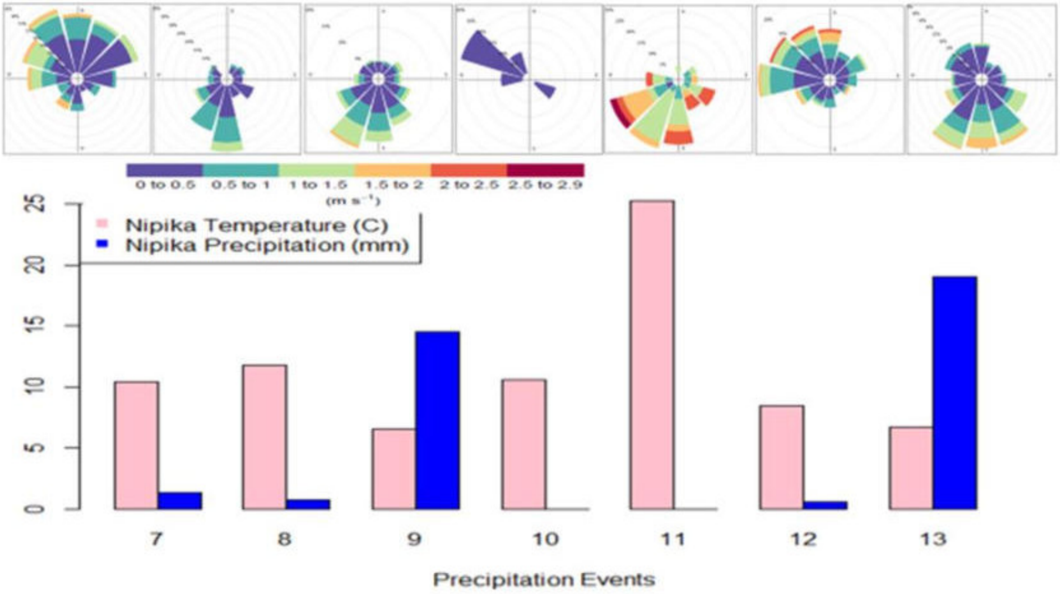

Figure D.4. Total precipitation and temperature at Nipika for the last seven SPADE precipitation events (bottom) compared with wind direction by percent frequency of counts at Nipika for each precipitation event (top).

Appendix E

LOESS regressions of cumulative precipitation across longitude during the SPADE period and the annual period (2011 to 2019). These plots contain maps of the Continental Divide.

LOESS regressions of cumulative precipitation from the SPADE period and the annual period each year (2011-2019) plotted across the longitudinal coordinate of each station. These plots denote the location of the Continental Divide.

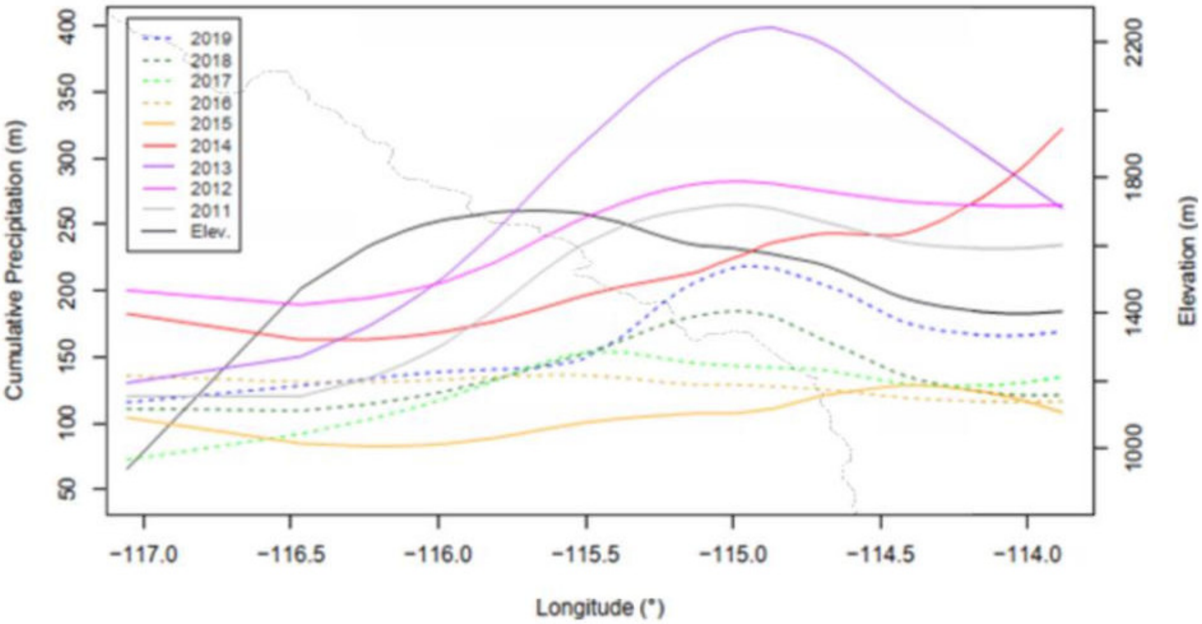

Figure E.1. LOESS regression of cumulative precipitation during the SPADE period from each year (2011-2019) plotted across the longitudinal coordinate of each station. The black line denotes a LOESS regression of average station elevation at a specific longitude. The grey line represents the location of the Continental Divide.

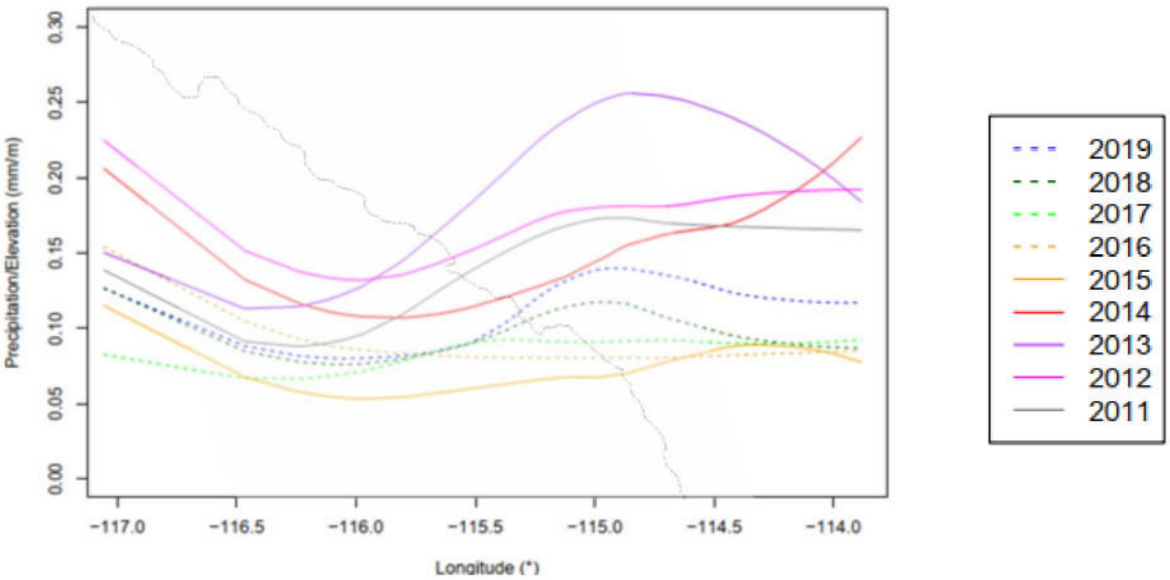

Figure E.2. LOESS regression of cumulative precipitation during the SPADE period from each year (2011-2019) plotted across the longitudinal coordinate of each station. Cumulative precipitation values at each station were divided by the elevation at each station. The grey line represents the location of the Continental Divide.

.

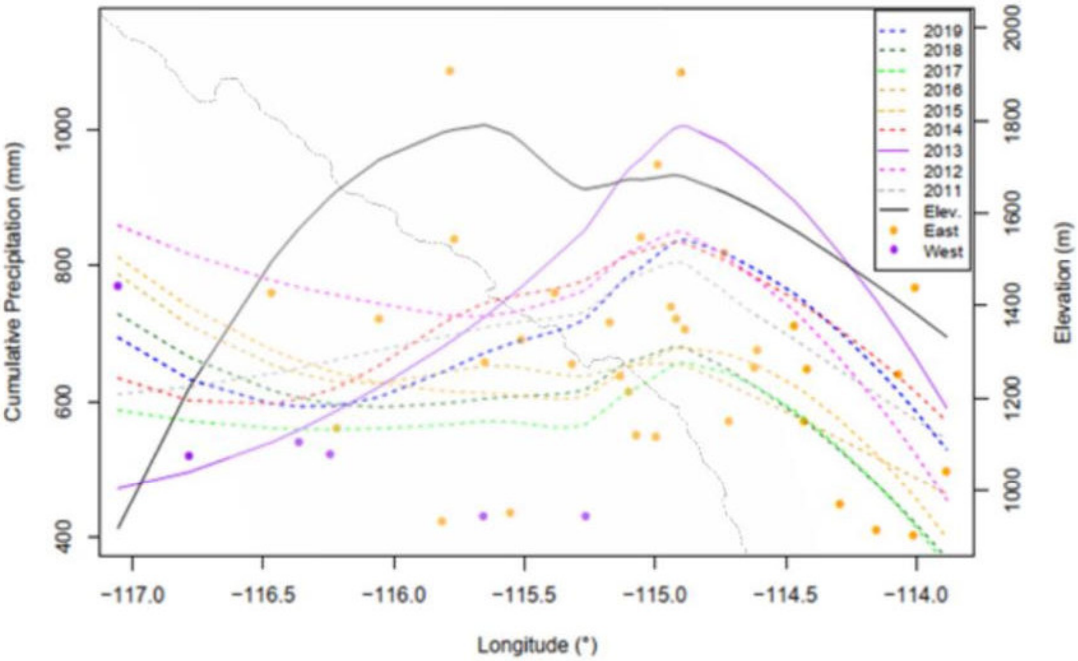

Figure E.3. LOESS regression curves of annual cumulative precipitation against longitude. Dotted lines represent years in which there was not a significant ($p < 0.05$) correlation between cumulative precipitation and longitude. Dots denote cumulative precipitation at stations. The black line denotes average station elevations at a specific longitude. The grey line represents the location of the Continental Divide. The elevational profile differs from the previous longitudinal regression because there were fewer stations available for annual time periods between 2011-2019

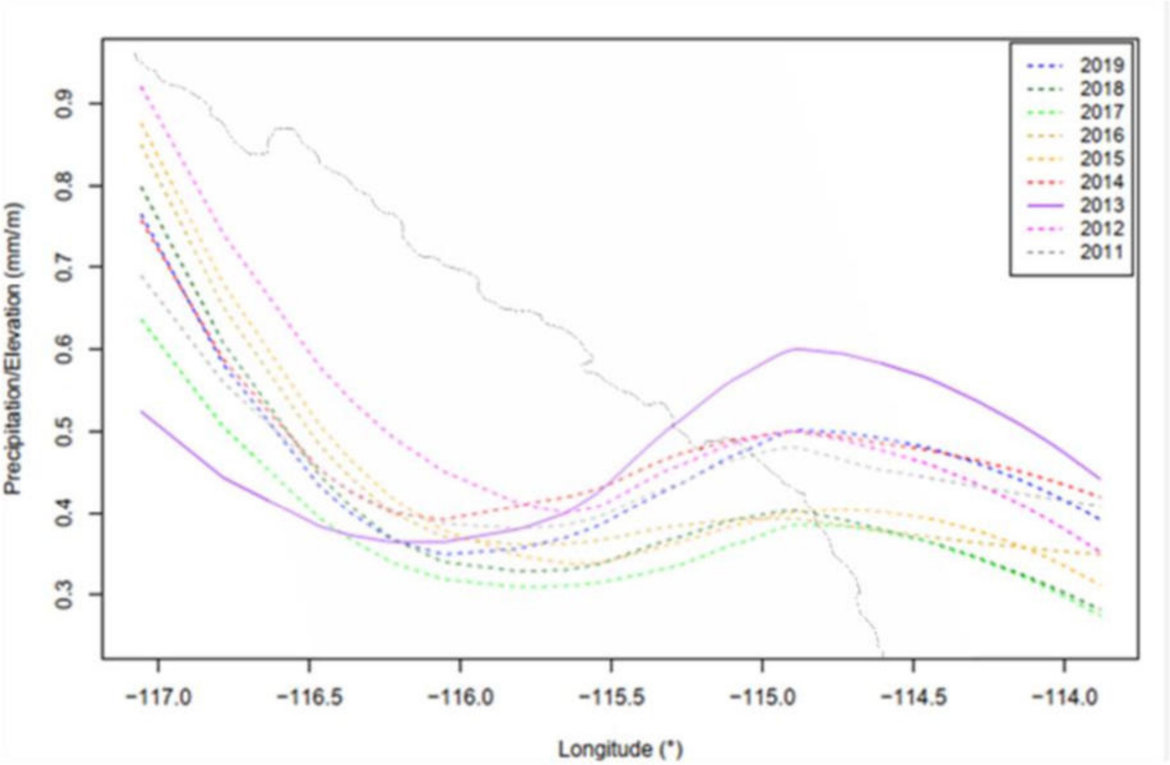

Figure E.4. LOESS regression curves of annual cumulative precipitation against longitude. Dotted lines represent years in which there was not a significant ($p < 0.05$) correlation between cumulative precipitation and longitude. Dots denote cumulative precipitation at stations. The grey line represents the location of the Continental Divide. The elevational profile differs from the previous longitudinal regression because there were fewer stations available for annual time periods between 2011-2019.

Appendix F

Cumulative Precipitation Plots and Intensity Plots for Precipitation During each Precipitation Event at SPADE Sites

Cumulative precipitation is plotted over time from Nipika, Fortress Mountain, and Fortress Junction, and Precipitation Gauge 1 (TBRG 1), Precipitation Gauge 2 (TBRG 2), and Precipitation Gauge 3 (TBRG 3) above wind vectors from Nipika (Figures F.1-13 (Left)). Cumulative precipitation is plotted per hour or per 15-minute period (the shorter increment of time available during a specific event) from Nipika, Fortress Mountain, and Fortress Junction above wind vectors from Nipika (Figures F.1-13 (Right)). Relative speed is related to wind vector magnitude. Horizontal arrow heads represent wind vectors of less than 0.5 $m \cdot s^{-1}$ (these values were eliminated from plots). Negative precipitation values at Nipika are likely due to wind induced gauge oscillations. The precipitation gauge transect was not operational during the first three events. Precipitation Gauge 3 was not operational during Event 13. For this analysis to include precipitation values from the precipitation gauge transect, the time-frame for Event 10 was adjusted to include a period of time 40 minutes before the start of the official SPADE Event and the time-frame for Event 11 was adjusted to include a period of time 50 minutes after the end of the official SPADE event.

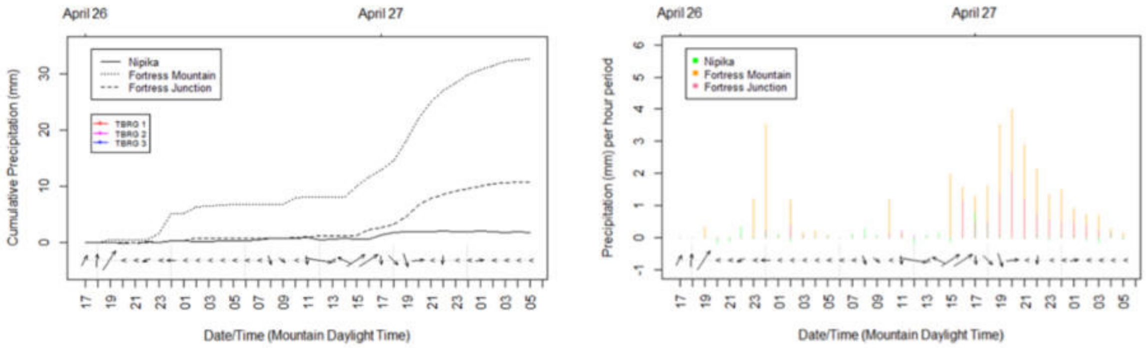

Figure F.1. SPADE Event 1 (16:50 MDT 26 April 2019 to 5:00 MDT 28 April 2019). This event was caused by an upper level trough and lasted for 35.8 hours. Water vapour flux was strongly upslope.

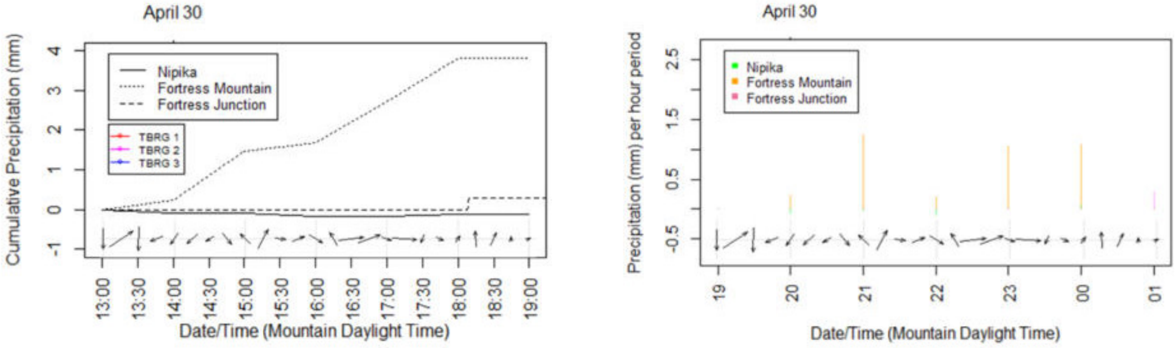

Figure F.2. SPADE Event 2 (13:30 UTC 30 April 2019 to 19:30 UTC 30 April 2019). This event was caused by an inverted near surface trough and lasted for six hours. Water vapour flux direction was parallel to the Canadian Rockies from the north.

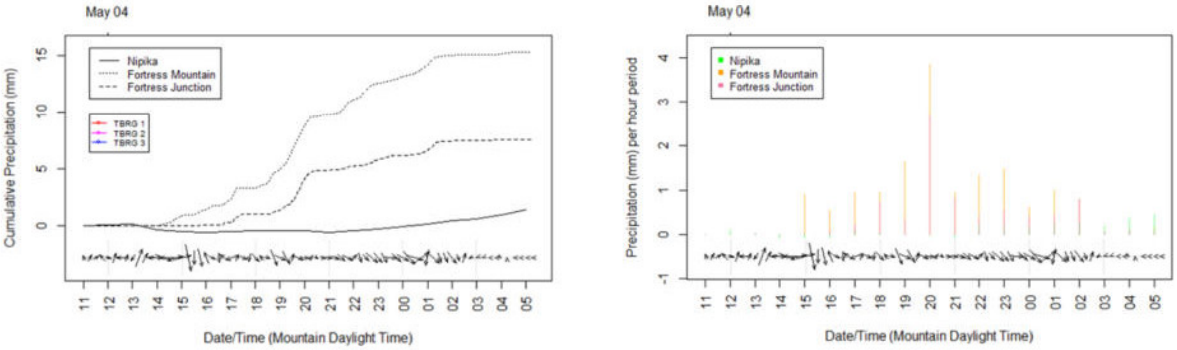

Figure F.3. SPADE Event 3 (11:00 MDT 4 May 2019 to 5:20 MDT 5 May 2019). This event was caused by an inverted near surface trough and lasted for 18.5 hours. Water vapour flux was from the northwest.

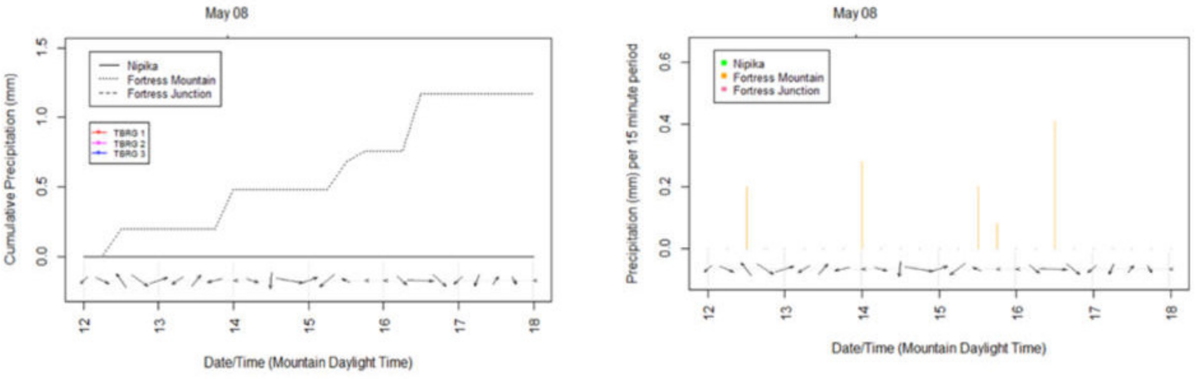

Figure F.4. SPADE Event 4 (12:00 MDT 8 May 2019 to 18:00 MDT 8 May 2019). This event was caused by an inverted near surface trough and lasted for 6 hours. Water vapour flux direction was parallel to the Canadian Rockies from the north.

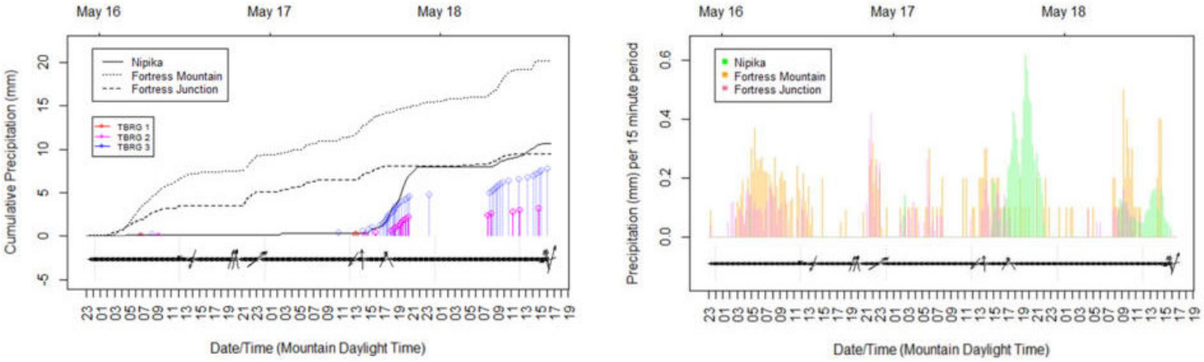

Figure F.5. SPADE Event 5 (23:00 MDT 15 May 2019 to 16:30 MDT 18 May 2019). This event was caused by an upper level ridge and lasted for 65.5 hours. Water vapour flux was from the south.

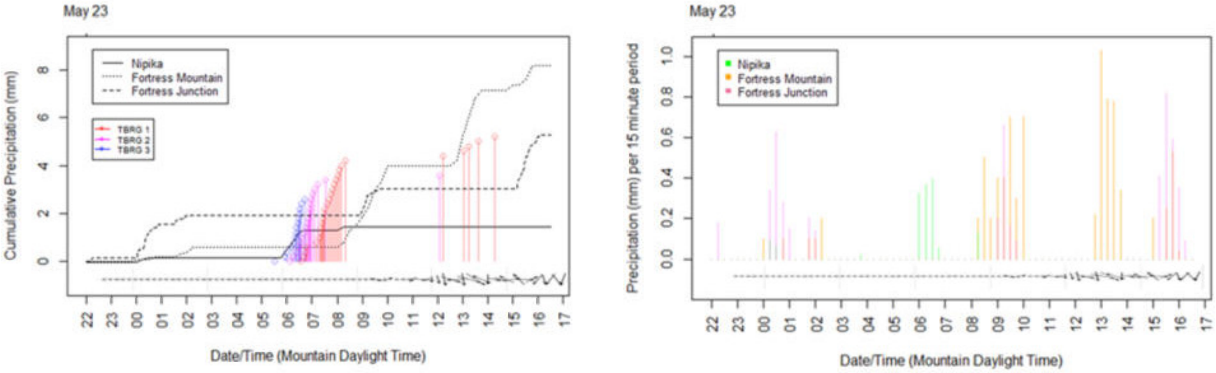

Figure F.6. SPADE Event 6 (22:45 MDT 23 May 2019 to 17:15 MDT 24 May 2019). This event was caused by local topography effects (there was little forcing by a synoptic scale system) and lasted for 18.5 hours. Water vapour flux was from the northeast.

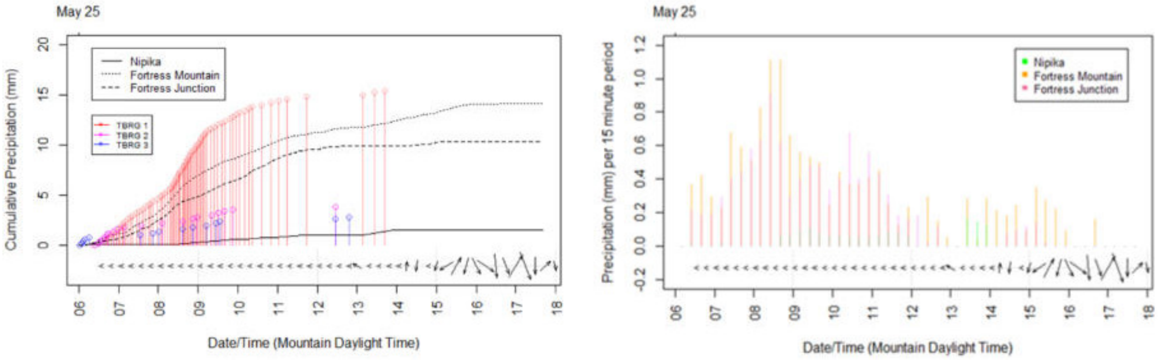

Figure F.7. SPADE Event 7 (6:20 MDT 25 May 2019 to 18:00 MDT 25 May 2019). This event was caused by local topography effects (there was little forcing by a synoptic scale system) and lasted for 11.5 hours. Water vapour flux was from the northeast.

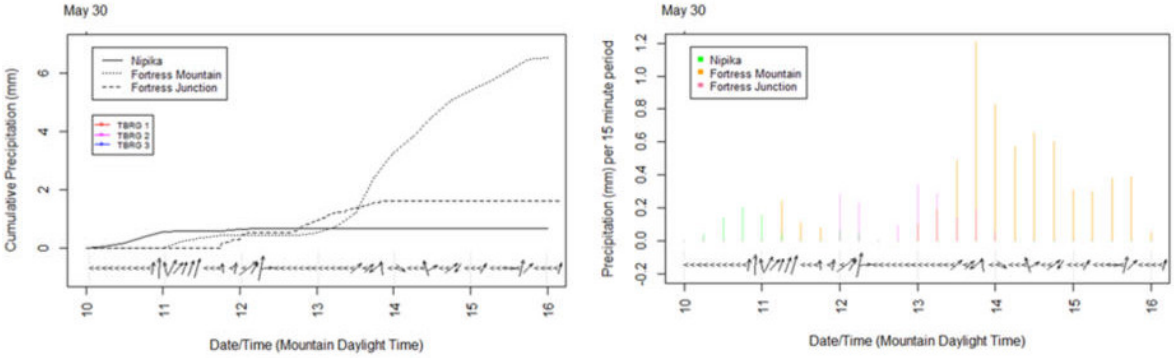

Figure F.8. SPADE Event 8 (10:00 MDT 30 May 2019 to 16:10 MDT 30 May 2019). This event was caused by an upper level trough and lasted for 6 hours. Water vapour flux was from the northwest.

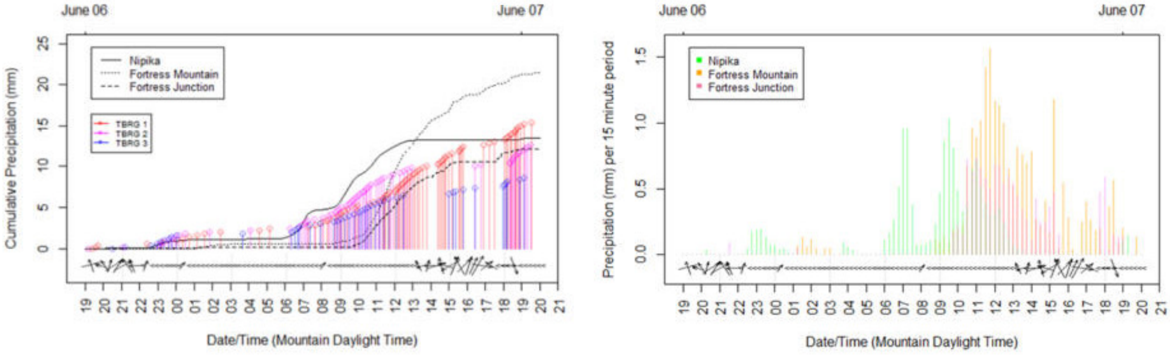

Figure F.9. SPADE Event 9 (19:00 MDT 6 June 2019 to 20:00 MDT 7 June 2019). This event was caused by an upper level trough and lasted for 25 hours. Water vapour flux was from the northwest.

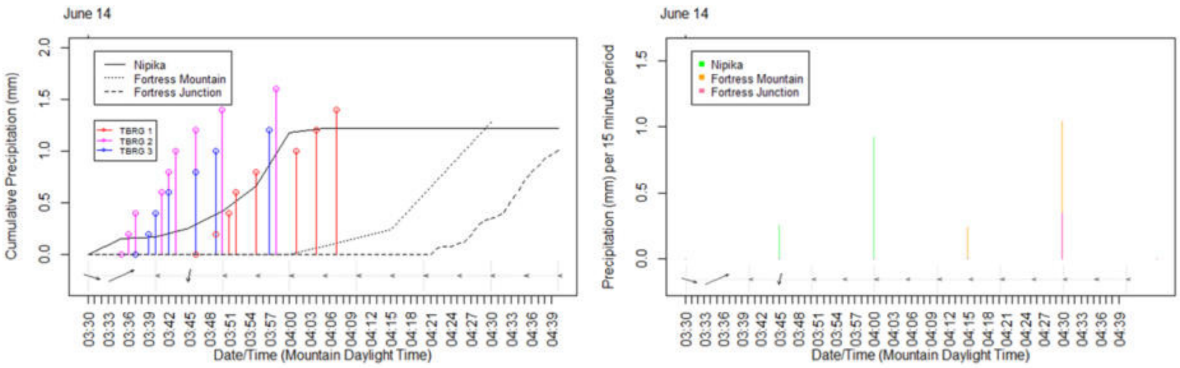

Figure F.10. SPADE Event 10 (4:10 MDT 14 June 2019 to 4:40 MDT 14 June 2019). This event was forced by mountain topography and lasted for 0.5 hours. My graphical analysis has been adjusted to include a period of time 40 minutes prior to the start of the official SPADE event. Water vapour flux was from the northwest.

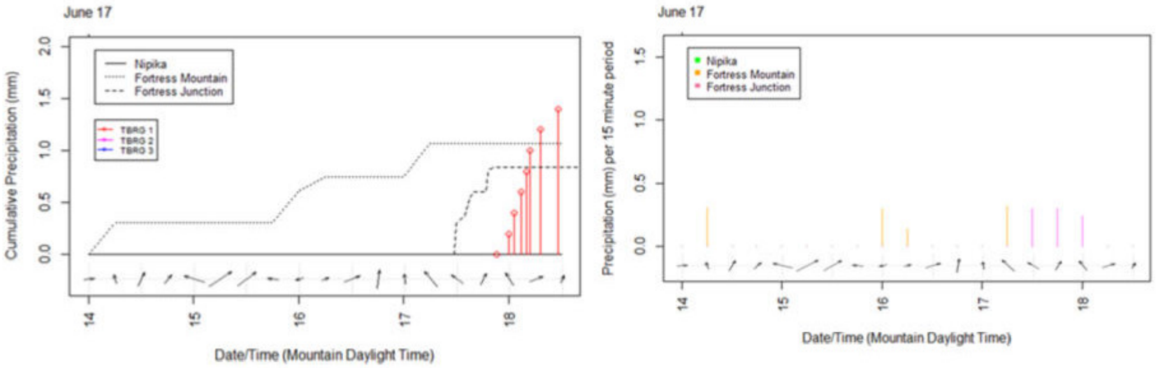

Figure F.11. SPADE Event 11 (14:00 MDT 17 June 2019 to 17:50 MDT 17 June 2019). This event was caused was forced by mountain topography and lasted for 3.5 hours. My graphical analysis has been adjusted to include a period of time 50 minutes after the end of the official SPADE event. Water vapour flux was from the west.

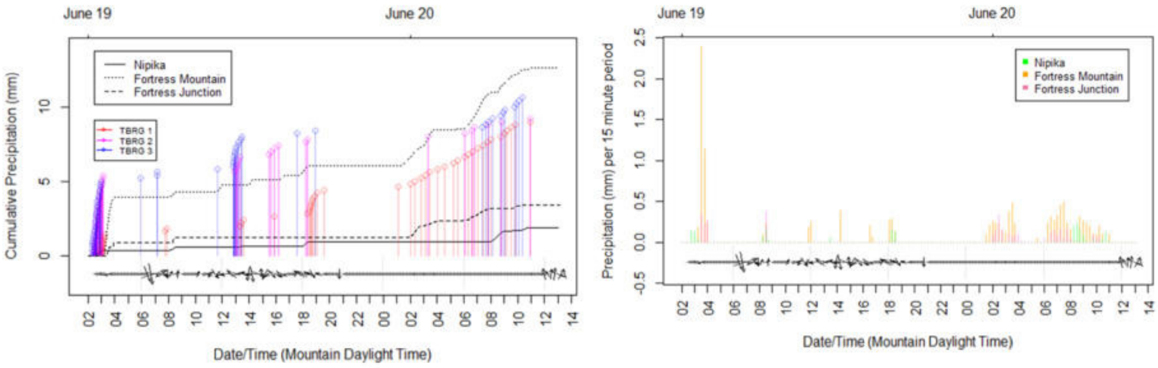

Figure F.12. SPADE Event 12 (2:30 MDT 19 June 2019 to 13:40 MDT 20 June 2019). This event was caused by an upper level trough and lasted for 35 hours. Water vapour flux was downslope of the Canadian Rockies, before becoming parallel, and then strongly upslope.

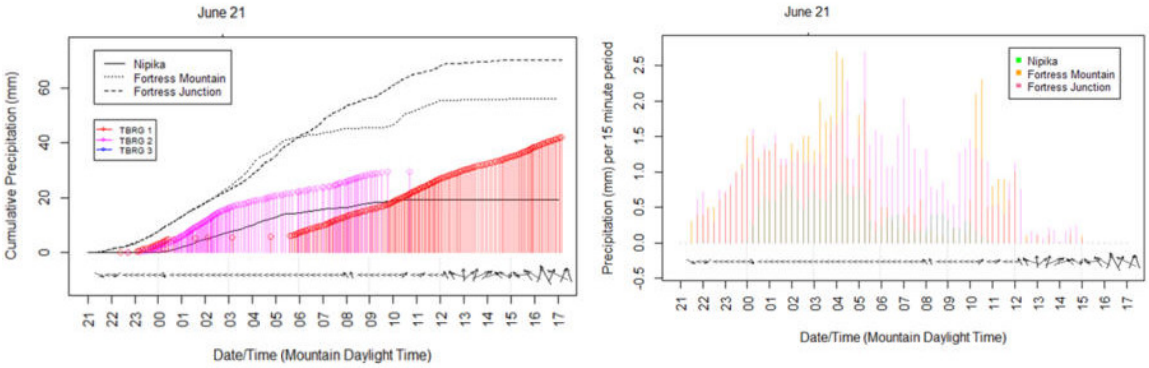

Figure F.13. SPADE Event 13 (21:30 MDT 20 June 2019 to 17:40 MDT 21 June 2019). This event was caused by an upper level trough and lasted for 20.25 hours. Water vapour flux was strongly upslope of the Canadian Rockies, but transitioned to a northerly direction towards the end of the event.

Appendix G

Precipitation roses for each SPADE event (Events 1 to 13) using wind data from Nipika

Precipitation roses have been replaced with wind roses during events in which there was no precipitation at Nipika. All wind vectors with less than 0.5 m·s^{-1} have been removed. Roses represent precipitation in millimetres.

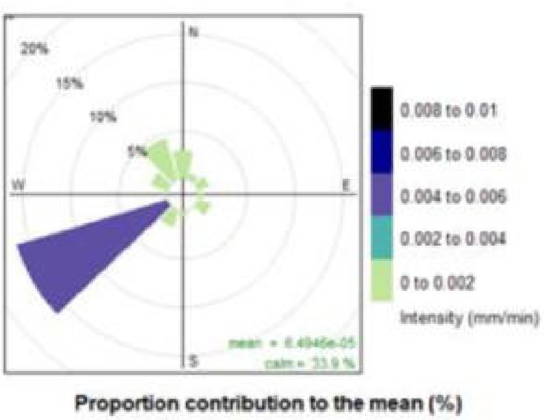

Figure G.1. SPADE Event 1 (16:50 MDT 26 April 2019 to 5:00 MDT 28 April 2019). This event was caused by an upper level trough and lasted for 35.8 hours.

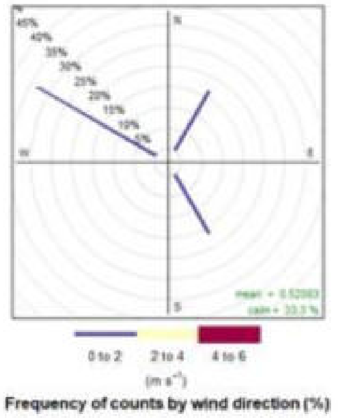

Figure G.2. SPADE Event 2 (13:30 UTC 30 April 2019 to 19:30 UTC 30 April 2019). This event was caused by an inverted near surface trough and lasted for six hours.

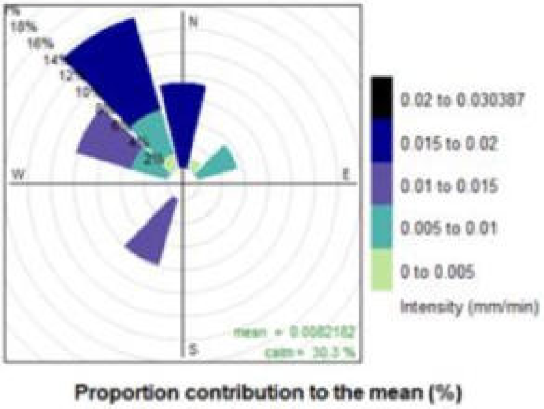

Figure G.3. SPADE Event 3 (11:00 MDT 4 May 2019 to 5:20 MDT 5 May 2019). This event was caused by an inverted near surface trough and lasted for 18.5 hours.

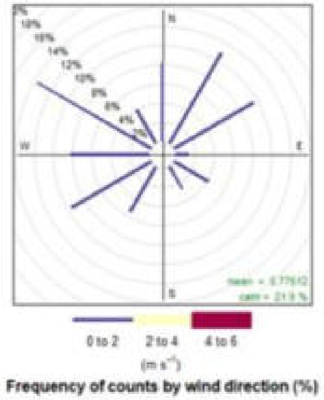

Figure G.4. SPADE Event 4 (12:00 MDT 8 May 2019 to 18:00 MDT 8 May 2019). This event was caused by an inverted near surface trough and lasted for 6 hours.

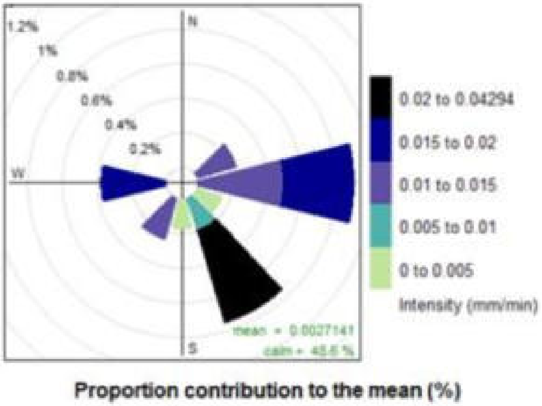

Figure G.5. SPADE Event 5 (23:00 MDT 15 May 2019 to 16:30 MDT 18 May 2019). This event was caused by an upper level ridge and lasted for 65.5 hours.

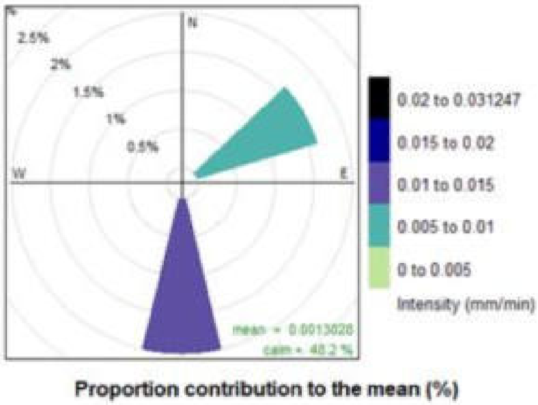

Figure G.6. SPADE Event 6 (22:45 MDT 23 May 2019 to 17:15 MDT 24 May 2019). This event was caused by local topography effects and lasted for 18.5 hours.

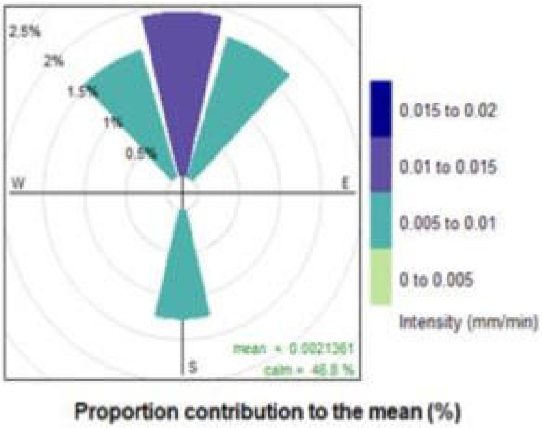

Figure G.7. SPADE Event 7 (6:20 MDT 25 May 2019 to 18:00 MDT 25 May 2019). This event was caused by local topography effects and lasted for 11.5 hours.

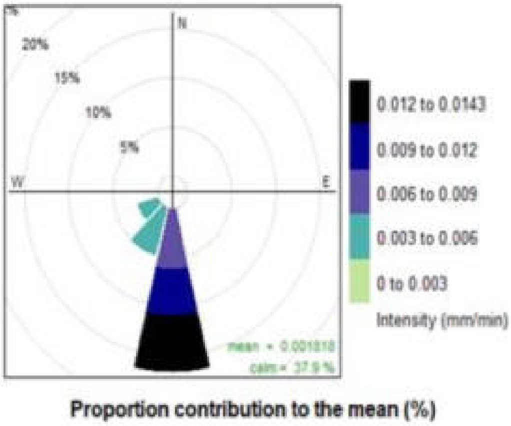

Figure G.8. SPADE Event 8 (10:00 MDT 30 May 2019 to 16:10 MDT 30 May 2019). This event was caused by an upper level trough and lasted for 6 hours.

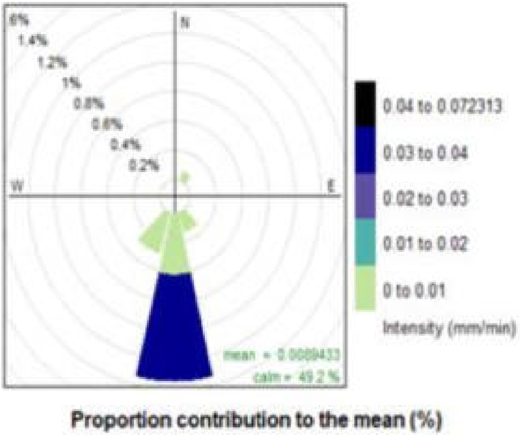

Figure G.9. SPADE Event 9 (19:00 MDT 6 June 2019 to 20:00 MDT 7 June 2019). This event was caused by an upper level trough and lasted for 25 hours.

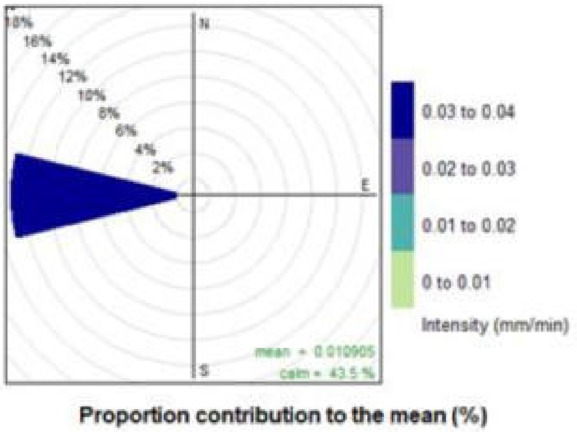

Figure G.10. SPADE Event 10 (4:10 MDT 14 June 2019 to 4:40 MDT 14 June 2019). This event was caused by topography and lasted for 0.5 hours. My analysis includes 40 minutes prior to the start of the SPADE event.

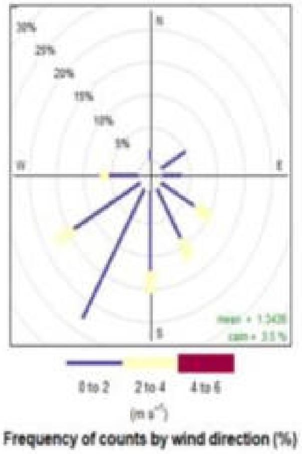

Figure G.11. SPADE Event 11 (14:00 MDT 17 June 2019 to 17:50 MDT 17 June 2019). This event was caused by topography and lasted for 3.5 hours. My graphical analysis has been adjusted to include a period of time 50 minutes after the end of the SPADE event.

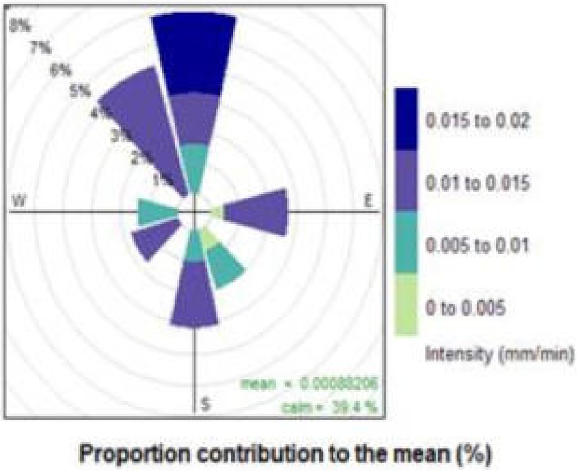

Figure G.12. SPADE Event 12 (2:30 MDT 19 June 2019 to 13:40 MDT 20 June 2019). This event was caused by an upper level trough and lasted for 35 hours.

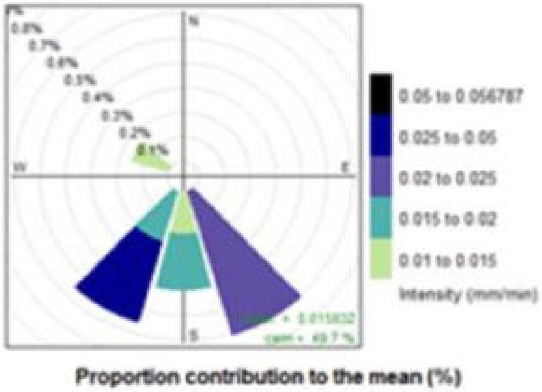

Figure G.13. SPADE Event 13 (21:30 MDT 20 June 2019 to 17:40 MDT 21 June 2019). This event was caused by an upper level trough and lasted for 20.3 hours.